ELECTRONIC PROPERTIES OF CARBON NANOTUBES: COMBINED EFFECT OF GEOMETRY AND CORRELATIONS

THÈSE N^O 3328 (2005)

PRÉSENTÉE À LA FACULTÉ SCIENCES DE BASE

Institut de théorie des phénomènes physiques

SECTION DE PHYSIQUE

ÉCOLE POLYTECHNIQUE FÉDÉRALE DE LAUSANNE

POUR L'OBTENTION DU GRADE DE DOCTEUR ÈS SCIENCES

PAR

Thomas GLOOR

ingénieur physicien diplômé EPF
et de nationalité liechtensteinoise

acceptée sur proposition du jury:

Prof. F. Mila, directeur de thèse
Prof. L. Forro, rapporteur
Prof. T. Martin, rapporteur
Dr K. Penc, rapporteur

Lausanne, EPFL
2005

Abstract

In this thesis we study the interplay between electronic correlations and geometry in single–walled carbon nanotubes by microscopic model calculations. Electronic correlations are expected to be strong because of the low dimensionality of carbon nanotubes. Moreover the possibility of existing in different chiralities make them an ideal model system to investigate this interplay.

After reviewing the band theory we discuss the magnitude and the scaling of the single particle charge gap when electronic correlations are included. This is done within a Hartree–Fock mean field calculation and with the help of a renormalization group argument. We predict that there is a correlation induced charge gap of several meV. This result is especially important for carbon nanotubes of armchair chirality where the band gap is always zero. We also observe that this correlation gap is tunable with uniaxial strain.

In another chapter we study the electronic properties when a magnetic field parallel to the tube axis is applied. The persistent currents show a strong dependence on chirality. When we look at the diffusive limit by adding disorder (impurities) we can exhibit the Altshuler–Aronov–Spivak effect.

The last two chapters are concerned with the question of superconductivity in carbon nanotubes. We calculate the spingap in the Heisenberg model for the smallest tubes by an exact quantum Monte Carlo method. We relate these results to the RVB theory of superconductivity (mean–field and variational Monte Carlo) which describes the system upon hole doping. We obtain chirality dependent RVB superconducting order parameters. Compared to the two dimensional limit we observe that superconductivity is enhanced and antiferromagnetism is reduced.

Wherever possible we try to put our results into relation with experimental findings.

Version abrégée

Nous avons étudié l'effet combiné des corrélations électroniques et de la géométrie dans les nanotubes de carbone monoparois en utilisant des modèles microscopiques. Du fait de la basse dimensionalité des nanotubes de carbone, on s'attend à ce que les corrélations électroniques soient fortes. De plus comme ils peuvent exister dans des chiralités différentes, ils forment un cadre idéal pour cette étude.

Après une présentation de la théorie des bandes nous discutons la valeur du gap de charge et son comportement en fonction du diamètre, en incluant les corrélations électroniques par un calcul de type Hartree–Fock et un argument du groupe de renormalisation. Nous obtenons un gap de charge, induit par les corrélations, de l'ordre du meV. Ce résultat est spécialement important pour les tubes de chiralité "armchair" où la théorie des bandes prédit toujours un comportement métallique. Nous observons aussi que ce gap de corrélation est ajustable en appliquant une tension axiale.

Dans un autre chapitre, nous étudions les propriétés électroniques des tubes dans un champ magnétique longitudinal. Les courants permanents montrent une dépendance importante en fonction de la chiralité. En ajoutant du désordre (impuretés), nous considérons aussi la limite diffusive où l'effet Altshuler–Aronov–Spivak est observé.

Les deux derniers chapitres sont consacrés à la question de la supraconductivité dans les nanotubes de carbone. Nous déterminons le gap de spin dans le modèle de Heisenberg pour les tubes de plus petit diamètre, par une méthode de Monte Carlo quantique exacte. Nous mettons en relation ces résultats avec la théorie RVB de la supraconductivité (champ moyen et Monte Carlo variationnel) qui décrit le système dopé. Les paramètres d'ordre de la supraconductivité RVB dépendent de la chiralité. En comparaison avec la limite 2D, nous observons que près du demi–remplissage, la supraconductivité est renforcée et l'antiferromagnetisme est réduit.

Nous avons essayé de mettre systématiquement nos résultats en relation avec les expériences.

Acknowledgments

The biggest thank goes to Frédéric Mila who gave me the opportunity to engage a doctoral thesis in his group. During these four years he was continuous source of ideas, particularly he was the point of origin for all chapters presented in this thesis. Besides him I had also the chance to collaborate with the following distinguished physicists:

Chapter 4: This was a collaboration with Didier Poilblanc during his stay in Lausanne in the summer of 2002. Everything I know about persistent currents and charge stiffness I learned from him.

Chapter 5: Andreas Läuchli showed me the way through the ALPS library and QMC simulations. Further I thank him for his continuous interest in my work, for the many clever remarks and suggestions, and also for showing me all those computer tricks.

Chapter 6: When I was doing the RVB mean field theory I could profit from the experience of Brijesh Kumar. Thanks to Brijesh for answering so many annoying questions. The credits for the variational MC simulations go entirely to Cédric Weber. Some time ago these simulations were started together by debugging our VMC codes. I stopped my VMC experience after the Gutzwiller projection of the Fermi sea, whereas Cédric went the way up to true mastery. It was an honor for me to be on his list of projects, thank you Cédric.

I hope that now the reader will understand better what I mean by "we" which I used throughout the whole thesis.

In addition I would like to thank the following people for innumerous discussions, valuable help and excellent company: Japhet Bagilishya, Jean–Sébastien Caux, David Eichenberger, Maged Elhajal (special thanks to Maged for reading and commenting on the manuscript), Jean–Baptiste Fouet, Marco Grioni, Valeri Kotov, Susanne Mölbert, Shin Myahara, Arnaud Ralko, Ewald Roessl, François Vernay.

I thank Yvonne, Georg and Martin for their friendship and for sharing my highs and lows during this thesis.

I am especially grateful to my parents for their love and their support.

Contents

Chapter 1

Introduction

Carbon nanotubes (CNT) are large cylindrical molecules which consist of carbon atoms only.[1] Their structure is similar to graphite as each atom is covalently bound to three nearest neighbours to form a honeycomb lattice. Whereas in graphite two dimensional layers are stacked, CNT are rolled up to sheets forming a cylinder usually closed by spherical cups. One distinguishes two types of CNT: The single–walled CNT (SWCNT) are made out of a single cylinder. In contrast multiwalled CNT consist of several concentrically arranged tubes.

The discovery of CNT goes back to 1991 [4], Iijima observed multiwalled CNT, when he analyzed carbon soot from an arc discharge by transmission electron microscopy. In the arc–discharge method a large voltage is applied between two electrodes of pure graphite until there is discharge through strong currents in an inert gas between them. The temperatures involved are high (3000-4000 K) and are close to the melting temperature of graphite. Multiwalled CNT can then be found in the soot that is produced on the negative electrode. SWCNT could be produced two years later [5,6]. There it was shown that the arc discharge method could also be used to produce SWCNT but a catalyst, *e.g.* cobalt, had to be added at the anode.

There are two other methods for CNT production, the laser ablation technique and the chemical vapor deposition (*cf e.g.* [2]). The latter is believed to be very promising because controlled CNT growth on surfaces is possible and the process can also be scaled up. In the chemical vapor deposition acetylene gas is led into a heated reactor which contains a transition metal catalyst. The CNT are produced in high yields upon cooling to room temperature.

The typical tube diameters are a few nanometers for SWCNT and multiwalled CNT have diameters up to 50 nm. The length is usually of several hundreds of nm but can be as large as a few micrometers. However length and diameter are

---

[1]Several textbooks about CNT were published: The book by Saito *et al.* [1] focuses on the the tight binding description, the book edited by Dresselhaus *et al.* [2] gives a summary of the state of knowledge at the beginning of 2001. A more recent monograph by Reich *et al.* [3] concentrates on luminescence and Raman scattering.

not the only parameter to characterize a perfect CNT. It was noticed right away by Iijima [4] that there are CNT with different chiralities, *i.e.* there is an angle degree of freedom how a single graphite sheet can be rolled up into a cylinder.

In this thesis we will nearly exclusively be concerned with electronic properties of SWCNT. We will see that in a simple one–electron picture SWCNT are either metallic or semiconducting depending on chirality. Both types of SWCNT are actually observed. The semiconducting SWCNT behave typically as a p–type field–effect transistor at room temperature [7] whereas metallic CNT show only very little gate dependence [8]. Scanning tunneling microscopy measurements showed also metallic or semiconducting density of states [9, 10]. At millikelvin temperatures SWCNT can behave as true quantum wires where electrons conduct coherently over long distances through well separated channels [11]. In tunneling experiments of SWCNT ropes, a power law behaviour in the density of states is observed and therefore it was suggested that SWCNT would show Luttinger liquid physics [12]. In 2001, it was achieved for the first time to attach very low– ohmic contacts to SWCNT [13,14]. As a result, interference patterns of electrons reflected at the contacts could be observed [13]. In the last few years there has been growing evidence that besides proximity induced superconductivity, also true intrinsic superconductivity could exist in ropes of SWCNT [15]. The critical temperature is sample dependent and varies from 120 to 550 mK.

After the early CNT history told by Ebbesen [16], the same year but still be- fore the discovery of CNT, a group of theorists asked the question "Are fullerene tubules metallic?". Apparently their paper was judged too speculative for publi- cation, and could only be published after the discovery of CNT [17]. Since then a huge number of theoretical investigations appeared. Most of them can be crudely separated into two groups. The first group consists of papers which try to explain the properties of CNT with the help of band structure calculations (*ab initio*, tight binding, *etc.*) where the typical energy scale is the eV. These calculations neglect electron–electron interactions which are however strong in reduced dimensions. On the other hand the second group tries to give a field theoretical description for physical processes at the meV scale. In this continuous description the effect of band structure is only taken into account by linearized bands around the two Fermi points and one obtains a purely one–dimensional description where the electrons have forgotten that they live on a two–dimensional surface. But it has the advantage that many analytic methods from one–dimensional physics become available which allow to treat electron–electron interaction.

Of course, the ultimate goal of a complete theory of CNT would be the unifi- cation of the two approaches, *i.e.* to treat the true NT topology and interactions on the same footing. But needless to say that this is far beyond what can be done by present methods, so the reader of this thesis has to be content with much more modest goals. They are outlined in the next paragraph.

Goal of the thesis

The goal of this thesis is to explain a certain number of electronic properties of carbon nanotubes. Most notably we are interested in effects where electron–electron interaction plays an important role, this is where band theory alone is insufficient to explain the observed phenomena. Our working method consists of analyzing microscopic models analytically or numerically, always with the goal to gain a better understanding of experimental findings, or to make some new predictions which can be tested experimentally.

The following questions have been addressed:

- Can we clarify the value and scaling of the single particle charge gap. Or in other words, can clean SWCNT be metallic ? (chapter 3)

- How does uniaxial strain change the electronic properties of CNT ? (section 3.8)

- What effect has an applied longitudinal magnetic field on the properties of CNT ? In particular, can we explain the oscillations (fast and slow) in the resistivity versus applied magnetic flux measurements ? (chapter 4)

- How does the spin gap depend on chirality ? (chapter 5)

- What can we say about superconductivity in CNT ? And more generally, what phases can appear when we dope CNT ? (chapter 6)

Chapter 2

Tight binding band structure of SWCNT

2.1 Summary

The determination of the band structure of SWCNT is an important starting point of all subsequent theoretical studies in this work. The simplest way to get an idea of the band structure of SWCNT is to use the tight–binding energy band due to the graphene p_z orbitals, determined originally by Wallace in 1947 [18], and then to impose the appropriate periodic boundary condition which reflects the cylindrical shape of the CNT. This calculation was done first in the references [19, 20] and helped to find a suitable classification scheme for CNT, using the chiral vector $\mathbf{C_h}$. This chapter is mainly based on the book by Brandt *et al.* on graphite [21] and the book by Dresselhaus *et al.* on CNT [2]. Below we derive the tight–binding band structure of SWCNT and we discuss its validity reviewing the results obtained by *ab initio* calculations.

2.2 Graphene

The neutral carbon atom contains six electrons in a $1s^2 2s^2 2p^2$ configuration. The ground state of a free carbon atom is ^3P, i.e. with total spin $S = 1$ and total orbital angular momentum $L = 1$. The variety of carbon materials, ranging from 0 to 3 dimensional structures (cf table 2.1), is due to the special character of the bonds between carbon atoms. The energy difference between the ground state and the first excited state of the free carbon atom $(1s^2 2s 2p^3 /^5 S)$ is about 4 eV which is small compared to the interatomic binding energy of about 7.4 eV [21]. This fact makes it very often energetically favorable to excite a $2s$ electron into the p shell to form bondings with other carbon atoms. Now the four electrons can mix with each other to enhance the binding energy with other carbon atoms. This mixing is called hybridization, more precisely, the mixing of one $2s$ electron

dimension	0 d	1 d	2 d	3 d
isomer	C_{60} fullerene	nanotube	graphite	diamond amorphous
hybridization	sp^2	sp^2	sp^2	sp^3
density g/cm^3	1.72	1.2–2.0	2.26	3.515 2–3
bond length Å	1.40 $(C = C)$ 1.46 $(C - C)$	1.44 $(C = C)$	1.42 $(C = C)$	1.54 $(C - C)$
electronic properties	semiconductor $E_g = 1.9$ eV	metal or semiconductor	semimetal	insulating $E_g = 5.47$ eV

Table 2.1: Some carbon isomers (This table was taken from reference [1])

with n $2p$ electrons is called sp^n hybridization.

We call graphene a single layer of graphite. It forms a two dimensional hexagonal structure, called honeycomb lattice (cf figure 2.1). In this lattice the carbon atoms form three equivalent bonds. One $2s$ electron and two $2p$ electrons form σ–bonds through sp^2 hybridization. The σ–bonds are coplanar and make angles of 120° between them. The spatial electronic density of the fourth valence $2p$ electron is orthogonal to the plane of σ–bonds. These $2p$ electrons of neighboring atoms overlap to form π–bonds. In this model each carbon atom is bounded to three other carbon atoms by one π–bond and three σ–bonds. The resulting honeycomb lattice with its unit cell and its reciprocal lattice with the first Brioullin zone is shown in figure 2.1.

We determine the band structure in the tight–binding calculation. We content ourselves with the calculation of the π–bands since they are responsible for most of the electronic properties of graphene. The σ–bands are completely filled and do not mix with the π–bands due to symmetry. In a tight–binding calculation the π–bands are formed from orbitals with p_z character. Each lattice site in the honeycomb lattice has three nearest–neighbours. For graphene one expects that all nearest–neighbour hopping matrix elements are the same for all these three bonds. However for later convenience we chose different hopping integrals $t_\perp$, $t_{1\parallel}$ and $t_{2\parallel}$ for each nearest–neighbour bond.[1] Thus the auxiliary equation for the graphene tight–binding energy bands ϵ_{2d} is:

$$\begin{vmatrix} -\epsilon_{2d} & t_\perp + t_{1\parallel}e^{i\mathbf{k}\cdot\mathbf{a_1}} + t_{2\parallel}e^{i\mathbf{k}\cdot\mathbf{a_2}} \\ t_\perp + t_{1\parallel}e^{-i\mathbf{k}\cdot\mathbf{a_1}} + t_{2\parallel}e^{-i\mathbf{k}\cdot\mathbf{a_2}} & -\epsilon_{2d} \end{vmatrix} = 0 \qquad (2.1)$$

---

[1]In the language of Slater and Koster the t's are nothing else than the $V_{pp\pi}$ interatomic matrix elements (cf p. 481 of reference [22]).
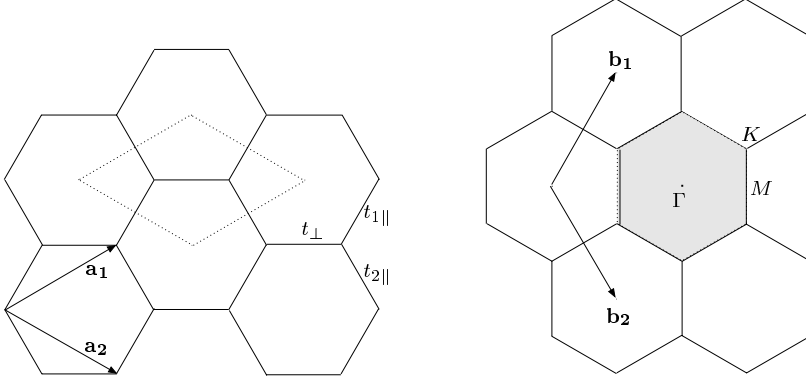
Figure 2.1: The figure on the left hand side shows the two-dimensional honeycomb lattice. Its unit cell contains two carbon atoms and has the shape of a rhombus. The basis vectors are chosen to be $\mathbf{a_1} = a/2\,(\sqrt{3}, 1)$ and $\mathbf{a_2} = a/2\,(\sqrt{3}, -1)$ where $a = 2.46$, the lattice constant of graphene. This distance is slightly modified for CNT where $a = 2.49$. $t_\perp$, $t_{1\parallel}$ and $t_{2\parallel}$ are the hopping integrals corresponding to different hopping directions. On the right hand side the reciprocal lattice is shown. The shaded region corresponds to the first Brioullin zone and Γ, K and M indicate the high symmetry points. The reciprocal basis vector are $\mathbf{b_1} = 2\pi/a\,(1/\sqrt{3}, 1)$ and $\mathbf{b_2} = 2\pi/a\,(1/\sqrt{3}, -1)$.

Setting $\mathbf{k} = \alpha_1/2\pi\,\mathbf{b_1} + \alpha_2/2\pi\,\mathbf{b_2}$ we get for the energy dispersion of graphene

$$
\begin{aligned}
\epsilon_{2d}(\alpha_1, \alpha_2) &= \pm\left| t_\perp + t_{1\parallel}e^{i\alpha_1} + t_{2\parallel}e^{i\alpha_2} \right| \\
&= \pm\left(t_\perp^2 + t_{1\parallel}^2 + t_{2\parallel}^2 + 2t_\perp t_{1\parallel}\cos\alpha_1 + 2t_\perp t_{2\parallel}\cos\alpha_2 \right.\\
&\quad \left. + 2t_{1\parallel}t_{2\parallel}\cos(\alpha_1 - \alpha_2) \right)^{1/2} .
\end{aligned}
\tag{2.2}
$$

We finish this section by giving an idea of the band structure of graphene using the dispersion relation (2.2). In figure 2.2 we plotted the bands along the high symmetry lines (*cf* figure 2.1). We note that close to half–filling only the states near the K points are forming the Fermi surface. But at this electron fillings the density of states is very low, and even vanishing exactly as $\epsilon \to 0$. This explains the semimetallic behaviour of graphite. We also observe van Hove singularites in the density of states at energies $\pm\,1t$ which correspond to fillings of $^3/_8$ and $^5/_8$ respectively.

2.3   Classification of Carbon Nanotubes

We are going to think about SWCNT as a rectangular graphene layer rolled up into a cylinder. In a first approximation we do not consider differences in the hopping integrals due to bending, i.e. $t \equiv t_\perp = t_{1\parallel} = t_{2\parallel}$. Thus forming a SWCNT consists just in imposing the appropriate periodic boundary conditions on the graphene layer. A classification of all SWCNT can be given with the help
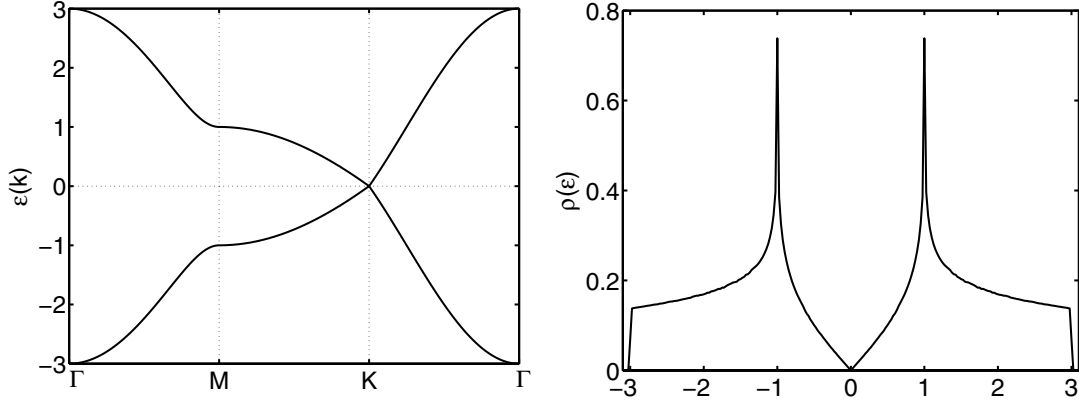
Figure 2.2: At the left hand side we show the tight binding bandstructure of a single graphene layer along the lines of high symmetry. At the right hand side the corresponding single particle density of states $\rho(\epsilon) = -\frac{1}{\pi L}\mathrm{Im}\sum_{\mathbf{k},p} G_p(\mathbf{k}, \epsilon + i\delta)$ is plotted (p is the band index and L is the total number of sites). We recall that $G_p(\mathbf{k}, i\omega)$ is the single particle Green's function which is for non–interacting systems given by $G_p(\mathbf{k}, i\omega) = \frac{1}{i\omega - \epsilon_{\mathbf{k}}^{(p)}}$. The van Hove singularities are found at energies $\pm\, t$ which correspond to fillings of $3/8$ and $5/8$ respectively.

of the so called chirality vector $\mathbf{C_h}$. As it is done in figure 2.3 we can choose two sites $\mathbf{s_1}$ and $\mathbf{s_2}$ on the honeycomb lattice to define the chirality vector

$$\mathbf{C_h} = \mathbf{s_2} - \mathbf{s_1} = n\mathbf{a_1} + m\mathbf{a_2}. \tag{2.3}$$

Then the lattice is cut along $\mathbf{C_h}$ and lines perpendicular to it passing through $\mathbf{s_1}$ and $\mathbf{s_2}$ respectively. Folding up the resulting rectangle gives the nanotube, more precisely a SWCNT of type (n, m). For symmetry reasons it is exhaustive to consider only tubes with $n \geq m$. Up to the length, the chirality vector classifies completely all the carbon nanotubes. The angle θ between $\mathbf{C_h}$ and $\mathbf{a_1}$ is called chiral angle (cf figure 2.3) and it is given by $\tan\theta = \sqrt{3}m/(2n + m)$. There are two limiting cases which are of particular interest:

1. The $(n, 0)$ "zig-zag" CNT with a chiral angle of $0°$.

2. The (n, n) "armchair" CNT with a chiral angle of $30°$.

We will apply periodic boundary conditions not only along $\mathbf{C_h}$ but also along the CNT. Thus the length of a tube is not arbitrary. The CNT must be a multiple of the one dimensional unit cell. The one dimensional unit cell is defined by $\mathbf{C_h}$ and a vector $\mathbf{T}$ perpendicular to $\mathbf{C_h}$. The vector $\mathbf{T}$ has to be able to join two equivalent sites of the honeycomb lattice, thus its lentgth is defined by the first occurrence of an equivalent site in this direction (*cf* figure 2.3). It is easy to see that $\mathbf{T}$ is given by

$$\mathbf{T} = t_1\mathbf{a_1} + t_2\mathbf{a_2} \quad \text{with} \tag{2.4}$$
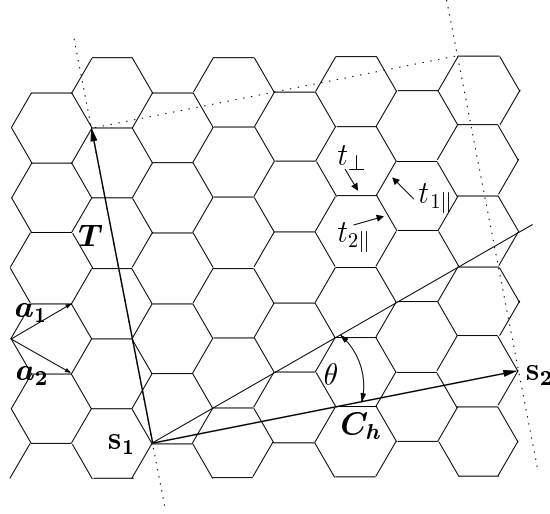
Figure 2.3: We show how we can contruct SWCNT from the honeycomb lattice of graphite and we classify them with the help of the chirality vector $\mathbf{C_h}$. The tube axis is along $\mathbf{T}$. The rectangle defined by $\mathbf{C_h}$ and $\mathbf{T}$ defines the one-dimensional unit cell. The tube constructed in the figure corresponds to $\mathbf{C_h} = 4\,\mathbf{a_1} + 2\,\mathbf{a_2} = (4, 2)$.

$$t_1 = \frac{2m + n}{d_R} \quad \text{and} \quad t_2 = -\frac{2n + m}{d_R} \tag{2.5}$$

where d_R is the greatest common divisor of $2m + n$ and $2n + m$. We define the length of a CNT by an integer N in units of $\|\mathbf{T}\|$. Usually all the quantities are calculated in the limit of a very long tube, i.e. N is large. In this case they should not depend on the particular boundary conditions chosen along the tube.

2.4 Band Structure

In this section we determine the tight binding band structure of CNT. We start from the band structure of graphene which is given by the dispersion relation (2.2) and the two–dimensional first Brioullin zone (*cf* figure 2.1). We have seen in the previous section that we can obtain the CNT structure from graphene by imposing periodic boundary conditions:

$$N\mathbf{T} \cdot \mathbf{k} = 2\pi q \quad q \in \mathbb{N} \tag{2.6}$$
$$\mathbf{C_h} \cdot \mathbf{k} = 2\pi p \quad p \in \mathbb{N} \tag{2.7}$$

As we are working with a very long tube, there is a quasi–continous set of wavevectors, indexed by q, which are inequivalent. Thus these two conditions select N_{1D} lines in the two–dimensional first Brillouin zone of graphene. The number N_{1D} is given by the number of hexagons in the one–dimensional unit cell defined by
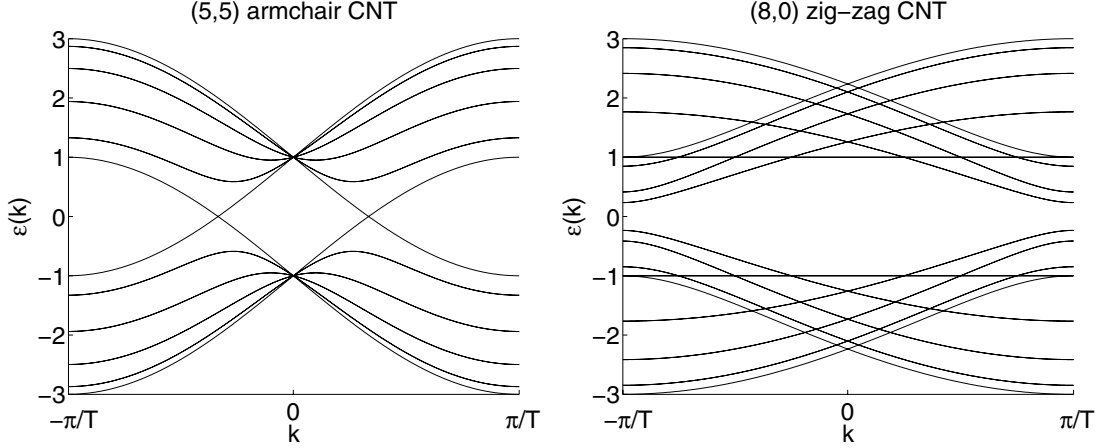
Figure 2.4: The tight–binding energy bands for a metallic $(5,5)$ armchair CNT and a semiconducting $(8,0)$ zig–zag CNT are plotted. The energies are given in units of the hopping amplitude t_0.

$\mathbf{C_h}$ and $\mathbf{T}$ which is

$$N_{1D} = \frac{2\left(n^2 + m^2 + mn\right)}{d_R}. \tag{2.8}$$

This discrete set of lines which defines the first Brioullin zone for CNT can be parametrized by two integers, say p and q:

$$\mathbf{k} = 1/N_{1D}\left[\left(-p\,t_2 + \frac{q}{N}m\right)\mathbf{b_1} + \left(p\,t_1 - \frac{q}{N}n\right)\mathbf{b_2}\right] \tag{2.9}$$

$$p = 0,\dots,N_{1D}-1 \qquad q = 0,\dots,N-1 \tag{2.10}$$

In figure 2.4 we show two examples of CNT band structures where we have put $t_\perp = t_{1\|} = t_{2\|}$. This approximation means that for instance we neglect the effect of curvature on the hopping integrals. Within this approximation all CNT which have a chirality such that $n - m$ is a multiple of 3 are metalic. Still within the same approximations, the band gap of semiconducting CNT is proportional to the inverse of its diameter d_t

$$E_g = \frac{2t_0 a}{\sqrt{3}d_t} \quad \text{where} \quad d_t = \frac{a}{\pi}\sqrt{n^2 + m^2 + nm}. \tag{2.11}$$

Thus typically, semiconducting CNT have an energy gap of order 0.5 eV. This behaviour has been tested in experiments [9,10] where the tube diameter and the energy gap were extracted from scanning tunneling microscopy data. This data could be fitted to equation (2.11) with reasonable values of $t_0 = 2.5$–2.7 eV.[2] A

---

[2]Essentially the same values are inferred from Raman scattering experiments (see reference [23] and references therein). *Ab initio* calculations can also give an estimate for t_0 and they confirm the results mentioned before $t_0 = 2.4$–2.6 eV depending on chirality [23] and $t_0 = 2.5$ eV [17].

typical bandstructure of metallic armchair CNT is shown at the left hand side of figure 2.4. For clean CNT the Fermi level is at zero energy as we have a bipartite lattice and one π electron per carbon atom (half–filling). At zero energy we have two band crossings and the band dispersion is nearly linear. If one expands the dispersion around $\mathbf{k}_F = {}^1\!/_3 \, (\mathbf{b_1} - \mathbf{b_2})$ which are the K points in the first Brillouin zone, one obtains

$$\epsilon_{2d}(\boldsymbol{k_F} + \boldsymbol{q}) = \frac{a}{2}\sqrt{3}t_0 \, ||\boldsymbol{q}||. \tag{2.12}$$

From this equation one can compute the density of states per carbon atom for armchair CNT around the Fermi energy [24]

$$\rho(\epsilon) = \frac{2\sqrt{3}}{\pi^2}\frac{1}{t_0}\frac{a}{d_t} \tag{2.13}$$

which differs from the same quantity calculated for graphene

$$\rho(\epsilon) = \frac{2}{\sqrt{3}\pi}\frac{\epsilon}{t_0^2}. \tag{2.14}$$

In contrast to graphene where the density of states vanishes at the Fermi level (*cf* figure 2.2), CNT have a finite density of states scaling as $1/d_t$.

The simple tight–binding description of the electronic band structure of SWCNT which was shown here makes two approximations:

(a) The Hückel approximation: We consider only the hopping t_0 between nearest neighbours.

(b) The cylindrical geometry of the tubes induces a curvature to the graphene layer. We neglect the change in the hopping integrals and possible hybridization of σ and π orbitals due to curvature.

In reference [25] the hopping terms up to third nearest neighbours have been included into the tight–binding calculations to study the validity of approximation (a) by comparing their results to *ab initio* calculations. They showed that the nearest–neighbour tight–binding model does not reproduce the π graphene bands over a large interval of the first Brillouin zone. Including third nearest–neighbour hopping a much better agreement could be achieved. The conclusion of their work was that the nearest–neighbour tight–binding model works well for the lowest band but higher bands reproduce only qualitatively the real band structure and it is dangerous to use it for quantitative comparison with experiments.

The effect of curvature was studied analytically [26, 27] and also with the help of *ab initio* calculations [17, 25, 28]. The analytical studies use a tight–binding approach, including the fact that the π orbitals are not orthogonal to the tube surface. These calculations suggest that all the CNT, except the ones of armchair type, have a curvature induced gap which scales as $1/d_t^2$ with tube diameter. For

formerly semiconducting tubes this gap adds to the primary gap which scales as $1/d_t$ (*cf* equation (2.11)). A nearest–neighbour tight–binding calculation gives for CNT with zero primary ($n - m = 0$ modulo 3) gap the following equation for the curvature induced band gap [17]:

$$E_g = \frac{a^2}{d_t^2} t_0 \cos 3\theta \qquad (2.15)$$

Again, from this equation we see that there is no curvature induced gap for armchair CNT ($\theta = \pi/6$) due to the symmetry $t_{1\parallel} = t_{2\parallel}$, and zig–zag CNT ($\theta = 0$) acquire a maximal curvature induced gap. This gap scales as $1/d_t^2$. Such a scaling was also found by Kane and Mele using a $\boldsymbol{k} \cdot \boldsymbol{p}$ approximation [26].

The *ab initio* calculations confirm these results for the band gap only partially. The $1/d_t$ scaling of the gap of semiconducting CNT could be confirmed in [17] with local–density functional calculations. But I could not find any confirmation of the $1/d_t^2$ scaling for the curvature induced gap in the literature of *ab initio* calculations. But as the $1/d_t$ scaling law (2.11) for semiconducting tubes, equation (2.15) could also be tested experimentally [29] for meV gaps of zig–zag CNT with $t_0 = 2.6$ meV which is in agreement with the previous estimates. In references [23, 28] it was argued that curvature induced hybridization reduces strongly the band gap of semiconducting tubes. However also these *ab initio* calculations predict a band gap of at least of order 10 meV for all CNT except armchair CNT and the smallest zig–zag CNT.

Chapter 3

The correlation gap in CNT

3.1 Summary

When one comes to think about a new class of materials a fundamental question to ask is if one has to deal with a metal or an insulator. To answer this question we apply the gap criterion (*cf* section 3.2), *i.e.* we investigate if there exist charge carrying single–electron excitations of infinitesimal energy. In the previous chapter we have seen that all CNT except armchair CNT are band insulators. Thus from the band theory point of view armchair CNT seem to be perfect one–dimensional metals. But very general arguments by Mott (*cf* section 3.3) suggest that there should be a single–electron charge gap for one–dimensional systems at half–filling due to electron–electron interaction. It has been argued by Balents and Fisher [30] that this gap, although existent, is exponentially small and thus negligible for all practical purposes in CNT. Their argument is presented in section 3.4. In the main part of this chapter we will argue that the Balents–Fisher result should not be true for CNT at half–filling and that there is a finite gap which cannot be neglected. As an application we show how our results can be used for real CNT and that the gap can be tuned with elastic strain.

Obtained results:

- We predict the scaling law (3.26) of the correlation gap of armchair CNT as a function of tube diameter and Hubbard on–site interactions strength by two different methods (Hartree–Fock and renormalization group).

- We review the model parameters used in the literature for carbon isomers and suggest values to use for CNT.

- We argue that the gap for small armchair CNT could be as large as 10 meV.

- We show that the correlation gap is sensitive to uniaxial strain at a rate of several meV/%.

3.2   The gap criterion

This section follows closely the books by Gebhard [31] and by Mott [32]. The gap criterion is introduced and we discuss under which assumptions it can be used. An insulator and a metal can be distinguished by looking at its zero temperature DC conductivity, *i.e.* the linear response function to a weak applied electrical field

$$\sigma_{\alpha\beta}^{DC}(T=0) \equiv \lim_{T \to 0} \lim_{\omega \to 0} \lim_{|\mathbf{q}| \to 0} \text{Re}\left[\sigma_{\alpha\beta}(\mathbf{q}, \omega)\right] \tag{3.1}$$

where $\sigma_{\alpha\beta}$ is the conductivity tensor. Thus if $\sigma_{\alpha\beta}^{DC}(T=0) = 0$ we have an insulator and otherwise we deal with a metal.

At low temperatures, the conductivity is usually dominated by impurity scattering, other contributions (most importantly from phonons) vanish at $T = 0\,\text{K}$. Up to the scale of the Fermi temperature $T_F = E_F/k_B$, the scattering from impurities gives a temperature independent contribution to the conductivity. This can be shown from microscopic models[1] starting from a Kubo formula for the current–current correlation function:

$$\pi(i\omega_n) = -\frac{1}{3v} \int_0^\beta \mathrm{d}\tau \, e^{i\omega_n \tau} \langle T_\tau \, \mathbf{j}(\tau) \cdot \mathbf{j}(0) \rangle \tag{3.2}$$

The physically relevant retarded function $\pi_{\text{ret}}(\omega)$ is obtained by analytical continuation $(i\omega_n \to \omega + i\delta)$, which is connected to the DC conductivity by

$$\sigma = -\lim_{\omega \to 0} \frac{\text{Im}\left[\pi_{\text{ret}}(\omega)\right]}{\omega}. \tag{3.3}$$

π can be computed, at least approximatively in the limit of small impurity densities, by diagrammatic summation where the important contributions come from ladder diagrams [33]. As it is noted in Gebhard's book [31] there are two conditions which have to be met for a metallic ground state:

1. "Quantum-mechanical states for electron-hole excitations must be available at energies immediately above the energy of the ground state since the external field provides vanishingly small energy $(\omega \to 0)$."

2. "These excitations must describe delocalized charges that can contribute to transport over the macroscopical sample size."

The gap criterion wants to relate the electric conductivity to the *single–particle* excitation spectrum. To do this we have to make the assumption that there is no correlation between the electron and the hole of the electron–hole excitation. Technically speaking, this corresponds to a factorisation of the two–particle

---

[1]See for example, chapter 8 of reference [33].

Green's function into its one–particle components. Under this assumption the elementary excitations of the system are the single–particle excitations and it permits us to draw conclusions about the DC conductivity, a two–particle quantity, from the one–particle spectrum: The zero–temperature gap for single–particle charged excitations gives then a criterion to check if the ground state is metallic or insulating. This is defined with the help of the zero–temperature chemical potentials

$$\mu^+ = E_0(N+1) - E_0(N), \tag{3.4}$$
$$\mu^- = E_0(N) - E_0(N-1), \tag{3.5}$$

the minimal energies needed to add an electron to the ground sate with N (respectively $(N-1)$) particles. Then the gap is given by

$$\Delta = (\mu^+ - \mu^-)_{\text{ext}}. \tag{3.6}$$

The subscript 'ext' indicates the new single–particle state has to be extended so that it can carry current. Then the gap criterion says that we have an insulator if $\Delta > 0$.

However there are some situations where this criterion evidently fails, for instance when electrons, or electrons and holes form bound pairs as it the case in BCS superconductors. Excitons in semiconductors are another example.

3.3 The Hubbard model and Mott's argument

The gap criterion which was described in the previous section will be applied for CNT using the Hubbard model. In this section we will define this model and we reproduce Mott's argument to show that it has all the necessary ingredients to give an accurate evaluation of the gap (3.6) at half–filling.

The Hubbard model on a lattice is defined by the following Hamiltonian[2]:

$$H = \sum_{\langle i,j \rangle \sigma} \left(t_{ij} c_{i\sigma}^\dagger c_{j\sigma} + \text{h.c.} \right) + U \sum_i n_{i\uparrow} n_{i\downarrow} \tag{3.7}$$

σ is the spin index and i, j sum over the sites of a lattice, the symbol $\langle i, j \rangle$ indicates that only terms where i and j are nearest neighbours are taken into account. $c_{i\sigma}^\dagger$ are the fermion creation operators and $n_{i\sigma} = c_{i\sigma}^\dagger c_{i\sigma}$. The first term describes the nearest–neighbour hopping and wants the electrons to delocalise. The second term is the on–site Hubbard repulsion ($U > 0$) which tends to correlate the electronic motion and in some cases even to localise the electrons.

---

[2]The credits for the introduction and the recognition of its importance go to Gutzwiller, Kanamori, Hubbard, Mott and Anderson, *cf* page 61 of reference [31].

Now we want to give an argument that the short-range part of the correlations plays the dominant role when it comes to calculating the correlation gap in half-filled systems. This is most easily seen in the atomic limit where the hopping integrals are assumed to be vanishingly small. So let us assume for a moment that the system is described by the Hamiltonian:

$$H = U \sum_i n_{i\uparrow} n_{i\downarrow} + \sum_{(i,j)} V_{ij} n_i n_j \tag{3.8}$$

where $n_i = n_{i\uparrow} + n_{i\downarrow}$ is the total density, and where V_{ij} is the long-range part of the repulsion that does not need to be specified. According to Mott's prescription to evaluate the gap [32], one has to compare the energy of a uniform configuration with that of a configuration with a doubly occupied site and a hole far apart from each other. The only difference comes from the energy of the electron that has been moved, and the energy increase is precisely equal to U since it still interacts with further neighbours in the same way. So, even in the presence of long-range Coulomb repulsion, the value of the charge gap is controlled by the on-site repulsion U in the atomic limit. Of course, away from the atomic limit, the long-range part of the Coulomb interaction will play a role. To get a quantitative estimate of the charge gap in that case is a very difficult problem though which has not been solved even in the simplest case of a pure one-dimensional model, but if anything the longer range part of the Coulomb repulsion is expected to reinforce the tendency to localize the charge, hence to increase the charge gap. So to use a simple Hubbard model with only on-site repulsion to calculate the correlation gap of a half-filled system is a reasonable assumption, and the value is probably an underestimate of the actual gap in the presence of the long-range part of the Coulomb repulsion. For the present purpose this is all we need since our main conclusion will be to argue that the gap might be larger than previously assumed.

We finish this section with a summary of what is known about the gap (3.6) in the half–filled Hubbard model for the simplest low–dimensional lattices with uniform nearest–neighbour hopping t:

- For the *one–dimensional* chain, the correlation gap can be extracted from the exact Bethe ansatz solution [3]:

$$\Delta = \frac{16t^2}{U} \int_1^\infty \mathrm{d}y \, \frac{\sqrt{y^2 - 1}}{\sinh(2\pi y t/U)} \tag{3.9}$$

  This expression can be used to get the first terms of the asymptotic expansion for weak and strong interactions:

$$\Delta \sim \begin{cases} 8t/\pi \sqrt{U/t} \exp(-2\pi t/U) & \text{for} \quad U \lesssim 2t \\ U - 4t + 8\ln(2)t^2/U & \text{for} \quad U \gtrsim 4t \end{cases} \tag{3.10}$$

---

[3]See for example, chapter 4 of reference [31].

Thus we see that a charge gap opens, inducing a Mott transition at zero coupling.

- In *two–dimensional* lattices the behaviour of the correlation gap depends strongly on the "topology" of the lattice.

  - The *square* lattice is bipartite and its tight–binding dispersion has the perfect nesting property

  $$\epsilon(\boldsymbol{k}) = -\epsilon(\boldsymbol{k} + \boldsymbol{Q}) \quad \forall \boldsymbol{k} \in 1^{\text{st}} \text{ BZ} \tag{3.11}$$

  with nesting vector $\boldsymbol{Q} = (\pi, \pi)$. In two dimensions, this property has the direct consequence that the non–interacting static susceptibility $\chi_0(\boldsymbol{Q})$ shows a logarithmic divergence. The RPA criterion for the onset of the antiferromagnetic instability indicates that there is long range magnetic order for infinitesimal interaction stregth[4]. A Hartree–Fock (H–F) calculation (*cf* section 3.5) gives for small couplings [34]

  $$\Delta \simeq t \exp(-2\pi\sqrt{t/U}). \tag{3.12}$$

  Quantum Monte Carlo simulations confirmed the onset of this instability at infinitesimal U [34–37].

  - The *triangular* lattice is frustrated and has no nesting in its dispersion. Due to frustration the Monte Carlo simulations suffer from the sign problem. Mean field calculations (*cf e.g.* [38] and references therein) suggest that one deals with a "classic" Mott scenario [32] where the magnetic instability and the metal–insulator transition are not at the same U. These calculations give two phase transitions with increasing U, first we go from a non–magnetic semi–metal to a metal with spin density wave ordering, and second to an antiferromagnetic insulator.

  - The *honeycomb* lattice is bipartite, as it is the case for the square lattice, which implies perfect nesting at the Fermi surface. But the Fermi surface of the honeycomb lattice consists of two points only, and moreover, there the density of states vanishes. Thus χ_0 is not logarithmically divergent, and as for the triangular lattice, RPA suggests a metal insulator transition at finite U. However, as a consequence of the bipartite property, the two transitions of the triangular lattice collapse into one, and one finds a direct transition from the semi–metallic state to the antiferromagnetic insulator. One infers from a H–F calculation [39]

  $$\Delta \simeq \begin{cases} 0 & \text{for} \quad U \leq U_{cr}^{HF} = 2.23t \\ \pi\sqrt{3}t^2 \left(1/U_{cr}^{HF} - 1/U\right) & \text{for} \quad U \gtrsim U_{cr}^{HF} \end{cases}. \tag{3.13}$$

---

[4]This calculation is outlined in detail in appendix A for the honeycomb lattice.
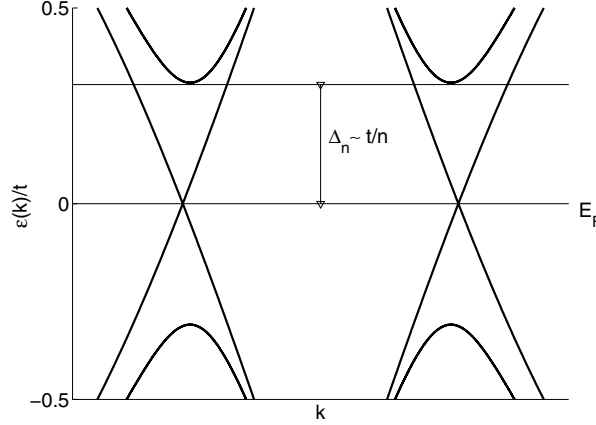
Figure 3.1: The energy bands near the Fermi level for armchair CNT at half–filling.

This scenario is supported by quantum Monte Carlo computations [39–42]. There the gap could not be calculated, but the critical value U_{cr} has been determined by looking at the development of magnetic long-range order, and the value is around $U_{cr} = 3.6t$.

- CNT are between one and two dimensions: Globally they form a one–dimensional structure and therefore one expects a correlation gap for any infinitesimal interaction strength, similar to equation (3.10). On the other hand, one could also say that an electron sitting on the surface of the tube sees it more as a two–dimensional object, the gap is therefore reduced. In the following sections we will discuss this subject in detail and we will try to quantify this reduction to answer the question if armchair CNT at half–filling are effectively insulators or metals.

3.4   The Balents–Fisher result

Already a few years ago, in 1997, Balents and Fisher [30] considered the problem of the correlation gap in half–filled (n, n) armchair carbon nanotubes. To put the problem into a treatable form, they excluded all but the lowest band from their calculation. Checking with figure 3.1, this seems to be a very reasonable assumption, at least at first sight. The distance from the Fermi points to the next band, Δ_n, can be evaluated analytically from the dispersion relation (2.2) with $t_\perp \equiv t_\parallel$ to be

$$\Delta_n = \frac{\pi t_0}{n}, \tag{3.14}$$

leading them to the following conclusion: "Below Δ_n the mode structure is equivalent to a 1D two band model independent of the nanotube size n." The lowest
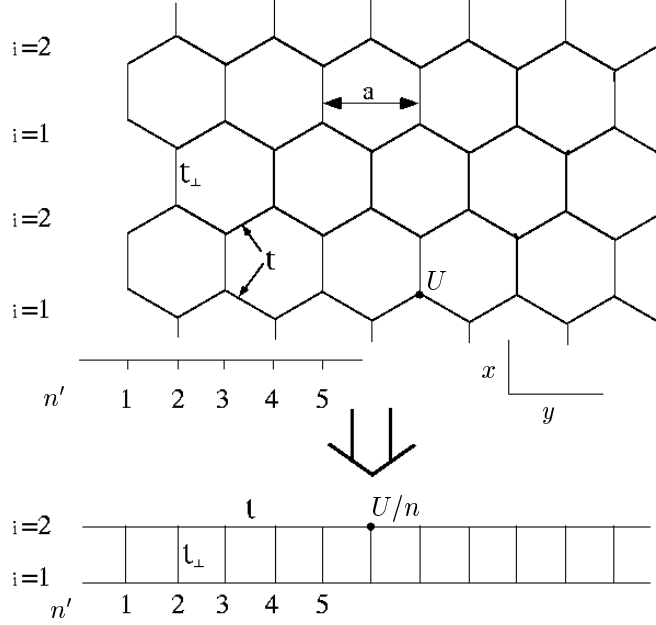
Figure 3.2: Illustration of the relabeling which leads to the effective two–chain Hubbard model. Due to the symmetry of armchair CNT we have $t_{1\parallel} = t_{2\parallel} \equiv t$. This figure was taken from reference [30].

energy modes are given by the $p = 0$ band (*cf* (2.9)) where the wave vectors are given by

$$\mathbf{k} = \frac{q}{2N} \, \mathbf{T}. \qquad (3.15)$$

They are all parallel to the y axis. Thus the space of low–energy states is defined by the states having $k_x = 0$. Balents and Fisher have chosen the following basis for this subspace (*cf* figure 3.2):

$$\phi_{n'1}(x, y) = \begin{cases} n^{-1/2} \, \delta_{y,n'a/2} \, \delta_{x,6\ell a/(2\sqrt{3})} & n' \text{ even} \\ n^{-1/2} \, \delta_{y,n'a/2} \, \delta_{x,(6\ell+1)a/(2\sqrt{3})} & n' \text{ odd} \end{cases} \qquad (3.16)$$

$$\phi_{n'2}(x, y) = \begin{cases} n^{-1/2} \, \delta_{y,n'a/2} \, \delta_{x,(6\ell-2)a/(2\sqrt{3})} & n' \text{ even} \\ n^{-1/2} \, \delta_{y,n'a/2} \, \delta_{x,(6\ell+3)a/(2\sqrt{3})} & n' \text{ odd} \end{cases} \qquad (3.17)$$

These normalised states can be used to expand the field operators in the low–energy sector:

$$c_{i\sigma}^{\dagger} = \sum_{n'\alpha} \phi_{n'\alpha}(\mathbf{r}_i) \, c_{n'\alpha\sigma}^{\dagger} \qquad (3.18)$$

With the help of these new operators we can rewrite the Hubbard Hamiltonian for armchair CNT as the Hamiltonian of the two–chain Hubbard model with

effective interaction U/n (*cf* figure 3.2):

$$
\begin{aligned}
H \;=\; & \sum_{n'\alpha\sigma} \left\{ -t \left(c^{\dagger}_{n'\alpha\sigma} c_{n'+1\alpha\sigma} + \text{h.c.} \right) - t_{\perp} \left(c^{\dagger}_{n'1\sigma} c_{n'2\sigma} + \text{h.c.} \right) \right\} \\
& + \frac{U}{n} \sum_{n'\alpha} c^{\dagger}_{n'\alpha\uparrow} c_{n'\alpha\uparrow} c^{\dagger}_{n'\alpha\downarrow} c_{n'\alpha\downarrow}
\end{aligned}
\tag{3.19}
$$

The reduction of the interaction arises because the electrons have the possibility to delocalise around the circumference of the NT. Effectively they occupy a site i with probability $1/n$. For this model it is known from renormalisation group (RG) calculations (see [30] and references therein) that the functional dependence of the gap Δ on U/n and t is given by

$$
\Delta \sim t \exp[-ct/(U/n)] \qquad \text{if} \quad U/n \ll t.
\tag{3.20}
$$

The constant c and the whole prefactor are unknown. Nevertheless such a behaviour would predict that (n, n) armchair CNT at half–filling with large enough n are metallic for practical purposes since the correlation gap is exponentially small.

In our work we question this conclusion and we argue that the scaling law in equation (3.20) can only be valid, even for large n, if at the same time the interaction strength U is not too large. This can already be seen from the $2D$ limit, i.e. when n approaches infinity. As we have shown in the previous section we expect in this limit a metal–insulator transition at some critical value U_{cr} of the interaction strength. Even at finite n the gap will be exponentially small only up to U_{cr} but will grow linearly for larger values of U. In the following we derive the scaling law of the gap as a function of n and U. In section 3.5 we determine the gap from a H–F calculation where we take into account all the bands. On more qualitative grounds we show in section 3.6 that we can get the same results from a RG argument.

3.5   The correlation gap from H–F calculations

Here we give a summary of the H–F approach which allows us to calculate the correlation gaps in the Hubbard model (3.7) for CNT.[5] In contrast to Balents' and Fisher's calculation this approach includes all the bands. The details of the calculations are outlined in appendix A. Since H–F neglegts completely quantum fluctuations, this approximation will give very poor results in one dimension in general. But when it comes to the correlation gap, H–F is known to reproduce

---

[5] Previously, similar calculations have been done by López Sancho, Muñoz and Chico [43]. They predict a metallic ground state if U is smaller than some critical value. This result will clearly be proved wrong from what follows in this work.

correctly the exponential form of the Bethe ansatz solution (*cf* equation (3.10)):

$$\Delta = 16t \exp(-2\pi t/U) \tag{3.21}$$

The prefactor of the exponential is wrong and the gap is overestimated by a factor $2\pi\sqrt{t/U}$. This is only a problem for very small values of U/t, but we will see in section 3.7 that this is not the range of interest. Thus we expect that H–F gives the exact exponential form for CNT. The H–F value will be an uppper bound to the real value, but of the same order of magnitude for not too small U.

The Hubbard H–F Hamiltonian for CNT at half–filling is

$$H = \sum_{\langle i,j \rangle \sigma} t_{ij} c_{i\sigma}^{\dagger} c_{j\sigma} + \text{h.c.} + U \sum_i \left[n_{i\uparrow} \langle n_{i\downarrow} \rangle + \langle n_{i\uparrow} \rangle n_{i\downarrow} - \langle n_{i\uparrow} \rangle \langle n_{i\downarrow} \rangle \right]$$

with the expectation values given by

$$\langle n_{i\sigma} \rangle = 1/2 \left(1 + m(-1)^i \lambda_{\uparrow\sigma} \right) \tag{3.22}$$

where $\lambda_{\sigma\sigma} = 1$, $\lambda_{\sigma-\sigma} = -1$ and $m = |\langle n_{i\uparrow} \rangle - \langle n_{i\downarrow} \rangle|$. This Hamiltonian can be diagonalized by a Bogoliubov transformation and it yields the self–consistent H–F equation for the sublattice magnetisation:

$$m = \frac{2}{L} \sum_{\boldsymbol{k} \in 1^{st}BZ} \frac{Um}{\sqrt{U^2 m^2 + 4\epsilon^2(\boldsymbol{k})}} \tag{3.23}$$

L is the total number of sites and $\epsilon(\boldsymbol{k})$ is the tight binding dispersion relation (2.2). Finally the gap is obtained from the sublattice magnetisation:

$$\Delta = \min_{\boldsymbol{k}} \sqrt{U^2 m^2 + 4\epsilon^2(\boldsymbol{k})} = Um \tag{3.24}$$

As it was discussed in chapter 2, the armchair CNT are of particular interest since at half–filling they are the only CNT which are truly metallic in the non–interacting electron approximation. We limit therefore our discussion to (n,n) armchair CNT and we put all nearest neighbour hoppings equal t_0. Then we note that for very small interaction strength, the main contribution to equation (3.23) comes from $\boldsymbol{k}$'s around the Fermi points (cf equation (2.12)) and it is straightforward to show that

$$\Delta \propto \exp(-\frac{2\pi}{a} \hbar v_F \, n/U) \quad \text{for} \quad U/t_0 \ll 1. \tag{3.25}$$

In figure 3.3 the numerical results for the correlation gap are shown. We have two parameters to vary, the tube diameter which is proportional to n and the interaction strength U. We tried to fit the H–F results to $c \exp(-\lambda t_0/U)$ when we varied U and to $c \exp(-\lambda n)$ for a variation of n. We see that these fits break down at a critical value of the interaction strength $U_{cr}^{HF} = 2.23t_0$. There is no
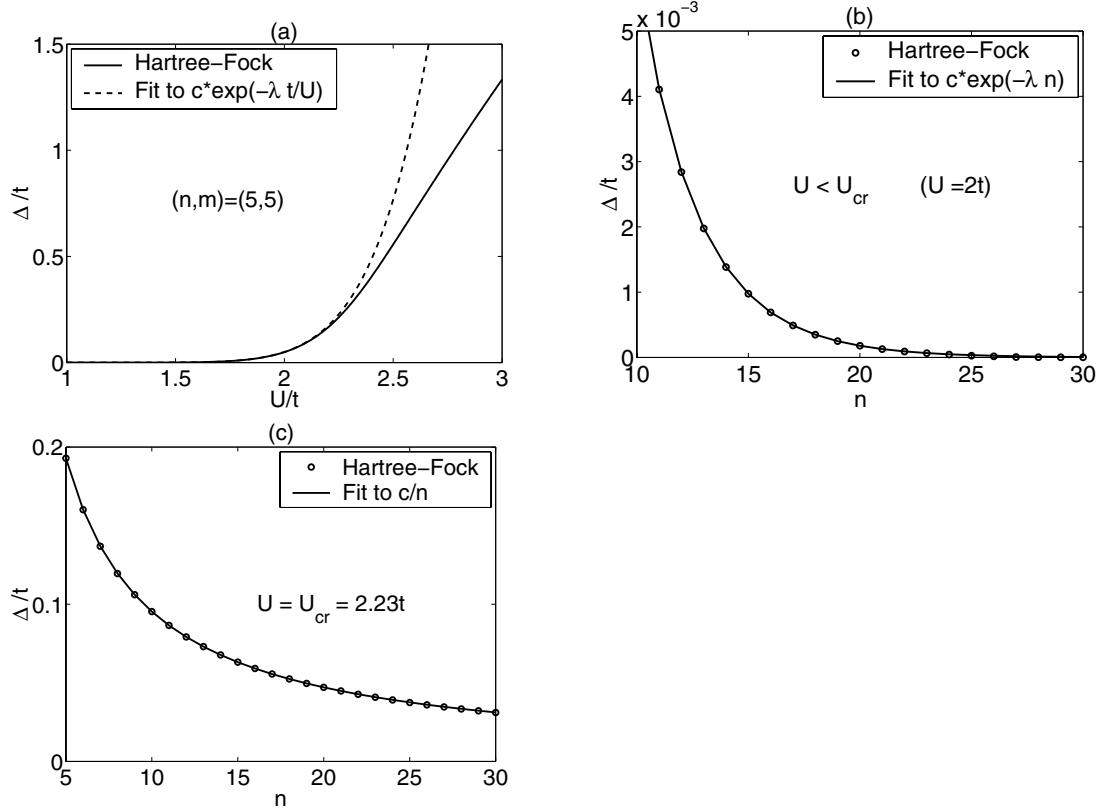
Figure 3.3: Numerical results for the correlation gap: (a) The gap for a $(5,5)$ tube as a function of U. The solid line is the H–F result. The dashed line is the fit to $c \exp(-\lambda t_0/U)$ (c, λ are constants). (b) The gap as a function of the CNT size n at $U = 2t_0$. The H–F results ($\circ$) are fitted to $c \exp(-\lambda n)$ (solid line) (c) The same plot for $U = U_{cr}^{HF} = 2.23t_0$. The data fits the function c/n.

exponential decay beyond U_{cr}^{HF}. In particular for $U = U_{cr}^{HF}$ we can fit the data to c/n, a power law. Combining equation (3.25) and the numerical fits we can write down the following scaling law

$$\Delta/t_0 = c/n \, \exp\left\{-\frac{2\pi}{a}\hbar v_F \, n(1/U - 1/U_{cr}^{HF})\right\} \quad \text{for} \quad U \le U_{cr}^{HF} \qquad (3.26)$$

with $c \simeq 1.01$ and $2\pi/a\,\hbar v_F = \pi\sqrt{3}\,t_0 \approx 5.44\,t_0$. U_{cr}^{HF} is identical to the critical value in the H–F approximation to open a gap in the two–dimensional honeycomb lattice. We see that if U is approaching U_{cr}^{HF} the exponent is going to vanish and we are left with a power law $\Delta = ct_0/n$.

The result of Balents and Fisher (3.20) is recovered in the limit $U \ll U_{cr}^{HF}$ but for values of the interaction strength close to U_{cr}^{HF} the gap is strongly enhanced, even for large n.

3.6 RG–argument

Now we apply an RG argument to show that the scaling law (3.26) is not just an artefact of H–F theory. The basic ideas of the RG approach are developed in appendix B and we are going to use them to find the scaling equation of the gap. In the following we will adopt an even more extreme point of view than Balents and Fisher: We describe CNT as a purely one–dimensional system with hopping t and effective "on–site" repulsion $U/(2n)$. The interaction is reduced since the electrons can disperse around the circumference of the tube. The shortest way around the circumference of a (n,n) armchair CNT passes by $2n$ sites. This allows us to use the RG equations (B.57–B.59) with $g_i(l = 0) = U/(2n) > 0$, $i = 1, \ldots, 4$. In figure B.6 we see that the flow corresponding to these initial couplings falls on the separatrix $2g_2 - g_1 = |g_3|$ and goes to strong coupling. As we have noted there the charge sector and the spin sector completely decouple. Here we are interested in the charge sector only. The g_4 interaction was dropped with the remark that it only renormalises the Fermi velocity [44]:

$$v_F \longrightarrow v_c = v_F + \frac{g_4}{2\hbar\pi/a} \qquad (3.27)$$

Then (B.57–B.58) give one flow equation in the charge sector:

$$\frac{\mathrm{d}g_3}{\mathrm{d}l} = \frac{a}{\pi}\frac{1}{\hbar v_c}g_3^2 \qquad (3.28)$$

By reducing the energy cutoff $E_0(l) = E_0\,e^{-l}$, the flow equation scales towards the strong coupling region. In this region the RG equations are no longer valid and the flow has to be stopped. It has been shown by Larkin and Sak [45] for the Hubbard chain that this should occur when the energy cutoff $E_0(l)$ equals

the energy scale of the charge gap Δ. Following this description, the flow of the running coupling constant has to be stopped at the first relevant new energy scale which enters when we lower the cutoff. In the usual one–band picture this energy scale is just the kinetic energy $\sim t$. But in the present problem there is another energy scale entering before: It is the gap to the next band which is of order $\pi t/n$. Thus we set the boundary conditions to

$$g_3(l_0) \quad \equiv \quad g_0 = U/(2n) \tag{3.29}$$

$$g_3\big(^a/\pi\Delta/(\hbar v_c)\big) \quad \equiv \quad g_c = \pi t/n, \tag{3.30}$$

and we get

$$-\int_{\ln[a/\pi\Delta/(\hbar v_c)]}^{\ln l_0} \mathrm{d}\left(\ln[E_0(l)/E_0]\right) = \frac{\pi}{a}\hbar v_c \int_{g_c}^{g_0} \mathrm{d}g\,\frac{1}{g^2}. \tag{3.31}$$

Doing the integration and neglecting the prefactors we obtain

$$\Delta \quad \sim \quad \exp[^\pi/_a\,\hbar v_c\,(-1/g_0 + 1/g_c)]$$
$$\sim \quad \exp[-2\pi/_a\,\hbar v_F\,n\,(1/U - 1/\gamma)] \tag{3.32}$$

with

$$\gamma = \left(\frac{t}{2\pi} - \frac{a}{4\pi}\frac{1}{\hbar v_F}\right)^{-1} \approx 14.87\,t. \tag{3.33}$$

Thus we find the same exponential form as in the H–F calculation. If one would like to go further and wishes to determine the functional dependence of the prefactor and a more accurate estimate of γ one would have to

1. include two–loop contributions [45] which account for the $\sqrt{U/t}$ factor present in the Hubbard chain.

2. determine the vertex corrections to the coupling constants, taking into account contributions coming from intra *and* inter band interactions [44].

To complete such a program is unfortunately very cumbersome.

3.7   Application to real CNT

In this section we want to discuss the application of the scaling law of the gap

$$\Delta \sim \exp[-2\pi/_a\,\hbar v_F\,n\,(1/U - 1/U_{\mathrm{cr}})] \tag{3.34}$$

to real CNT. This scaling was obtained equally from a H–F (section 3.5) and a RG (section 3.6) calculation. We recall that U_{cr} is identified with the critical value of the interaction strength to open a gap in the two–dimensional honeycomb lattice. The H–F value $U_{cr}^{HF} = 2.23t_0$ is a lower bound to the exact value since
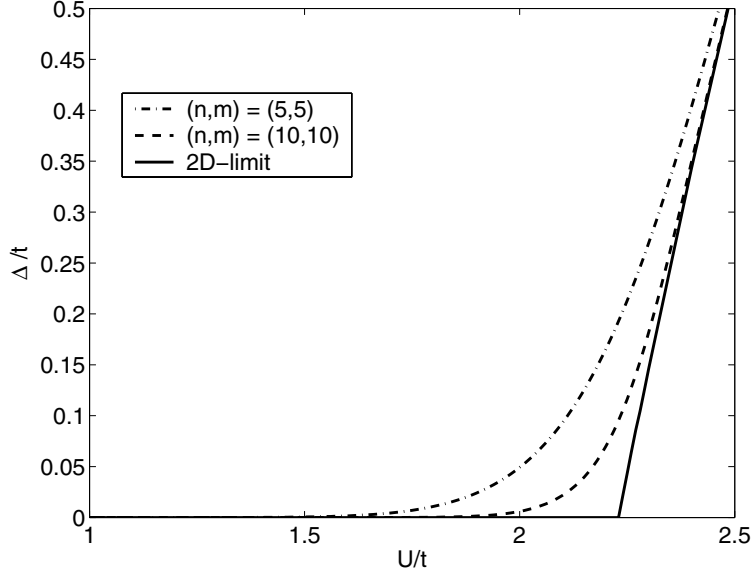
Figure 3.4: The correlation gap as a function of interaction strength for $(5, 5)$ CNT (dot-dashed line), $(10, 10)$ (dashed line) and the 2D–limit (solid line).

H–F neglects all quantum fluctuations. Luckily enough, the Hubbard model on the honeycomb lattice has been extensively studied by Monte Carlo simulations, and although the gap could not be calculated, the critical value U_{cr} has been determined by looking at the development of magnetic long-range order [39–41], and the value is around $U_{cr} = 3.6t$. This is clearly larger than the Hartree-Fock result, but the order of magnitude is the same.

Figure 3.4 summarizes our results obtained from H–F calculations on the correlation gap in armchair CNT. We observe that there is an exponentially small gap only if $U \ll U_{cr}$, even for large n. U_{cr} is a critical value for the interaction strength. For values $U < U_{cr}$ the correlation gap follows an exponential scaling law. For $U > U_{cr}$ the gap is growing linearly. Thus the actual value of the charge gap in CNT depends crucially on the parameter U. What we need here is the atomic value for carbon. The fact that graphite, a system of very weakly coupled honeycomb planes, is a semi-metal and *not* an insulator just tells us that U does not exceed U_{cr}. Besides, values often quoted for fullerenes are of no help since they concern the molecule C_{60} and not the atomic value for carbon.

As we have discussed in chapter 2, t_0 can be extracted from *ab–initio* calculation and experiments. It is known to be $t_0 = 2.5$–2.7 eV. The on–site repulsion U of atomic carbon in CNT is difficult to estimate. The only values we can cite are the ones used in model calculations for other carbon isomers to fit best the experimental data available. In small conjugated molecules the Coulomb interaction between p_z orbitals is unscreened and good results are obtained using the

Ohno potential [46]

$$V(r) = \frac{U}{\sqrt{1 + (r/a_0)^2}} \qquad (3.35)$$

with $U = 11.13$ eV and $a_0 = 1.29$ Å. For larger systems screening will become effective, and the effective on–site repulsion will diminish. For instance, in reference [47] values between $2 \leq U/t_0 \leq 3$ were used for polyacetylene which is a one–dimensional isomer. In the fullerene family, calculations for C_{60} suggest values between 5–12 eV [48,49]. For graphite not much is known. In reference [50] estimates between 6 eV $\leq U \leq 8$ eV are used. These estimates are based on calculations done for coronene molecules [51] which can be considered as a fragment of the graphite layer.

Considering all the values of the on–site repulsion quoted in the previous paragraph, we believe that a value of U close to the critical value $U_{cr} \approx 9$ eV seems plausible. This would mean that the exponential decay of the gap is strongly suppressed. Let us estimate the gap from the H–F equation (3.26). As an example we look at a $(10, 10)$ CNT assuming an interaction strength of $U = 2t$. In this case we obtain for the gap a value of $0.006t_0$ which corresponds to an energy of 15 meV and a temperature of 170 K. For smaller CNT the gap is even larger. Thus a correlation gap of a few meV should be present and a gap of such magnitude could in principle be observed experimentally.

Indeed gaps of order meV have been observed in scanning tunneling microscopy [29] and in two– [52] and four–contact [53] resistivity measurements. These gaps were attributed to curvature effects (*cf* chapter 2), and other tubes were observed to stay metallic down to temparatures of 5 K. This apparant discrepancy between experiments and our theory is resolved by noting that all the currently available CNT seem to be heavily self–doped[6]. Of course our results apply only for SWCNT at half–filling. Away from half–filling metallic behaviour is expected.

3.8   Applying uniaxial strain

As an application of our scaling law (3.26), we calculate the change in the correlation gap of armchair carbon nanotubes with uniaxial elastic strain. We predict that such a stretching will enlarge the correlation gap for all carbon nanotubes by a change that could be as large as several meV per percent of applied strain, in contrast with pure band structure calculations where no change for armchair carbon nanotubes is predicted.

---

[6]This experimental fact was brought to our attention by Lázló Forró. He believes that the Fermi level is usually shifted quite far, so that several bands are crossed. See also references [54,55].
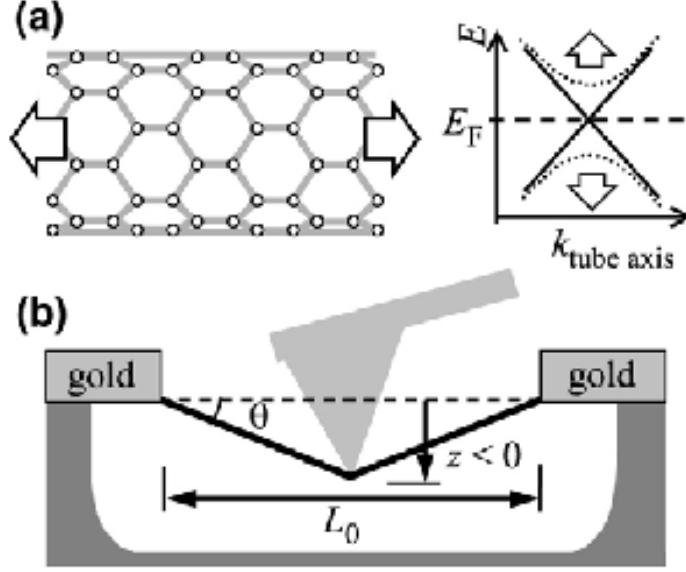
Figure 3.5: (a) Real space representation of a zigzag CNT and the dispersion relation near the Fermi level. Solid lines show the tight–binding bands before and after stretching, respectively. (b) Experimental geometry for applying strain and gate voltage with an AFM tip, and measuring conductance with gold contacts. L_0 is the distance between anchoring points; z is the distance the center of the CNT is displaced from the plane of the anchoring points. Figure and caption are reproduced from reference [58].

Experiments show that CNT can sustain large mechanical strains and can be deformed elastically up to bendings of order 19° which corresponds to a strain along the tube of 5.5% [56]. Experiments and numerical calculations indicate a large Young modulus of order 1TPa [57]. The interaction of mechanical and electronic properties has been studied at room temperature in two experiments [56, 58] where it has been shown that uniaxial stress can change dramatically the electronic structure of CNT. As it is shown in figure 3.5, in these experiments a CNT has been suspended between two metal electrodes on SiO_2/Si substrates. To apply uniaxial stress along the tube the tip of an atomic force microscope (AFM) was used. The tip was lowered to push at the center of the CNT. The AFM allows to measure simultaneously the deflection and the conductance of the CNT. The strain can be defined as $\sigma = \left[\sqrt{4z^2 + L_0^2} - L_0 \right]/L_0$ where L_0 is the suspended length of the tube and z is its vertical deflection. In the first experiment [56] it was shown that changing the strain from 0% to 3.2% let the conductance of a metallic CNT drop by two orders of magnitude. Both the mechanical and the electronic properties were observed to be completely reversible. More recently it was demonstrated [58] that not only metallic CNT become less conducting when

applying stress but also inversely that some samples modified their behaviour from semiconducting to metallic. These experiments show convincingly that uniaxial stress applied to CNT changes their electronic properties.

Theoretically, the effect of strain on the electronic properties of CNT has been studied in band structure calculations, either analytically, using a tight–binding approach, or numerically by density functional theory [26,59–63]. In particular it has been shown that, depending on chirality, uniaxial stress can increase, decrease or not alter the band gap.

With the help of our previous results, we are able to include the effect of electron–electron correlations in these calculations. We compute in detail the gap as a function of applied strain and we compare our results to the one–electron band structure calculations in the literature. Again we use the Hubbard model with on–site interaction only, and the hopping integrals t_{ij} are restricted to near-est neighbors (cf equation 3.7). In general the hopping integrals can have different values in every direction, say $t_\perp$, $t_{1\|}$ and $t_{2\|}$ (cf figure 2.1). We make the reason-able assumption that an applied strain will uniquely change the hopping integrals. Then these three hopping amplitudes and the one–site interaction strength U are the four parameters entering into the model. Choosing some values for them we can determine the charge gap from the H–F equation (3.24) for a given (n, m) CNT.

As discussed in chapter 2 armchair CNT is the only chirality where no band gap opens. Further we will assume that, if there is no applied strain, all the hopping amplitudes are equal to t_0. Of course this is only an approximation since we neglect the curvature of the tube. But for armchair CNT the curvature induces only two different hopping amplitudes, namely $t_\perp$ and $t_\| \equiv t_{1\|} = t_{2\|}$. Due to this symmetry, no gap is opened from the band point of view. However we will show that there will be a gap induced from electron–electron correlation effects for all CNT, even if they are of armchair type.

Following references [59,60] we use Harrison's phenomenological law to relate the hopping parameter t_0 of the undeformed CNT to the ones of the elastically deformed CNT [22] $t_i = t_0 \left(r'_i/r_i \right)^2$ where $\boldsymbol{r'_i}$ and $\boldsymbol{r_i}$ respectively, are the bond vectors before and after the deformation and $i = \perp$, $1_\|$, $2_\|$. Projecting these vectors along the directions of $\boldsymbol{T}$ and $\boldsymbol{C_h}$, we can write for an elastic uniaxial strain along the tube: $r_{iT} = (1 + \sigma) r'_{iT}$ and $r_{iC_h} = (1 - \nu\sigma) r'_{iC_h}$ where ν is the Poisson ratio. The Poisson ratio has been computed numerically [2] and measured experimentally for graphite to be about $\nu = 0.2$ [64].

We verified that for (n, n) CNT with $n = 5, \ldots, 30$ and for an on–site repul-sion in the interval $\left[U_{cr}^{HF} - 0.7t_0, U_{cr}^{HF} \right]$ the scaling law (3.26) is still valid when uniaxial stress σ is applied:

$$E_g/t_\| = c/n \, \exp \left\{ -\alpha n (t_\|/U - t_\|/U_{cr}^{HF}) \right\} \qquad (3.36)$$

The correlation gap, including the strain induced gap, is denoted by E_g. The prefactor c varies only slightly from its original value $c = 1.01$ when we change
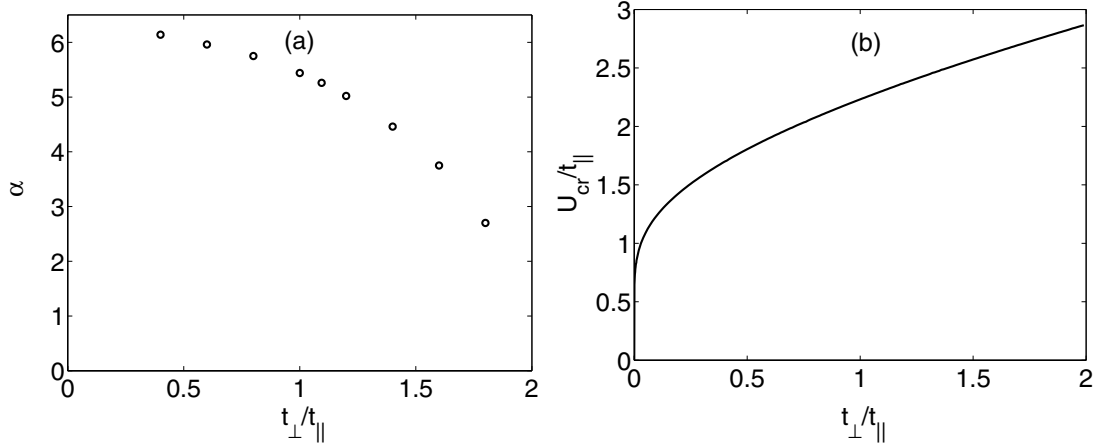
Figure 3.6: Numerical results for the dependence of the parameters α and U_{cr}^{HF} in equation (3.36) on $t_\perp/t_\parallel$: (a) α is extracted from fitting the H–F results to the scaling law (3.36). (b) U_{cr}^{HF} is calculated by evaluating $\chi_0 = \int_{\epsilon<0} d\epsilon \frac{\rho(\epsilon)}{2|\epsilon|}$, the bare staggered static susceptibility, and where $\rho(\epsilon)$ is the tight–binding density of states of the honeycomb lattice. We have shown in appendix A that H–F theory gives $U_{cr}^{HF} = \chi_0^{-1}$.

the ratio $t_\perp/t_\parallel$. The variation of α and U_{cr}^{HF} on the applied strain is much more significant and it is shown in figure 3.6. We observe that U_{cr}^{HF} increases with applied strain. From equation (3.26) we can see that this would imply that the charge gap diminishes since a U far from the critical value disfavours a large gap. However the simultaneous decrease of the parameter α overcomes this tendency and when both effects are taken into account, the charge gap increases approximately linearly with the strain with a slope that depends on U. For small applied strain

$$t_\perp/t_\parallel \equiv 1 + \varepsilon \quad \text{with} \quad \varepsilon \ll 1, \tag{3.37}$$

one can compute the change in the band structure around the Fermi points (*cf* equation (2.12)):

$$\epsilon_{2d}(\boldsymbol{k_F} + \boldsymbol{q}) = \frac{a}{2}\sqrt{3}\, t_\parallel \left(||\boldsymbol{q}|| + \varepsilon \frac{\left(3q_x^2 - q_y^2\right)}{||\boldsymbol{q}||} \right) \quad + \mathcal{O}(\varepsilon^2, q_x^3, q_y^3) \tag{3.38}$$

We see that this calculation still predicts a metal. Further one remarks that strain does not give just a renormalisation of the Fermi velocity, but it deforms the cone of dispersion. In the limit $t_\perp/t_\parallel \rightarrow 0$ we get the one–dimensional behaviour where any infinitesimal electron–electron interaction can open a gap and α takes its value known from the Bethe Ansatz solution, *i.e.* U_{cr}^{HF} tends towards zero and α to 2π. The other limiting point is $t_\perp/t_\parallel = 2$ where the two Fermi points collapse into one and a band gap appears for values $t_\perp/t_\parallel > 2$ which makes the system insulating already for $U = 0$.
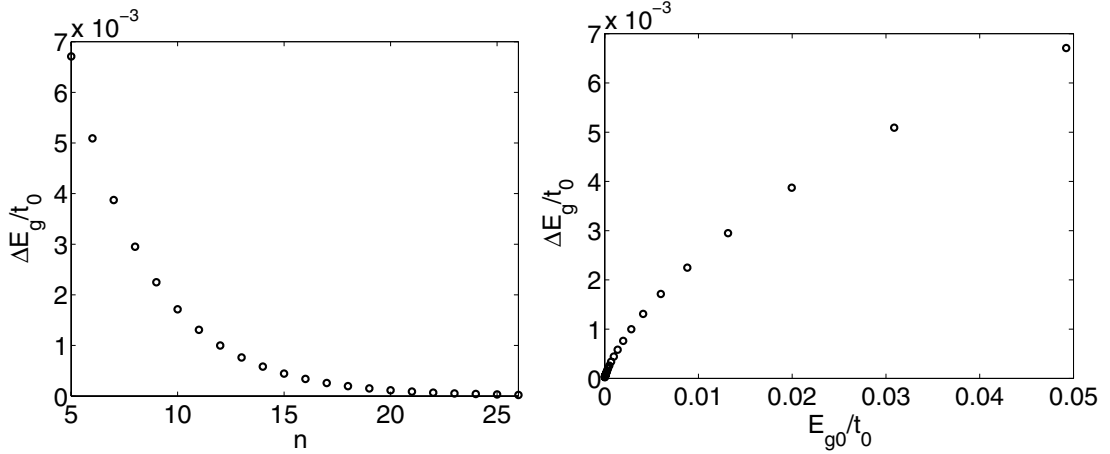
Figure 3.7: The variation of the correlation gap for different (n, n) armchair CNT is plotted when a strain of 1% is applied ($U = 2t_0$). The plot on the left shows the variation of the gap $E_g(\sigma = 1\%) - E_g(\sigma = 0)$ as a function of n. n is proportional to the tube diameter. The right hand side shows the same variation as a function of the original correlation gap at zero applied strain $E_{g0} \equiv E_g(\sigma = 0)$. E_{g0} is calculated for different armchair CNT, $n = 5, \ldots, 26$.

To compare our results to experiments we plot the variation of the gap for armchair CNT as a function of its size when a strain of 1% is applied (cf figure 3.7). The on–site interaction U is set to $2t_0$. As the hopping amplitude t_0 has a large value of 2.5 eV neither the correlation gap at $\sigma = 0$ of order 10 meV nor its variation of order meV per percent of applied strain can be neglected. Taking again the $(10, 10)$ CNT as an example, we can read off from figure 3.7 that the energy gap at zero strain is 15 meV which corresponds to a temperature of 170 K and that a strain of 1% induces a rise of 4 meV in the gap.

How does this compare to the effect of strain to the band structure? For small strains the following formula has been derived from a tight–binding calculation [59]:

$$\frac{\mathrm{d}E_g}{\mathrm{d}\sigma} = \mathrm{sgn}\,(2p + 1)\,3t_0\,(1 + \nu)\cos 3\theta \qquad (3.39)$$

where $p \in \{-1, 0, 1\}$ is defined by the equation $n - m = 3q + p$ (q is integer). This formula has been used to interpret the experimental results in Ref. [58]. It follows from it that the change of the band gap with applied stress can be either positive or negative, depending on the value of q, or in other words the chirality. The maximum variation is achieved for zig–zag CNT (chiral angle zero) and is about ± 85 meV/%. The maximal variation of 85 meV/% is one or even two orders of magnitude larger then the variation of 4 meV/% which we derived from electron–electron correlation. However, for armchair CNT ($\theta = \pi/6$) equation (3.39) and ab initio calculations predict that no gap opens up with applied strain. Then correlation effects are the only reason why one should have a gap and this gap
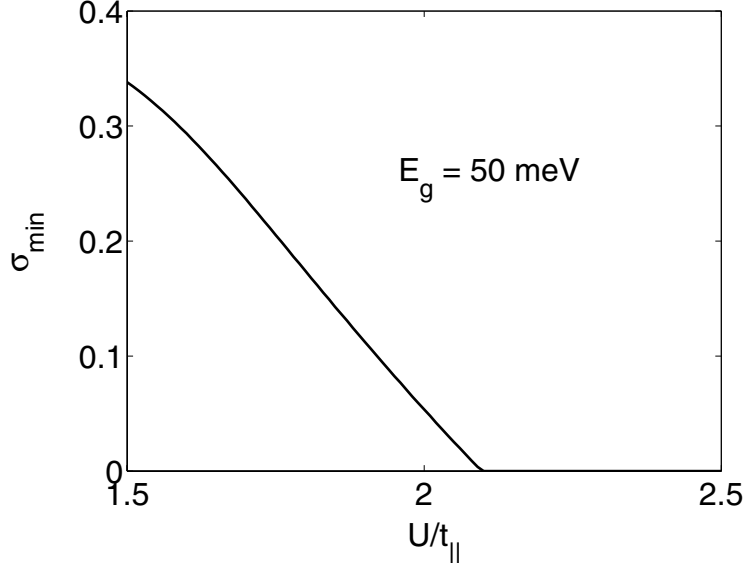
Figure 3.8: Minimal strain σ_{min} necessary to open a gap of $50\,\text{meV}$ as a function of the on–site repulsion U. The calculation was done for a $(10, 10)$ armchair CNT.

increases by applying uniaxial strain at a rate of several meV/%. In our previous example of the $(10, 10)$ CNT, we have seen that one percent of strain can change the correlation gap by about 30% of its original value.

To summarize, for semiconducting CNT with large band gaps the electronic structure at half filling is well described within band theory and correlation effects give only small corrections. But for CNT with a small gap (of several meV or less) correlation effects cannot be neglected. This is especially true for armchair CNT where no band gap at all is predicted but they should develop a measurable gap, induced from correlations alone, if sufficient pressure is applied. This conclusion is illustrated in fig. 3.8. We plot the strain which is necessary to open a gap of $E_g = 50\,\text{meV}$ as a function of the on–site repulsion U for a $(10, 10)$ armchair CNT. We see that if U is not too far from U_{cr} this quite large gap would be realisable experimentally and could be seen in low temperature data.

Chapter 4

Aharonov–Bohm oscillations in CNT

4.1 Summary

This chapter was initally motivated by the experimental observation of oscillations of unexplained periodicities in the magnetoresistance in CNT when a strong magnetic field parallel to the tube axis is applied [53, 65–67]. First we will give an overview of these experiments. Then we start to investigate this theoretically by including a magnetic flux into the tight–binding model of chapter 2 which allows us to exhibit the effects which are present in the one–electron picture. This is done by calculating persistent currents and the conductivity stiffness in a geometry (*cf* figure 4.3) not treated before which seems most relevant to us for experiments which look at electronic transport in tubes with applied longitudinal magnetic field. Successively we include disorder and we outline possible scenarios how to treat electron–electron interactions.

Obtained results:

- In a tight binding calculation perfect tubes at half–filling show always insulating behaviour when a magnetic field is applied longitudinally except around some special fluxes where they become metallic. This happens at $\phi_B = 0$ for armchair CNT and at $\phi_B = {}^1\!/_3\,\phi_0$, ${}^2\!/_3\,\phi_0$ for zigzag CNT because ϕ_B will shift the positions of the lines selected in $\boldsymbol{k}$–space, and each time such a line crosses a K point the bandgap closes. There are however persistent currents around the circumference which are responsible for the large orbital magnetic moment seen in experiments.

- When shifting the Fermi level below half–filling, the conductivity stiffness is always finite (and therefore metallic). The behaviour of the conductivity stiffness versus ϕ_B is non universal, *i.e.* depending strongly on the filling

and also on chirality.

- Experiments show more universality, with resistivity maxima at zero and $\phi_0/2$ flux, suggesting diffusive transport. We showed that disorder can account for such a behaviour. We used the Anderson model to show that the even harmonics of the persistent currents are highly suppressed (Altshuler–Aronov–Spivak effect).

- No signs from the observed small period oscillations have been found. Thus we believe that it should be an effect induced by electron–electron correlations only.

4.2   Experimental overview

In the subsequent sections we will show theoretically that a magnetic field parallel to the tube axis induces $\phi_0 = h/e$ Aharonov–Bohm (AB) oscillations (section 4.3) and $\phi_0/2$ Altshuler–Aronov–Spivak (AAS, section 4.5) oscillations due to impurity scattering. These oscillations have been observed experimentally for CNT. The pioneering work has been done by Bachtold *et al.* [65]. They achieved to contact a single MWCNT to four electrodes to measure the magnetoresistance at low temperatures as a function of the applied field. Their results are shown in figure 4.1. They interpreted their measurement as an observation of the AAS effect, which is the "fundamental" period observed corresponding to $\phi_0/2$. For all their tubes the radius extracted from this period is in good agreement with the one infered from AFM measurement. The authors concluded that this gives strong support that only electrons in the outer shell contribute to conduction. Moreover they observed a very puzzling feature: for some samples there are superimposed oscillations with a much smaller period of about $\phi_0/10$, as it is shown in figure 4.1. They seem to be a characteristic feature in magnetoresistance measurements in CNT, since similar further experiments show also fractional periodicity [66,67]. This effect does not seem to be restricted to MWCNT, Sagnes *et al.* [53] have observed oscillations in SWCNT in pulsed magnetic fields of strength up to 35 T. These CNT had a diameter of 2 nm and thus the AAS period would correspond to a field of 658 T, but the observed oscillations had a period of about 14 T. Although this effect of fractional periodictiy shows up in quite a few experiments, unfortunately, there exists no systematic study which clarify the dependance on tube sizes or chiralities up to now. However the maxima in resistance seem to be systematically at zero flux and $\phi_0/2$. This is observed in all experiments which supports further the assumptions of diffusive transport and the AAS effect. And as it should be, all the measurements are symmetric with respect to the sign change of the magnetic field.

More recently Zaric *et al.* [68] have studied SWCNT in high longitudinal fields (up to 45 T) by absorption and photoluminescence measurements. They
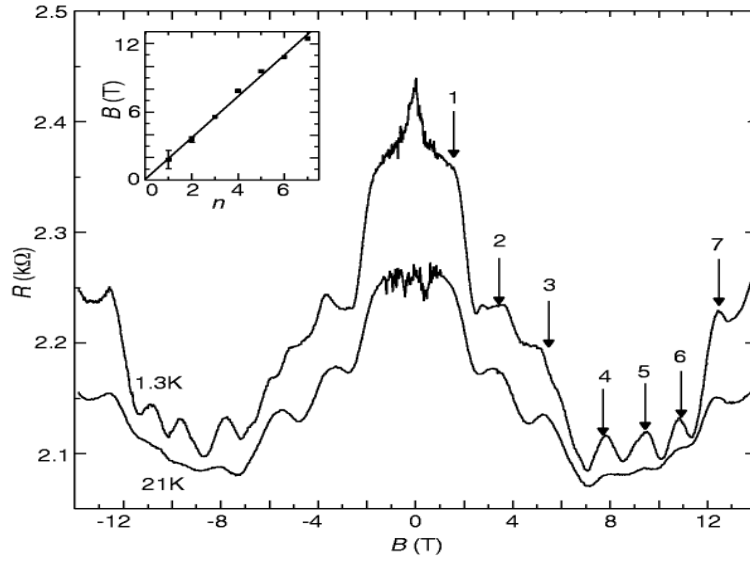
Figure 4.1: "Magnetoresistance measured for a MWNT in a parallel magnetic field B. The general decrease of the resistance from 0 T to ~9 T and the subsequent increase to a possible second maximum (beyond the magnetic field range of the experiment), is assigned to the fundamental oscillation of the AAS effect. In addition, a superimposed oscillation with a much smaller period is clearly visible. Positions of maxima in resistance for this oscillation is periodic with period $\Delta B_{\text{fast}} = 1.8$T. The peak positions agree for both temperatures." Caption and figure were taken from reference [65].

advertise their results as the first verification of the modified Bloch's theorem (4.4). Further they show that their measurments agree with the field dependance of the tight–binding energy gap (4.21–4.22).

At the same time Coskun *et al.* [69] observed Aharonov–Bohm $\phi_0 = h/e$ oscillations in short MWCNT by means of differential conductance measurements. Most excitingly they found an interconversion between semiconducting and metallic states. They claim to succeed in explaining their results using a tight–binding calculation of doped SWCNT (*cf* section 4.4).

Another interesting experiment was done by Minot *et al.* [70]. They measured the orbital magnetic moment of small diameter individual CNT in the presence of a coaxial magnetic field. The observed moments are much larger than the Bohr magneton due to circumferential persistent currents (*cf* section 4.3).

4.3   The Peierls phase and the tight–binding energy bands

Before discussing CNT in a magnetic field, let us start with some general remarks about gauge invariance and the derivation of the (London–)Peierls phase[1]. Ignoring lattice vibrations and relativistic corrections, the Hamiltonian for N electrons in a crystal when a classical magnetic field is applied is given by:

$$
\begin{aligned}
\hat{H} \;=\;& \frac{1}{2m} \sum_{i=1}^{N} \left(\hat{\boldsymbol{p}}_i - e\boldsymbol{A}(\hat{\boldsymbol{r}}_i, t) \right)^2 \\
&+ \sum_{i=1}^{N} V_{\mathrm{p}}(\hat{\boldsymbol{r}}_i) \quad \text{periodic potential of the lattice} \\
&+ \sum_{i=1}^{N} V_{\mathrm{imp}}(\hat{\boldsymbol{r}}_i) \quad \text{interactions with impurities} \\
&+ \sum_{i,j=1}^{N} V_{\mathrm{e-e}}(\hat{\boldsymbol{r}}_i - \hat{\boldsymbol{r}}_j) \quad \text{electron–electron interactions} \qquad (4.1)
\end{aligned}
$$

We note that $\boldsymbol{A}$ is the vector potential of the magnetic field and such a Hamiltionian is gauge invariant, meaning that all physical quantities are independent of the gauge χ chosen:

$$
\begin{aligned}
\boldsymbol{A}'(\boldsymbol{r},t) \;&=\; \boldsymbol{A}(\boldsymbol{r},t) + \boldsymbol{\nabla}\chi(\boldsymbol{r},t) &\qquad (4.2) \\
|\Psi'\rangle \;&=\; e^{i\frac{e}{\hbar}\chi(\boldsymbol{r},t)} |\Psi\rangle &\qquad (4.3)
\end{aligned}
$$

---

[1]This phase factor was originally introduced by Peierls (Z. Physik **80**, 763 (1933)) and London (J. Phys. Radium **8**, 397 (1937)). The derivation given here follows references [71] and [1].

Forgetting about impurities (which break the translational symmetry) until section 4.5 and about electron–electron interactions until section 4.6 (which make the problem infinitely more complicated), we will show how gauge invariance is translated into the tight–binding model of chapter 2.

It was shown by Luttinger [71] that in a *slowly varying* magnetic field the Bloch functions can be expressed as

$$\Psi(\boldsymbol{k}, \boldsymbol{r}) = \frac{1}{\sqrt{L}} \sum_{\boldsymbol{R}_i} \exp\left(i\boldsymbol{k} \cdot \boldsymbol{R}_i + i\frac{e}{\hbar}G_i(\boldsymbol{r})\right) \varphi(\boldsymbol{r} - \boldsymbol{R}_i) \qquad (4.4)$$

where $\boldsymbol{R}_i$ is a lattice vector, L the total number of lattice sites, $\varphi(\boldsymbol{r} - \boldsymbol{R}_i)$ a localized "atomic orbital", and G a magnetic flux phase factor defined by

$$G_i(\boldsymbol{r}) = \int_{\boldsymbol{R}_i}^{\boldsymbol{r}} \boldsymbol{A} \cdot \mathbf{d}\boldsymbol{\xi} \equiv \int_0^1 \mathrm{d}\lambda \, (\boldsymbol{r} - \boldsymbol{R}_i) \cdot \boldsymbol{A}\left(\boldsymbol{R}_i + \lambda(\boldsymbol{r} - \boldsymbol{R}_i)\right). \qquad (4.5)$$

How does the Hamiltonian act on these new Bloch functions ?

$$
\begin{aligned}
\hat{H}\Psi &= \frac{1}{\sqrt{L}} \sum_{\boldsymbol{R}_i} \left[\frac{1}{2m}(\hat{\boldsymbol{p}} - e\boldsymbol{A})^2 + \sum_{i=1}^{N} V_{\mathrm{p}}\right] \exp\left(i\boldsymbol{k} \cdot \boldsymbol{R}_i + i\frac{e}{\hbar}G_i\right) \varphi(\boldsymbol{r} - \boldsymbol{R}_i) \\
&= \frac{1}{\sqrt{L}} \sum_{\boldsymbol{R}_i} \exp\left(i\boldsymbol{k} \cdot \boldsymbol{R}_i + i\frac{e}{\hbar}G_i\right) \left[\frac{1}{2m}(\hat{\boldsymbol{p}} - e(\boldsymbol{A} - \boldsymbol{\nabla}G_i))^2 + \sum_{i=1}^{N} V_{\mathrm{p}}\right] \varphi(\boldsymbol{r} - \boldsymbol{R}_i)
\end{aligned}
$$

One would like that the phase factor G_i cancels the vector potential. When one computes $\boldsymbol{\nabla}G_i$, as it was done in appendix I of reference [71], we see that this happens partially:

$$\boldsymbol{\nabla}G_i(\boldsymbol{r}) = \boldsymbol{A}(\boldsymbol{r}) + \int_0^1 \mathrm{d}\lambda \, \lambda(\boldsymbol{r} - \boldsymbol{R}_i) \wedge \boldsymbol{H}\left(\boldsymbol{R}_i + \lambda(\boldsymbol{r} - \boldsymbol{R}_i)\right) \qquad (4.6)$$

To get rid of the second term we have to make the following two assumptions:

1. The magnetic field is slowly varying compared with the lattice constant a.

2. $\varphi(\boldsymbol{r} - \boldsymbol{R}_i)$ is localized at $\boldsymbol{r} = \boldsymbol{R}_i$.

Then we can write[2]

$$\hat{H}\Psi \approx \frac{1}{\sqrt{L}} \sum_{\boldsymbol{R}_i} \exp\left(i\boldsymbol{k} \cdot \boldsymbol{R}_i + i\frac{e}{\hbar}G_i\right) \left[\frac{1}{2m}\hat{\boldsymbol{p}}^2 + \sum_{i=1}^{N} V_{\mathrm{p}}\right] \varphi(\boldsymbol{r} - \boldsymbol{R}_i). \qquad (4.7)$$

---

[2]Citing Luttinger [71]:"Unfortunately it seems rather difficult within this formalism to make an estimate of the error involved here, and therefore it is impossible to say exactly what the conditions are under which equation (4.7) is valid."

Now we are able to compute the tight–binding matrix elements:

$$H_{\boldsymbol{k}\boldsymbol{k}'} \equiv \left\langle \Psi(\boldsymbol{k}) \left| \hat{H} \right| \Psi(\boldsymbol{k}') \right\rangle = \frac{1}{N} \sum_{\boldsymbol{R}_i, \boldsymbol{R}_j} t_{ij} \exp\left(-i\left(\boldsymbol{k} \cdot \boldsymbol{R}_i - \boldsymbol{k}' \cdot \boldsymbol{R}_j\right) - i\frac{e}{\hbar}\left(G_i - G_j\right) \right)$$
$$(4.8)$$

As a magnetic field breaks translational invariance, Bloch functions with different $\boldsymbol{k}$ vectors are mixed.

Now we will concentrate on the experimental situation described in section 4.2, namely when a constant magnetic field is applied parallel to the tube axis. We recall from chapter 2 that the vector $\boldsymbol{T}$ lies along the tube axis and $\mathbf{C_h}$ describes the circumference of the tube (*cf* figure 2.3). Then the vector potential can be chosen to be

$$\boldsymbol{A} = \frac{\phi_B}{||\mathbf{C_h}||} \; \boldsymbol{e}_{\mathbf{C_h}} \tag{4.9}$$

where $\boldsymbol{e}_{\mathbf{C_h}}$ is the unit vector in the direction of $\mathbf{C_h}$ and $\phi_B = \int \boldsymbol{B} \cdot \mathbf{d}\boldsymbol{\sigma} = \oint \boldsymbol{A} \cdot \mathbf{d}\boldsymbol{\xi}$ is the flux flowing through the tube. It follows immediately that all the longitudinal modes (2.6) are unaffected. They correspond to the one–dimensional translation and are therefore still good quantum numbers. By using the vector potential to determine the flux phase we obtain

$$G_i(\boldsymbol{r}) = \frac{\phi_B}{||\mathbf{C_h}||^2} \int_0^1 (\boldsymbol{r} - \boldsymbol{R}_i) \cdot \mathbf{C_h} \; \mathrm{d}\xi = \frac{\phi_B}{||\mathbf{C_h}||^2}(\boldsymbol{r} - \boldsymbol{R}_i) \cdot \mathbf{C_h} \tag{4.10}$$

and its difference

$$G_i(\boldsymbol{r}) - G_j(\boldsymbol{r}) = \frac{\phi_B}{||\mathbf{C_h}||^2}(\boldsymbol{R}_j - \boldsymbol{R}_i) \cdot \mathbf{C_h}. \tag{4.11}$$

This phase can be absorbed by shifting all the transverse $\boldsymbol{k}$ modes (2.7) by a constant value:

$$\mathbf{C_h} \cdot \boldsymbol{k} = 2\pi p + 2\pi \frac{\phi_B}{||\mathbf{C_h}||\phi_0} \tag{4.12}$$

ϕ_0 is called the *magnetic flux quantum* and defined by

$$\phi_0 = \frac{h}{e} = 4.1357 \times 10^{-15} \; \mathrm{Tm}^2. \tag{4.13}$$

This shows that a constant longitudinal magnetic field can be included in a tight–binding calculation just by shifting the transverse momenta and the tight–binding matrix elements become very simple

$$H_{\boldsymbol{k}\boldsymbol{k}'} = \sum_{\boldsymbol{R}_i} t_{ij} \exp\left[-i\left(\boldsymbol{k} + \frac{2\pi\phi_B}{||\mathbf{C_h}||\phi_0} \; \boldsymbol{e}_{\mathbf{C_h}} \right) \cdot (\boldsymbol{R}_i - \boldsymbol{R}_j) \right] \delta_{\boldsymbol{k},\boldsymbol{k}'}. \tag{4.14}$$

Thus the energy dispersion (2.2) is still valid but the transverse modes are now selected by equation (4.12).
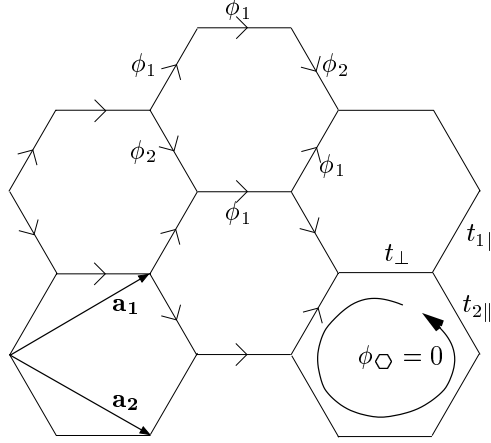
Figure 4.2: A section of a CNT in real space. We put at each link $t_\perp$ or $t_{1\|}$ a flux ϕ_1 and at each link $t_{2\|}$ a flux ϕ_2. An electron which circulate completely once around a hexagon picks up zero flux, $\phi_\bigcirc$ by construction. ϕ_1 and ϕ_2 are determined by the applied longitudinal field $\boldsymbol{B}$ and ϕ_z as shown in figure 4.3.

Of course, the gauge chosen in equation (4.9) is not the only possibility, in the tight–binding model one can make any *local* gauge transformation on the annihilation (and creation) operators of the form

$$c_i \longrightarrow c_i \exp(i\phi_i) \qquad (4.15)$$

which satisfies two conditions:

1. Each time an electron moves around the circumference, it picks up a flux ϕ_B.

2. As the magnetic field is purely longitudinal, the flux passing through any single hexagon $\phi_\bigcirc$ stays zero.

In our calculation we will chose the gauge shown in figure 4.2: We put at each link $t_\perp$ or $t_{1\|}$ a flux ϕ_1 and at each link $t_{2\|}$ a flux ϕ_2. This gauge satisfies evidently condition 2, and condition 1 can be written as

$$2n\phi_1 + m\left(\phi_1 - \phi_2\right) = \phi_B. \qquad (4.16)$$

There are two unknown phases ϕ_1 and ϕ_2, and only one linear relation between them. Therefore we still have some liberty how to chose them. We will use this liberty in the next section to study persistent currents along the tube axis. If we impose periodic boundary conditions the nanotube becomes a torus and persistent currents will induce a flux ϕ_z through the hole (or vice versa) as it is shown in figure 4.3. The flux ϕ_z will fix completely the phases ϕ_1 and ϕ_2:
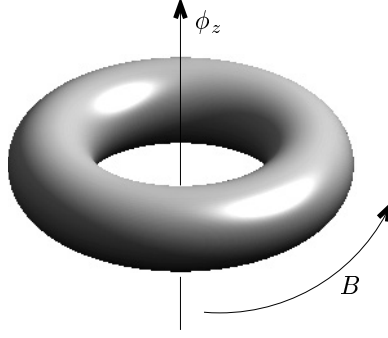
Figure 4.3: Periodic boundary conditions transform the tube into a torus. B is the longitudinal field inside the tube and ϕ_z is the flux inducing (respectively coming from) persistent currents.

$$N\left(2t_1\phi_1 + t_2\left(\phi_1 - \phi_2\right)\right) = \phi_z. \tag{4.17}$$

As before, we consider always the limit of very long tubes, *i.e.* when N is large. With these definitions the tight–binding calculations become trivial again, and we can just use the result of chapter 2, in particular formula (2.2) is still valid if we redefine the hoppings to

$$
\begin{aligned}
\tau_\perp &= t_\perp \exp(i2\pi\phi_1/\phi_0),\\
\tau_{1\parallel} &= t_{1\parallel} \exp(-i2\pi\phi_1/\phi_0),\\
\tau_{2\parallel} &= t_{2\parallel} \exp(i2\pi\phi_2/\phi_0).
\end{aligned}
\tag{4.18}
$$

Then the tight–binding dispersion for graphene becomes

$$
\begin{aligned}
\epsilon_{2d}(\alpha_1,\alpha_2,\phi_1,\phi_2) \;=\; \pm\Big(\;\; & t_\perp^2 + t_{1\parallel}^2 + t_{2\parallel}^2 + 2t_\perp t_{1\parallel}\cos(\alpha_1 - 4\pi\phi_1)\\
& + 2t_\perp t_{2\parallel}\cos(\alpha_2 + 2\pi(\phi_2 - \phi_1))\\
& + 2t_{1\parallel}t_{2\parallel}\cos(\alpha_1 - \alpha_2 - 2\pi(\phi_1 + \phi_2))\Big)^{1/2}.
\end{aligned}
\tag{4.19}
$$

From this equation it is not clear that the energy will show Aharonov–Bohm oscillations in the applied flux ϕ_B of period ϕ_0. But it can be seen when we apply local gauge transformations. As an example let us consider $(n,0)$ (zig–zag) CNT, then the flux ϕ_1 is given by $2n\phi_1 = \phi_B$. For simplicity we put $\phi_z = 0$ which implies $\phi_2 = 0$ for zig–zag CNT. The series of local gauge transformation shown in figure 4.4 will put the whole flux of $2n\phi_1$ at the last link of each zig–zag chain, and all other links have zero flux. This is equivalent to imposing the following boundary conditions for each chain:

$$c_{i=2n+1} = e^{-i2\pi\phi_B/\phi_0}\; c_{i=1} \tag{4.20}$$
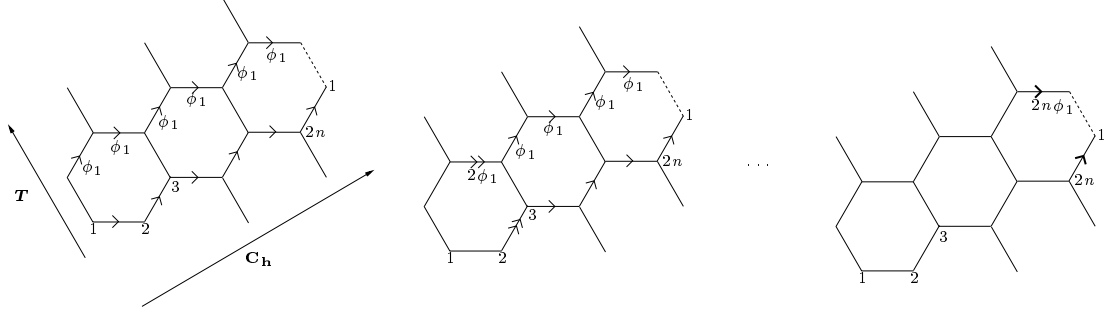
Figure 4.4: A sketch of succesive local gauge transformations $c_j \longrightarrow c_j \exp(i2\pi j \phi_1/\phi_B)$ $j = 1, \ldots, 2n$ where j indicates the site on a zig–zag chain. These transformations are carried out on each chain.

Thus all quantities derived from the tight–binding Hamiltonian show Aharonov–Bohm oscillations of period ϕ_0. As a manifestation of the Ahoronov–Bohm oscillations we show in figure 4.5 the tight–binding band gap as a function of applied magnetic flux ϕ_B for a (5,5) armchair and a (5,0) zig–zag CNT. We see that the gap oscillates, as predicted, with a period of ϕ_0 and there is a field induced metal–insulator transition. This happens because ϕ_B will shift the positions of the lines selected in $\boldsymbol{k}$–space, and each time such a line crosses a K point the gap closes. The tight–binding gap can be approximated by [72]

$$\Delta(\phi_B) = \begin{cases} t_0 \frac{2\sqrt{3}a}{d_t} \frac{\phi_B}{\phi_0} & 0 \leq \phi_B \leq \phi_0/2 \\ t_0 \frac{2\sqrt{3}a}{d_t} \left(1 - \frac{\phi_B}{\phi_0}\right) & \phi_0/2 \leq \phi_B \leq \phi_0 \end{cases} \tag{4.21}$$

if $n - m = 3q$ (q integer) and

$$\Delta(\phi_B) = \begin{cases} t_0 \frac{2\sqrt{3}a}{d_t} \left| \frac{1}{3} - \frac{\phi_B}{\phi_0} \right| & 0 \leq \phi_B \leq \phi_0/2 \\ t_0 \frac{2\sqrt{3}a}{d_t} \left| \frac{2}{3} - \frac{\phi_B}{\phi_0} \right| & \phi_0/2 \leq \phi_B \leq \phi_0 \end{cases} \tag{4.22}$$

if $n - m = 3q \pm 1$. Figure 4.5 shows that these formulae give very good results.

4.4 Persistent currents

We introduce the *persistent current J* and the *conductivity stiffness D* which will be the central quantities of study in this chapter. They have the advantage that one can include effects of quantum interference more satisfactory than in a perturbative calculation for the conductivity. The relation between these quantities will be shown in equation (4.32). To fix the ideas let us consider the Hubbard
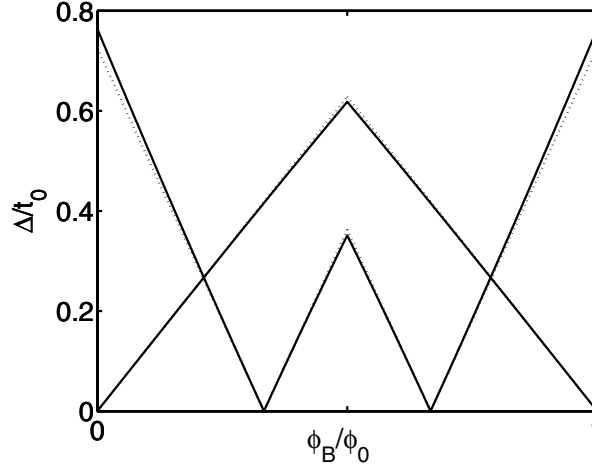
Figure 4.5: The tight–binding energy band gap (solid line) is shown as a function of magnetic flux ϕ_B passing inside the tube. The doted lines are the analytical estimates given in equations (4.21) and (4.22).

model

$$H = \sum_{\langle i,j \rangle \sigma} \left(\tau_{ij} c_{i\sigma}^\dagger c_{j\sigma} + \text{h.c.} \right) + U \sum_i n_{i\uparrow} n_{i\downarrow} \tag{4.23}$$

with the same parametrization of the magnetic flux as before by ϕ_1 and ϕ_2 (*cf* figure 4.2 and equation (4.18)). For the moment we will only consider the persistent current induced along the tube by ϕ_z which is defined as the response of the ground state energy to a finite flux[3]

$$J = \frac{\mathrm{d}E_0}{\mathrm{d}\phi_z}. \tag{4.24}$$

We consider again the example of $(n,0)$ zig–zag CNT. For simplicity we set $\phi_B = 0$ which gives us $\phi_1 = 0$ and $\phi_z = 2N\phi_2$:

$$J = \frac{\mathrm{d}E_0}{\mathrm{d}\phi_2} \frac{\mathrm{d}\phi_2}{\mathrm{d}\phi_z} = \frac{1}{2N} \frac{\mathrm{d}E_0}{\mathrm{d}\phi_2} \tag{4.25}$$

For small ϕ_2 we can develop the Peierls phase (4.18) and we find the perturbed Hamiltonian

$$H' = H(\phi_2 = 0) + \frac{2\pi\phi_2}{\phi_0} j_{\phi_2} - \frac{1}{2} \left(\frac{2\pi\phi_2}{\phi_0} \right)^2 T_{2\|} + \mathcal{O}(\phi_2^3) \tag{4.26}$$

where

$$j_{\phi_2} = i\, t_{2\|} \sum_{\langle i,i+2\| \rangle, \sigma} \left(c_{i\sigma}^\dagger c_{i+2\|,\sigma} - \text{h.c.} \right) \tag{4.27}$$

---

[3] *cf e.g.* reference [73], p. 225.

and

$$T_{2\|} = t_{2\|} \sum_{\langle i, i+2\| \rangle, \sigma} \left(c_{i\sigma}^{\dagger} c_{i+2\|, \sigma} + \text{h.c.} \right).$$ (4.28)

Now we calculate $\langle H' \rangle \equiv \langle 0 | H' | 0 \rangle$ the average in the $\phi_z = 0$ ground state $|0\rangle$. If we assume that $\langle 0 | j_{\phi_2} | 0 \rangle = 0$, we obtain

$$E_0(\phi_z) - E_0(\phi_0) \equiv D \left(\frac{2\pi\phi_z}{\phi_0} \right)^2 + \mathcal{O}(\phi_z^4).$$ (4.29)

D is the conductivity stiffness and in second order perturbation theory it is given by

$$D = \left(\frac{1}{2N} \right)^2 \left[\frac{1}{6} \langle -T \rangle - \sum_{\nu \neq 0} \frac{|\langle 0 | j_{\phi_2} | \nu \rangle|^2}{E_\nu - E_0} \right]$$ (4.30)

where T is the kinetic energy. Then for small flux we can write

$$D = \left. \frac{\mathrm{d}^2 E_0}{\mathrm{d}\Phi^2} \right|_{\phi_z=0} \quad \text{and} \quad J = 2D\,\Phi$$ (4.31)

wher $\Phi = 2\pi\phi_z/\phi_0$. Specifying ϕ_z to $\phi_z^0 \exp(-i\omega t)$, one can use the Kubo formula (3.2) to compute the small–ω behaviour of the real (dissipative) part of the conductivity [74, 75]:

$$\text{Re}\left[\sigma(\omega) \right] = \frac{2\pi e^2}{\hbar} \left[D\delta(\hbar\omega) + \left(\frac{1}{2N} \right)^2 \sum_{\nu \neq 0} |\langle 0 | j_{\phi_2} | \nu \rangle|^2 \, \delta\left((E_\nu - E_0)^2 - \hbar^2\omega^2 \right) \right]$$
(4.32)

Thus D is a measure of the strength of the Drude peak in the conductivity.

As a first example of persistent currents in CNT we plot in figure 4.6 the currents induced by ϕ_B only. These are the currents around the circumference responsible for large orbital magnetic moments predicted by theory [72, 76] and confirmed in experiments [70]. In figure 4.6 we recognize the difference in signs of the currents in zig–zag and armchair CNT. Small zig–zag CNT show an extra oscillation which is suppressed for larger tubes. Such circumferential persistent currents have also been studied by Szopa *et al.* [77, 78] and Sasaki *et al.* [79]. We will not further study these currents since we believe that the geometry most relevant to magnetoresistance measurement is the one shown in figure 4.3 since it enables us to study currents along the tube axis.

Persistent currents in CNT tori have also been investigated in references [80, 81] for the case $\phi_B = 0$. These calculations are relevant to the experiment of reference [82] where rings of SWCNT could actually be built and investigated. But what we want to study here is slightly different. We are interested in the dependence of the persistent currents parallel to the tube axis on the flux ϕ_B which passes through the tube. This persistent current is induced by a virtual
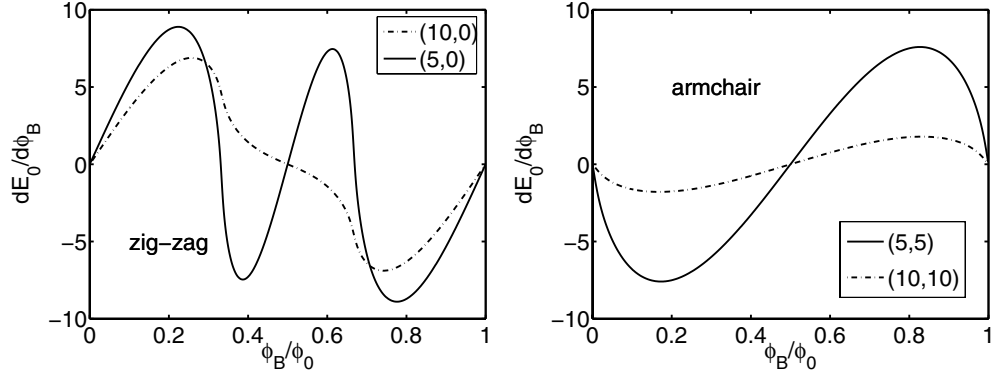
Figure 4.6: We show persistent currents around the circumference of the tube induced by a coaxial magnetic field for zig–zag (left) and armchair (right) CNT.
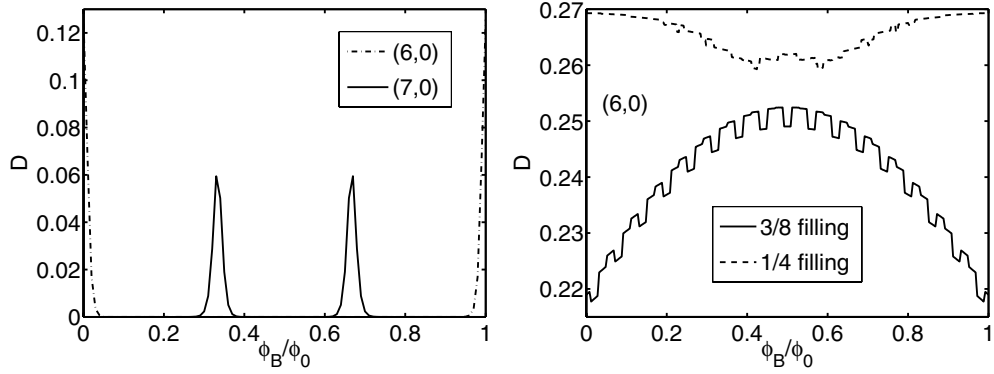
Figure 4.7: We plot the conductivity stiffness D, as defined in equation (4.31), at half–filling (left) and below half–filling (right).

flux ϕ_z. Thus the flux ϕ_z helps us to study currents along the tube axis which would not have been present with ϕ_B only. It is straightforward to calculate numerically the conductivity stiffness in the tight–binding model of the previous section. The results are shown in figure 4.7. We discuss first the case of half–filling shown on the left hand side. We see that the conductivity stiffness is only non–zero if the tube is very close to a metallic state. For example the (7,0) CNT is insulating at zero flux but becomes metalic at $^1/_3$ ϕ_0 and $^2/_3$ ϕ_0. The (6,0) CNT is only conducting at zero flux. This agrees perfectly with the previous results shown in figure 4.5.

Such a behaviour has been observed in experiments *only* for very short tubes and when the chemical potential could been tuned by a gate voltage [69]. In all other experiments such an interconversion between metal and insulator has not been observed. We noted already in chapter 3, and we note it here again,

all available CNT seem to be heavily hole–doped. Therefore we show in the right plot of figure 4.7 the conductivity stiffness of a (6,0) tube for two different fillings below half–filling. We observe that its behaviour depends strongly on the filling and also on chirality (not shown). This is a feature which is not observed in experiments. Experimental investigations [65–67] show a somehow universal behaviour with resistivity maxima at zero and $\phi_0/2$ flux. We will show in the next section how disorder can account for such a behaviour.

4.5 Disorder

The magnetoresistance measurements presented previously seem to be dominated by diffuse tranport showing the Altshuler–Aronov–Spivak (AAS) effect [83]. The AAS effect was originally introduced in 1981 using a diagrammatic perturbation expansion in $1/(k_F l)$ where l is the mean free path. Now we want to give an intuitive picture of this effect, based on a semi–classical argument by Larkin and Khmelnitskii [84].

The semi–classical propagator[4] to go from a space point 1 to another point 2 is given by the following sum over classical paths j

$$A_{12} = \sum_j A_j e^{\frac{i}{\hbar} S_j} \tag{4.33}$$

where S_j is the classical action along the path j and the coefficients A_j are due to the gaussian quantum fluctuations. Then the probability to go from 1 to 2 is

$$P_{12} = |A_{12}|^2 = \sum_i |A_i|^2 + \sum_{i \neq j} A_i A_j \, e^{\frac{i}{\hbar}(S_i - S_j)}. \tag{4.34}$$

The interference terms will usually cancel upon "impurity ensemble averaging". This corresponds to averaging over microscopic realizations of systems with the same macroscopic properties (*e.g* average defect concentration). Of course in real experiments there is only one realisation of the disorder, but in general it is assumed that large enough systems are self–averaging themselves automatically. However if we have time reversal symmetry, *i.e.* no applied magnetic field, there is a large class of trajectories whose contributions do not vanish upon ensemble averaging. These are the pairs of time reversed paths that start and end at the same point. Since these pairs of amplitudes have the same phase they lead to an enhanced probability to return to the initial point, hence implying smaller diffusion and a negative correction to the conductivity. The application of a magnetic field destroys time reversal symmetry and consequently destroys also the phase coherence of the time reversed paths. This translates into a minimum of the conductivity at $\phi_B = 0$. In fact the interference between two time reversed

---

[4]*cf* reference [85] for details.

paths leads to a phase factor of $4\pi\phi_B/\phi_0$. Thus the conductivity will oscillate with the AAS period $\phi_0/2$. If we have a disordered system of many rings (or a cylinder) therefore one always expects to find oscillations of period $\phi_0/2$ and the harmonics corresponding to $q\phi_0$ (q integer) to be suppressed[5].

We will show that we can find evidence for the AAS effect in CNT from microscopic model calculations. The model we use is the Anderson model [87]

$$H = \sum_{\langle i,j \rangle \sigma} \left(\tau_{ij} c_{i\sigma}^\dagger c_{j\sigma} + \text{h.c.} \right) + \sum_{i\sigma} \epsilon_i c_{i\sigma}^\dagger c_{i\sigma} \qquad (4.35)$$

which is the nearest neighbour tight–binding model studied previously and an additional term due to disorder. The disorder is modeled by on–site energies ϵ_i chosen randomly in the interval $[-W/2, W/2]$. This random energies destroy completely the translational invariance of the model and it has been argued already in Anderson's original paper, and confirmed afterwards in many calculations, that large disorder (large W compared to the bandwith) would lead to localization of the electronic states and eventually to a metal insulator transition at some critical disorder strength W_c.[6] This scenario happens in *three* space dimensions but if we lower the dimensionality the effect of disorder on free electrons becomes even more pronounced. In *two* dimensions it is predicted that free electrons are always localized but the localization length can be very large [88]

$$\xi_{\text{loc}} \sim l \exp(\frac{\pi}{2} k_F l). \qquad (4.36)$$

In contrast in *one* dimension the localization length is of the same order as the mean free path l, *i.e.* the electrons become localized already after a few back and forth scattering impacts. To summarize, in one dimension some simple back and forth bumping leads to localization whereas in higher dimensions much more subtle interference effects can occur. We discussed the AAS effect as an example.

CNT live between the one– and two dimensional world and we will try to study the interference effects due to disorder here. The plots in figure 4.8 show that for large enough disorder W the even harmonics of the Fourier decomposition of the conductivity stiffness

$$D = \sum_{n=0}^{\infty} D_n \cos(n2\pi\phi_B/\phi_0) \qquad (4.37)$$

are highly suppressed upon impurity ensemble averaging whereas the odd harmonics tend to finite values. Moreover the conductivity stiffness for $\phi_B = 0$ and

---

[5]Some references to non–CNT experiments demonstrating this effect can be found in Imry's book [86], section 3.2.

[6]Localization means that the wave functions decays exponentially with a characteristic length scale ξ_{loc}. For a general discussion and references on this topic see chapter 2 of Imry's book [86], and page 271 of Reference [73].
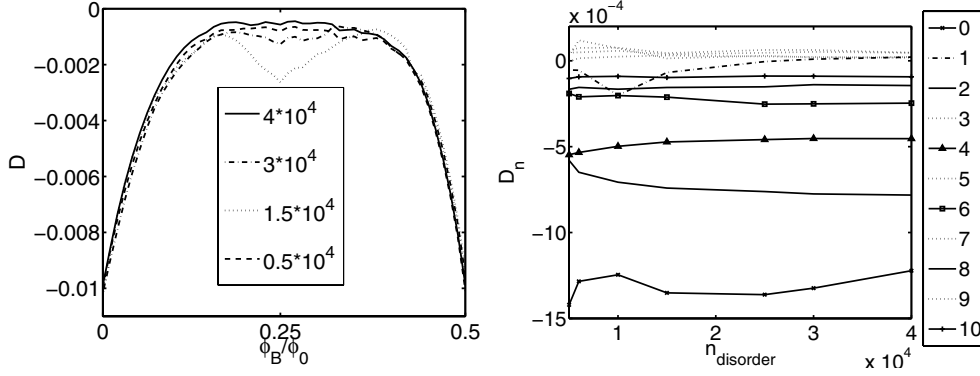
Figure 4.8: We show the conductivity stiffness (4.31) for a (4,0) zig–zag CNT of length $N = 4$ computed from the Anderson model (4.35) with disorder strength $W = 5t_0$ and at an electronic filling of 0.234. The different curves indicate different numbers of microscopic realizations which were used for the impurity ensemble averaging. On the right hand side the first ten components of the Fourier decomposition $D = \sum_{n=0}^{\infty} D_n \cos(n2\pi\phi_B/\phi_0)$ are plotted.

$\phi_B = 0.5$ are negative and minimal, indicating a negative contribution to the persistent current and therefore resistivity maxima for these fluxes as it was observed in experiments. We investigated zig–zag CNT with different diameters and for different fillings (below half–filling) and always this behaviour was observed for large disorder srength of $W = 5t_0$. Some of these calculations are shown in figure 4.9. We have not done this calculations for other chiralities but we do not believe that these results are sensitive to chirality if we consider strong disorder and fillings far below half–filling such that the Fermi level cuts many bands. We mention that the suppression of even harmonics has been observed in similar calculations on the square lattice by Bouzerar and Poilblanc [89, 90].

4.6 Electron correlations

Up to now, we did not find any trace of the "mysterious" fast period oscillations which were observed in different experiments. Thus one is tempted to believe that it is an effect induced by electron–electron correlations only.[7] Unfortunately one has to be careful since, if disorder is important, it cannot be treated as a small perturbation to interactions in general. But to treat disorder and interactions at the same footing is an extremly difficult problem. We conclude this chapter with an outline of possible (tractable?) approaches to the problem.

---

[7]We have to note that the cleanest experimental evidence comes from measurements in MWCNT [65]. Although the ϕ_0 oscillations are compatible with transport in the outer shell, one cannot exclude "multi–wallness" as another source of additional oscillations.
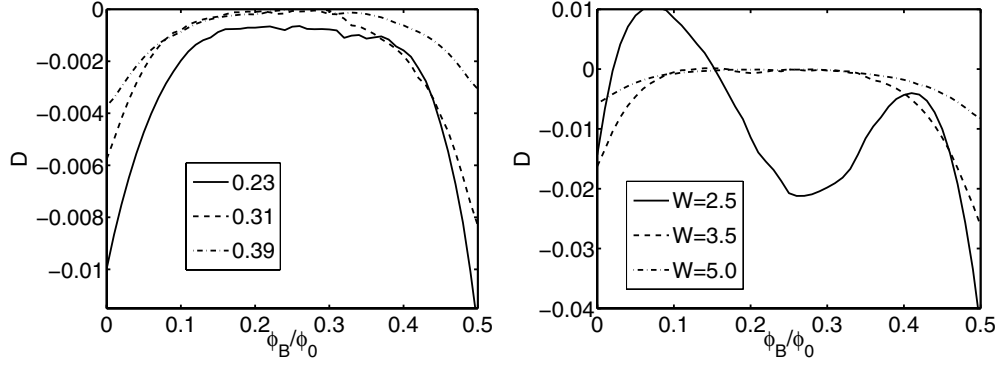
Figure 4.9: This figure shows the conductivity stiffness D for a (4,0) zig–zag CNT of length $N = 4$. At the left hand side, D is plotted for different electronic fillings at a disorder strength of $W = 5t_0$. The right hand side shows the influence of the disorder strength W at a filling of 0.23.

- Starting with a proposition from reference [53] to use a phenomenological Luttinger–Liquid theory[8] which is believed to dominate the metallic phase away from half–filling in CNT. In a Luttinger liquid spin and charge excitations are completely decoupled and therefore they can propagate with different velocities v_s and v_c repectively. At a semi–classical level one could imagine that once injected at one end of the tube they make a different number of loops around the circumference before arriving at the same time at the other end of the tube. This could induce a fast period oscillations depending on the ratio v_s/v_c. Jagla and Balseiro [91] have applied this phenomenological Luttinger liquid theory to small one–dimensional rings with two contacts. Indeed they found small period oscillations as a function of flux passing through the hole of the ring if the velocities satisfy $v_s/v_c = p/q$ where p and q have to be small odd integers. Such an approach would be possible to use for CNT.

- Aharonov–Bohm type oscillations of higher periods seem to be a well established result in the one–dimensional hole–doped Hubbard model which was found either by analyzing the Bethe ansatz equations [92] or doing exact diagonalization studies [93]. However there are serious drawbacks to apply these results to CNT. None of these methods are generalizable to several chains and moreover these oscillations appear uniquely for huge interactions strengths.

- If one believes that disorder *and* interactions play a crucial role and one wants to do a microscopic model calculation, then again, the only tractable

---

[8]*cf* chapter 3 of reference [73].

approach to CNT seems to be a H–F approximation. This approach was used previously for a square lattice rolled up to a cylinder [89, 90]. The authors showed that the second harmonic of the persistent current is enhanced by the interactions (of Hubbard and nearest neighbour type). Solving the self–consistent H–F theory is quite a heavy numerical calculations and therefore one is restricted to lattices of the order ~ 100 sites.

At the moment no worked out solution can be presented to any of these propositions. Therefore no conclusive explanation on the origin of the fast period oscillations is given in this thesis.

Chapter 5

The spin gap in CNT

5.1 Summary

We study the isotropic Heisenberg model for CNT by quantum Monte Carlo (QMC) simulations (*cf* appendix C). As the honeycomb lattice is bipartite these calculations do not suffer from the sign problem and many quantities can be calculated exactly with relatively small statistical error bars, even in the limit of low temperatures and large system sizes. In particular we calculate the spin gap for the smallest CNT (up to six legs) by two different methods: It can be determined either from a fit to the low–temperature magnetic susceptibility (section 5.3) or from the dynamical correlation function of the staggered magnetization in imaginary time (section 5.4).

At the end of this chapter we discuss what implications our results could have for real CNT, especially for the observed superconductivity.

Obtained results:

- All CNT develop a spin gap which decreases fast with tube diameter.

- Rule of thumb: For a given diameter, armchair CNT have larger gaps than zigzag CNT.

- The value of the gap correlates with the maximum difference in bond strength.

5.2   Heisenberg ladders and CNT

In this chapter we study the antiferromagnetic Heisenberg model[1] for CNT which is defined by the Hamiltonian

$$H = J \sum_{\langle i,j \rangle} \underbrace{\left[S_i^z S_j^z + \frac{1}{2} \left(S_i^+ S_j^- + S_i^- S_j^+ \right) \right]}_{\boldsymbol{S}_i \cdot \boldsymbol{S}_j} - \underbrace{g\mu_B B}_{h} \sum_i S_i^z \qquad (J > 0). \qquad (5.1)$$

The first term is the sum of Ising and spin–flip terms. The second term consists of an additional Zeeman term which couples the spins to a uniform external magnetic field which lies in the z direction and has an amplitude B. $g \simeq 2$ is the gyromagnetic ratio and $\mu_B = \frac{e\hbar}{2m} \simeq 5.8$ eV/T the Bohr magneton.

The Heisenberg model can be viewed as the effective low energy model of the Hubbard model (3.7) in the large U limit at half–filling (*cf* also section 6.2). The Heisenberg exchange coupling is related to the on–site interaction through $J = 4t^2/U$. In this limit, there will be exactly one electron per site in the ground state of the half–filled system as it is energetically very unfavorable to move a charge to form a doubly occupied site. Therefore there are no low–energy charge excitations and only the spin degrees of freedom are important. This brings considerable simplification for numerical calculation as the number of states has been reduced from four to two states per site. Consequently much larger systems can be studied.

In chapter 3 we have discussed extensively how the charge gap develops from one to two dimensions by increasing the tube diameter. Now we want to do the same interpolation for the spin gap. That this could be a more subtle problem is expected by analogy with the spin ladders which interpolate between the single chain and the square lattice (with open boundary conditions in one direction).[2] However this interpolation is far from being smooth in the case of spin ladders: Ladders with an odd number of legs have no spin gap and are critical in the sense that their spin–spin correlation functions decay with a power law. However there is a finite spin gap if the number of legs is even and therefore the spin–spin correlation functions decay exponentially with distance. This behaviour has been verified numerically doing quantum Monte Carlo simulations [95] and can be explained by field theoretical arguments using bosonization (*cf e.g.* [73], p.191 *ff*). Schulz [96] pointed out that the n leg ladders are intimately connected with the spin $S = n/2$ chains. This is in good agreement with Haldane's famous result which says that integer spin chains develop a spin gap whereas half–integer ones do not (*cf e.g.* [97]).

---

[1]A nice pedagogical introduction to the physics of the Heisenberg model can be found in Fazekas' book [94], chapter 6.

[2]References and an introduction to spin ladders, especially from a field theoretical point of view, can be found in Giamarchi's book [73], p. 188 *ff*.
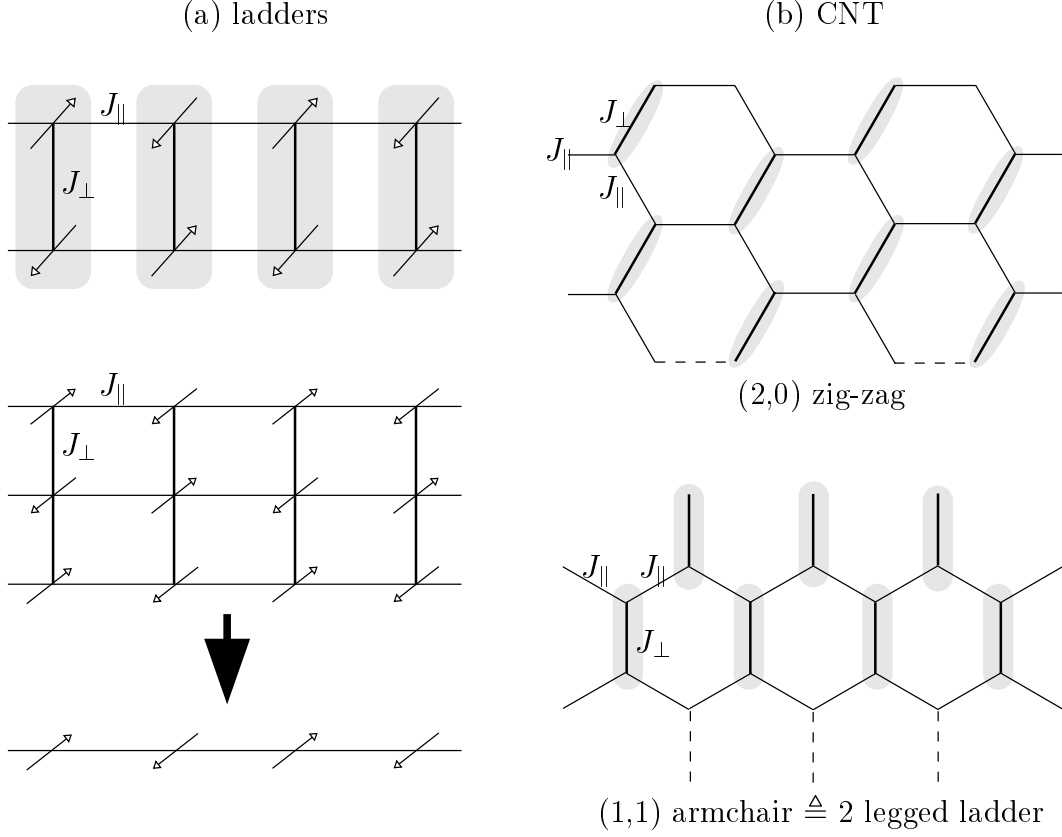
Figure 5.1: We sketch the ground state of the antiferromagnetic Heisenberg model in the limit $J_\perp \gg J_\parallel$. (a) In even legged ladders singlets can be formed on all the rungs simultaneously. In odd legged ladder this is not possible, and one spin per rung remains unbound. (b) CNT can always be covered with singlets since the unit cell of the honeycomb lattice consists of two atoms. We note that the (1,1) armchair CNT is nothing else than the two–legged ladder.

To get a simple grasp of what is going on in the two–legged spin 1/2 ladders we look at the limit where the transverse coupling $J_\perp$ on the rungs is much stronger than the longitudinal coupling $J_\parallel$ along the legs (*cf* figure 5.1 (a)). As $J_\perp$ is the dominant coupling, the system will try to minimize the bond energy of the rungs:

$$
\begin{aligned}
E_{\text{rung}} &= J_\perp \boldsymbol{S_1} \cdot \boldsymbol{S_2} = J_\perp/2 \left[(\boldsymbol{S_1} + \boldsymbol{S_2})^2 - \boldsymbol{S_1}^2 - \boldsymbol{S_2}^2 \right] \\
&= J_\perp/2 \left(\boldsymbol{S_1} + \boldsymbol{S_2} \right)^2 - J_\perp S(S+1) \\
&= \begin{cases} -{}^3\!/_4 \, J_\perp & \text{singlet state} \quad (|\boldsymbol{S_1} + \boldsymbol{S_2}| = 0) \\ {}^1\!/_4 \, J_\perp & \text{triplet state} \quad (|\boldsymbol{S_1} + \boldsymbol{S_2}| = 1) \end{cases}
\end{aligned}
\tag{5.2}
$$

The ground state is expected to be the product of singlet states on the rungs and to have a gap towards triplet excitations of order $J_\perp$. In this limit it is easy to see that the three legged ladder has a qualtitatively very different behaviour: As

it is impossible to form a singlet state out of three spins 1/2, two of the three spins on each rung will be locked into a singlet and the third spin remains free. This suggests that the physics of the three legged ladder will resemble the single chain behaviour.

The situation for CNT will be quite different. The unit cell of the honeycomb lattice contains two sites and therefore it is always possible to have a singlet covering in the limit $J_\perp \gg J_\parallel$, as it is shown exemplarily in figure 5.1 (b). Thus an odd–even effect, which is present in the ladders, is not expected for CNT.[3] A priori it is not clear what will happen if $J_\perp \to J_\parallel$. This question and especially the dependance of the spin gap on chirality will be studied in the subsequent sections. However we should not forget that the behaviour in the two dimensional limit is known: The ground state of the antiferromagnetic Heisenberg model on a two dimensional bipartite lattice (such as the honeycomb or square lattice) has Néel type long range order (*cf e.g.* [99]). This means that SU(2) symmetry is spontaneously broken and for this reason Goldstone's theorem predicts gapless excitations with a linear dispersion.[4]

5.3   The spin gap from susceptibility

We determine the spin gap for the smallest CNT from the uniform susceptibility as it was done in reference [101] for spin ladders. The susceptibility is computed using the stochastic series expansion QMC algorithm described in–depth in appendix C. The spin gap can be extracted from a fit at low temperatures. To see how this works, we write down the free energy $F = -1/\beta \ln Z$ at low temperatures, *i.e.* for $k_B T \ll \Delta$. To evaluate the partition function at low temperatures, we assume that the low energy excitations are given by collective triplet excitations with dispersion $\epsilon_{\boldsymbol{k}} + \sigma h$, where $\sigma = -1, 0, 1$. Then we obtain

$$F \;=\; -\frac{1}{\beta} \ln \left\{ 1 + [1 + 2\cosh(\beta h)] \sum_{\boldsymbol{k}} e^{-\beta \epsilon_{\boldsymbol{k}}} \right\} \tag{5.3}$$

$$\approx\; -\frac{1}{\beta} [1 + 2\cosh(\beta h)] \sum_{\boldsymbol{k}} e^{-\beta \epsilon_{\boldsymbol{k}}}. \tag{5.4}$$

As it was done for the spin ladders [95, 101], we will assume that the dispersion is quadratic around its minimum:

$$\epsilon_{\boldsymbol{k}} = \Delta + a \left| \boldsymbol{k} \right|^2 \tag{5.5}$$

---

[3]Very recently Matsumoto *et al.* [98] have also studied spin CNT. They do not give numerical values for the gap but they predict chirality dependent spin gaps for all CNT.

[4]*cf e.g.* the book by Peskin and Schroeder [100], p 351*f*.
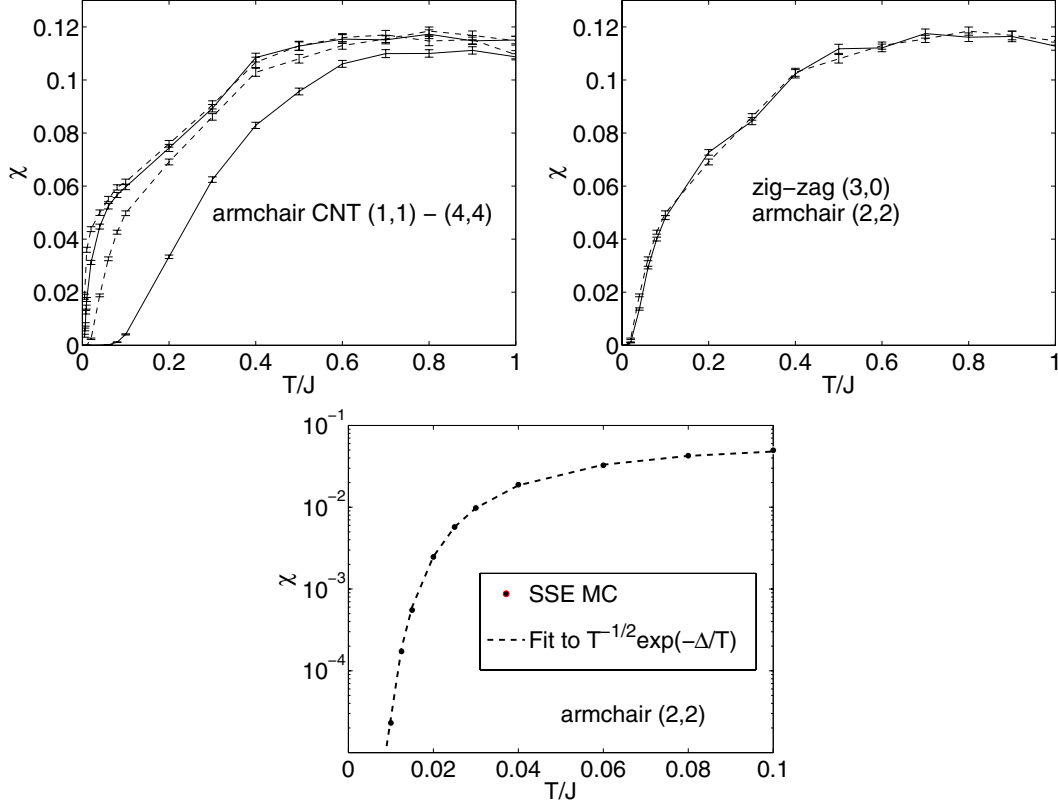
Figure 5.2: The uniform susceptibility χ (in units of $J(g\mu_B)^2$) as a function of temperature from QMC simulations is plotted for the smallest armchair CNT in the upper left corner. The upper right corner shows the same plot but compares the (3,0) zig–zag and the (2,2) armchair CNT. Below we show the low temperature fit for the (2,2) armchair CNT. The error bars are smaller than the symbols.

For low temperatures it is safe to replace the sum by an integral and to extend the integration up to infinity:

$$\sum_{\boldsymbol{k}} e^{-\beta\epsilon_{\boldsymbol{k}}} \approx \frac{1}{2\sqrt{\pi}}(a\beta)^{-1/2}e^{-\beta\Delta} \qquad (5.6)$$

The uniform magnetic susceptibility is then given by

$$\frac{\chi}{(g\mu_B)^2} = -\frac{1}{L}\left.\frac{\partial^2}{\partial h^2}F\right|_{h=0} \approx \frac{1}{2\sqrt{\pi a}}(k_B T)^{-1/2}e^{-\Delta/(k_B T)}. \qquad (5.7)$$

This formula will be used to fit the low temperature susceptibility obtained from QMC simulations. Such a fitting procedure will give immediately the value of the gap Δ. In figure 5.2 we show the susceptibilities for the smallest armchair CNT and also that the behaviour of the susceptibility does not depend on chirality

but seems to be determined uniquely by the value of the gap. From table 5.1 we read off that the armchair (2,2) and the zig–zag (3,0) CNT have nearly the same gap and its susceptibility versus temperature plots (figure 5.2) are close to be indistinguishable, not only at low temperature but throughout the whole temperature range. From the lower plot of figure 5.2 we see that the low temperature behaviour can be fitted nicely to equation (5.7). The values for the energies per site and the gaps for all CNT up to six legs are collected in table 5.1. In the following section we show that the SSE algorithm allows to compute the spin gap still by another method. Afterwards we will try to understand the chirality dependence of this gap.

5.4 The spin gap from imaginary time correlations

Here we present another method to compute the spin gap. We do this for two reasons: first this allows us to confirm the values of the previous section, and secondly the following method can give more precise results. It is however computationally much more complicated, and one is restricted to smaller systems.

We have shown in appendix C that the SSE algorithm permits also to compute dynamical correlation functions such as the staggered magnetization in imaginary time:

$$C(\tau) = \frac{1}{L^2\beta} \sum_{i,j=1}^{L} \int_0^\beta \mathrm{d}t \left\langle (-1)^{|i-j|} S_i^z(t) S_j^z(t+\tau) \right\rangle \tag{5.8}$$

Now we want to exhibit the gap from this correlation function.[5] We do a formal expansion of equation (5.8) in the eigenfunctions of the Hamiltonian $H \left| \Psi_n \right\rangle = E_n \left| \Psi_n \right\rangle$ which form a basis set of the Hilbert space $(\sum_n \left| \Psi_n \right\rangle \left\langle \Psi_n \right| = \mathrm{Id})$:

$$
\begin{aligned}
C(\tau) &= \frac{1}{L^2\beta Z} \sum_{i,j=1}^{L} \int_0^\beta \mathrm{d}t \sum_n \left\langle \Psi_n \right| e^{-\beta H} (-1)^{|i-j|} S_i^z(t) S_j^z(t+\tau) \left| \Psi_n \right\rangle \\
&= \frac{1}{L^2\beta Z} \sum_{i,j=1}^{L} (-1)^{|i-j|} \int_0^\beta \mathrm{d}t \sum_{n,m} \left\langle \Psi_n \right| e^{-\beta H} e^{-tH} S_i^z e^{tH} \left| \Psi_m \right\rangle \\
&\qquad\qquad\qquad\qquad\qquad\qquad \times \left\langle \Psi_m \right| e^{-(t+\tau)H} S_j^z e^{(t+\tau)H} \left| \Psi_n \right\rangle \\
&= \frac{1}{L^2 Z} \sum_{n,m} \sum_{i,j=1}^{L} (-1)^{|i-j|} \left\langle \Psi_n \right| S_i^z \left| \Psi_m \right\rangle \left\langle \Psi_m \right| S_j^z \left| \Psi_n \right\rangle e^{-\frac{\beta}{2}(E_n+E_m)} \\
&\qquad\qquad\qquad\qquad\qquad\qquad \times \cosh[(\tau - \frac{\beta}{2})(E_n - E_m)]
\end{aligned}
$$

---

[5]Todo *et al.* [103] used this approach to calculate the gap in the $S = 1, 2, 3$ Heisenberg chains.

# of legs	e_{ladders}	Δ_{ladders}	e_{armchair}	Δ_{armchair}	$e_{\text{zig-zag}}$	$\Delta_{\text{zig-zag}}$	e_{chiral}	Δ_{chiral}	
2	−0.5780(2)	0.51(1)	−0.5780(1)	0.50(1)	−0.5617(1)	0.070(5)			
3	−0.6006(3)	0	-	-	−0.5498(1)	0.11(1)	−0.5529(1)	0.14(1)	(2,1)
4	−0.6187(3)	0.17(1)	−0.5482(1)	0.094(5)	−0.5468(1)	0.04(1)	−0.5472(1)	0.028(2)	(3,1)
5	−0.6278(4)	0	-	-	−0.5456(1)	0.011(1)	−0.5462(1)	0.026(1)	(3,2)
							−0.5460(1)	0.033(2)	(4,1)
6	−0.635(1)	0.05(1)	−0.5456(1)	0.020(1)	−0.5451(1)	0.009(1)	−0.5455(1)	0.017(1)	(4,2)
							−0.5453(1)	0.011(1)	(5,1)
8			−0.5450(1)						
∞	−0.6693(1)	0	−0.545(1)	0					

Table 5.1: We list the energies per site and the spin gaps for spinladders and CNT. We computed the CNT values using the QMC SSE algorithm described in appendix C. The spin ladder results are taken from reference [95] and the value for the honeycomb lattice is taken from reference [102]. The Gap Δ was extracted from a fit to $\chi(T) \propto T^{-1/2} e^{-\Delta/(k_B T)}$ where χ is the uniform magnetic susceptibility (5.7): $\chi = L\beta \langle S^z S^z \rangle$ with $S^z = 1/L \sum_{i=1}^{L} S_i^z$. This formula is valid in the temperature range $k_B T \ll \Delta$ and if one can assume a quadratic dispersion for the lowest lying magnon branch in the excitation spectrum near its minimum (*cf* text). These values were obtained in the limit of very long tubes where the finite size effects are smaller than the statistical error. Typical system sizes L were of order 1000 sites.

We note that the high energy contribution to $C(\tau)$ are suppressed by the term $e^{-\beta(E_n+E_m)/2}$ and in the low temperature limit, $\beta \to \infty$, only the states with the lowest energies contribute. Of course, the term with the lowest $E_n + E_m$ is obtained if $|\Psi_n\rangle$ and $|\Psi_m\rangle$ equal the ground state. But in this case the sum over i and j is just the square of the staggered magnetization $[\sum_i (-1)^i \langle 0|S_i^z|0\rangle]^2$ which is zero because $\langle 0|S_i^z|0\rangle$ is zero at all sites. A non zero value of the local magnetization $\langle 0|S_i^z|0\rangle$ would imply a spontanous breaking of the SU(2) symmetry which is not possible in one dimensional systems. Thus the dominant term comes from the lowest excitations and we can write

$$C(\tau) \propto \cosh[\Delta(\tau - \beta/2)]. \tag{5.9}$$

One could try to make a fit to equation (5.9) to extract the value of the gap Δ but more accurate results can be obtained by using the so–called *second–* and *fourth–moment estimators* [103]. To derive their expressions, we pass to the Fourier space remembering that we are interested in the low–temperature limit $\beta^{-1} \ll \Delta$:

$$
\begin{aligned}
\tilde{C}(q) \quad &\propto \quad \int_0^\beta d\tau \cos(q\tau)\cosh[\Delta(\tau-\beta/2)] \\
&= \quad 2\int_0^{\beta/2} d\tau \cos(q\tau)\cosh[\Delta(\tau-\beta/2)] \\
&\overset{\beta^{-1}\ll\Delta}{\approx} \quad \int_0^{\beta/2} d\tau \cos(q\tau)\, e^{-\Delta(\tau-\beta/2)} \\
&\overset{\beta^{-1}\ll\Delta}{\approx} \quad e^{\beta\Delta/2} \int_0^\infty d\tau \cos(q\tau)\, e^{-\tau\Delta} \\
&= \quad e^{\beta\Delta/2} \frac{\Delta}{\Delta^2 + q^2}
\end{aligned}
\tag{5.10}
$$

This gives us immediately

$$\frac{\tilde{C}(0)}{\tilde{C}(q)} = 1 + \frac{q^2}{\Delta^2} \tag{5.11}$$

and thus it is easy to see that the gap can be expressed *e.g.* by the second–moment estimator

$$\frac{1}{\Delta} = \frac{\beta}{2\pi}\sqrt{\frac{\tilde{C}(0)}{\tilde{C}(2\pi/\beta)} - 1}, \tag{5.12}$$

or the fourth–moment estimator

$$\frac{1}{\Delta} = \frac{\beta}{4\pi}\sqrt{3\frac{\tilde{C}(0)-\tilde{C}(2\pi/\beta)}{\tilde{C}(2\pi/\beta)-\tilde{C}(4\pi/\beta)} - 1}. \tag{5.13}$$

A detailed presentation of the QMC calculations is given at the end of appendix

# of legs	Δ_{armchair}	$\Delta_{\text{zig-zag}}$	Δ_{chiral}	
2	0.504(4)	0.09(1)		
3	-	0.12(1)	0.15(1)	(2,1)
4	0.097(1)	0.044(4)	$\lesssim 0.035(2)$	(3,1)

Table 5.2: The spin gap as determined from the staggered magnetisation in imaginary time. Finite size and finite temperature effects are smaller than the statistical error.
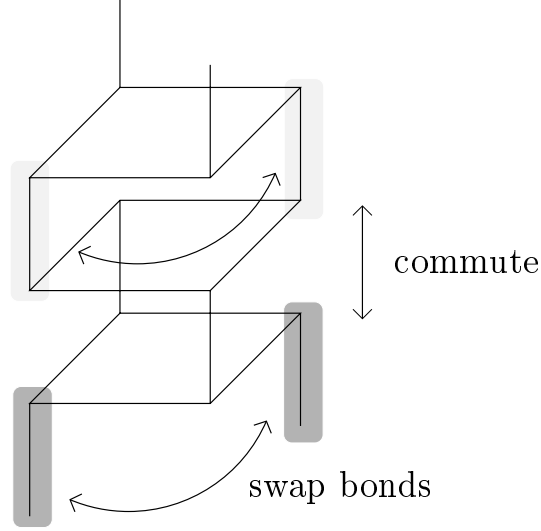
Figure 5.3: The (2,0) CNT can be viewed as coupled squares. In this representation it becomes clear that there are additional commuting local symmetries. The symmetry operations correspond to swap vertical bonds as it is shown.

C. Here, in table 5.2, we show only the extracted values of the gaps for CNT up to four legs. By comparing the tables 5.1 and 5.2 we see that the values are in excellent agreement except the one for the (2,0) CNT. For this zigzag CNT the susceptibility fit gives a slightly smaller value of $0.070\,J$ for the spin gap compared to $0.090\,J$ obained with the second– and fourth–moment estimators. There are several reasons to believe that the (2,0) CNT needs some special care: When we extract the charge gap from the low temperature susceptibility the fit works usually up to temperatures of $k_B T \simeq \Delta$. This can be seen in figure 5.2 for the (2,2) tube. The fit for the (2,0) chirality shows already significant deviations at $k_B T = 0.3J$ although the gap extracted from the fit is $0.070\,J$. We believe that the breakdown of assumption (5.5) is responsible for this abnormal behaviour. There we have assumed a quadratic dispersion for triplet excitations. The (2,0) CNT consists effectively of coupled squares as it is shown in figure 5.3. In this figure we have indicated that there is a macroscopic number of additional local symmetry operations which commute with each other. We believe that this will

	Bond 1∥	Bond 2∥	Bond ⊥	max. difference
(1,1) ladder	-0.351	-0.351	-0.455	0.104
(2,0) squares	-0.412(1)	-0.302(1)	-0.412(1)	0.110
(2,1)	-0.373(1)	-0.339(1)	-0.392(1)	0.053
(3,0)	-0.374(1)	-0.354(1)	-0.374(1)	0.020
(2,2)	-0.360(1)	-0.360(1)	-0.376(1)	0.016
(3,1)	-0.366(1)	-0.359(1)	-0.371(1)	0.012
(4,0)	-0.367(1)	-0.356(1)	-0.369(1)	0.013

Table 5.3: The bond strength $3 \times \left\langle S_i^z S_j^z \right\rangle$ for the three inequivalent bonds of the smallest nanotubes. The last column shows the maximal difference between two such bond strengths. Finite size and finite temperature effects are smaller than the statistical error.

flatten considerable the dispersion relation of the low–lying spin excitations.

5.5   Spin gap phenomenology

We tried to get a simple physical picture for the differences in the spin gap of CNT. Unfortunately it has turned out to be a quite subtle task and we are only able to enumerate some very rudimentary observations. Quite generally one can say that for a given number of legs armchair CNT have the biggest and zigzag CNT the smallest spin gap. However we have observed one exception which is the (3,1) tube which has a smaller gap than the (4,0) zig–zag tube.

We also calculated the bond strengths, *i.e.* $3 \times \left\langle S_i^z S_j^z \right\rangle$, for the three inequivalent bonds in CNT. The values are given in table 5.3. We see that ⊥ bond (*cf* figure 5.1 (b)) is enforced whereas for the zigzag CNT two bonds, namely 1 ∥ and ⊥, are enforced. The relative difference between the bond strengths of a given tube can be reproduced by a simple counting argument. We imagine that the system wants to build up resonances along the shortest path around the circumference. For a given chirality this path consists always of fixed numbers of the three bond types (⊥, 1 ∥, 2 ∥). For example the shortest path in the (2,1) tube goes through three ⊥ bonds, two 1 ∥ bonds and one 2 ∥ bond. That order is also followed by the bond strength. This observation is true for all CNT. Another interesting point is that the value of the gap seems to correlate with the maximal difference of bond strength (*cf* figure 5.4). The only exception is the (2,0) tube whose particularities were already discussed in the previous sections.

Now we will shortly discuss how these results could be applied to real CNT. Although clean CNT have a charge gap (*cf* chapter 3) and are insulating we do not believe that the on–site interaction is as strong that CNT live in the Heisenberg limit where the charge degrees of freedom are neglected completely. However we
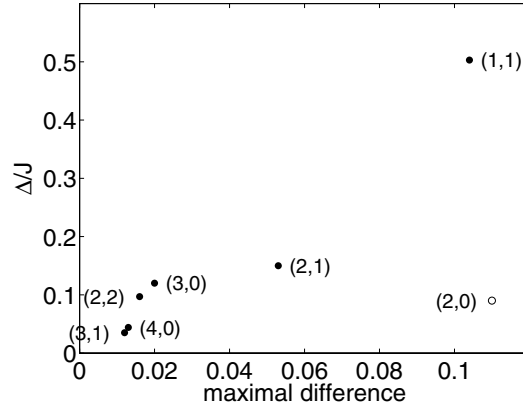
Figure 5.4: We show a scatter plot of the spin gap (table 5.2) versus the maximal difference in bond strength (table 5.3).

think that our results could be pertinent to the question of superconductivity in CNT. Quite recently intrinsic superconductivity has been observed in ropes of SWCNT [15]. The critical temperature is sample dependent varying between 120 and 550 mK. If the tendency to superconductivity depends on chirality this would explain different behaviours between samples. In this chapter we found that the spin gap depends strongly on chirality and also on the tube diameter. Anderson's resonating–valence bond theory (RVB) [104] suggests that a large spin gap favours superconductivity. The RVB theory of superconductivity is discussed and applied to CNT in chapter 6.

Chapter 6

Resonating–valence bond theory on the honeycomb lattice

6.1 Summary

In consideration of the results on the spin gap in the previous chapter we will treat now explicitly the question of superconductivity in CNT. With the help of the t–J model we explore the resonating–valence bond theory for superconductivity on the two–dimensional honeycomb lattice. After a general introduction to RVB theory (section 6.2) we formulate an RVB mean field theory on the honeycomb lattice (subsection 6.3.1). Complementary insight is gained by variational Monte Carlo simulations (subsection 6.3.2). They allow us to study the competition between different phases for the ground–state as a function of doping. At the end of this chapter we discuss the implications of RVB theory for CNT (section 6.4).

Obtained results:

- Determination of the ground–state phase diagram of the t–J model on the honeycomb lattice upon hole doping δ: RVB + antiferromagnetism ($0 < \delta < 1/8$), spin density wave ($1/8 < \delta \lesssim 0.25$), ferromagnetism ($\delta \gtrsim 0.25$)

- We write down a mean field theory for the RVB phase on the honeycomb lattice:

  - The singlet order parameter is of the form $\Delta_{ij} = |\Delta| e^{i\theta_{i-j}}$ with $\theta_\perp = 2/3\,\pi$, $\theta_{1\parallel} = 4/3\,\pi$, $\theta_{2\parallel} = 0$.
  - The spinon excitation spectrum is gapped for $0 < \delta \lesssim 1/8$ and gapless at $\delta = 0$ and $1/8$.

- In the (2,2) and (3,0) CNT superconductivity is enhanced compared to the honeycomb lattice. The RVB order parameters depend on chirality and antiferromagnetism is reduced in all CNT.

- The Gutzwiller projected BCS state reproduces nicely the bond strengths of the Heisenberg model in CNT (calculated in chapter 5).

6.2   The idea of RVB theory

The RVB state describes a "lightly doped spin liquid[1] of spin singlets. Rather than forming a fixed array of singlets (or dimers), strong quantum fluctuations could favor a liquid in which different configurations of singlets resonate." [105] The system needs strong quantum fluctuations to favor such a state, therefore it was initially introduced by Anderson and Fazekas in the seventies [106, 107] to describe the physics of the antiferromagnetic Heisenberg model in low dimensions on the triangular lattice.[2]

Very shortly after the discovery of high T_c superconductors Anderson suggested that this RVB state should be the key player in the underlying microscopic mechanism [104]. All the high T_c materials have in common that they are formed out of weakly coupled two–dimensional layers. Further they are Mott insulators if they are undoped (*i.e.* at commensurate filling). An RVB theory for the insulating state hopes to predict that the preexisting singlet pairs become superconducting pairs when the insulator is doped sufficiently [104]. Therefore the superconductivity would be driven by the strong electron correlations. Anderson's paper generated a huge number of theoretical studies which investigate the RVB theory in the t–J model on the square lattice.[3] The t–J model can be derived from a large U/t expansion of the Hubbard model (3.7). In this limit doubly occupied sites are energetically very unfavorable and one seeks to perform a unitary transformation which eliminates all processes which create doubly occupied sites. These are the hopping terms which change the total number of doubly occupied sites and thus they are those which have to be eliminated. By computing the unitary transformation

$$H_{t-J} = e^{iS} H e^{-iS} = H + i[S, H] - \frac{1}{2}[S, [S, H]] + \dots \qquad (6.1)$$

which does this job up to second order in t/U, one obtains[4]

$$H_{tJ} = T + H_J + H_{\mathrm{h}}^{3-\mathrm{site}} \qquad (6.2)$$

---

[1] A liquid is defined as a state where all correlation functions decay exponentially fast with distance.

[2] Actually the idea goes back to Pauling. It is described in chapter IV entitled "The resonance of molecules among several valence–bond structures" of his book: *The nature of the chemical bond*, Cornell University Press, Ithaca, New York (1945).

[3] *cf* reference [105] for a review.

[4] A detailed derivation of the t–J model can be found in chapter 5 of Fazekas' book [94].

$$T \;=\; -t \sum_{\langle i,j \rangle \sigma} \left(\tilde{c}_{i\sigma}^{\dagger} \tilde{c}_{j\sigma} + \text{h.c.} \right) \tag{6.3}$$

$$H_J \;=\; J \sum_{\langle i,j \rangle} \left(\boldsymbol{S}_i \cdot \boldsymbol{S}_j - \frac{n_i n_j}{4} \right) \tag{6.4}$$

$$H_{\text{h}}^{3-\text{site}} \;=\; -\frac{J}{4} \sum_{\langle i,j,k \rangle \sigma} \left(\tilde{c}_{k\sigma}^{\dagger} n_{j-\sigma} \tilde{c}_{i\sigma} - \tilde{c}_{k\sigma}^{\dagger} \tilde{c}_{j-\sigma}^{\dagger} \tilde{c}_{j\sigma} \tilde{c}_{i-\sigma} + \text{h.c.} \right) . \tag{6.5}$$

$J = 4t^2/U$, $\langle i,j,k \rangle$ denotes a three–site term, with $i \neq k$ being nearest neighbours of j, and the spin operators on site i are given by $\boldsymbol{S}_i = \nicefrac{1}{2} \sum_{\sigma\sigma'} c_{i\sigma}^{\dagger} \boldsymbol{\sigma}_{\sigma\sigma'} c_{i\sigma'}$ where $\boldsymbol{\sigma}$ is a vector containing the Pauli matrices. The projected operators $\tilde{c}_{i\sigma} = c_{i\sigma}(1 - n_{i-\sigma})$ assure that this Hamiltonian acts only in the subspace of no doubly occupied sites. At half–filling the t–J model reduces to the antiferromagnetic Heisenberg model (5.1). The three–site hopping term $H_{\text{h}}^{3-\text{site}}$ is systematically neglected in the literature. One could argue that this term is effectively of order $\delta J/4$, where δ is the number of holes (empty sites) per lattice site. Thus close to half–filling and for small J it should be small compared to the two site hopping (of order δt) and to the exchange term (of order J). In the following we will appeal to common practice and neglect this three–site term.

It was noted by Anderson [104] that it is neither easy to calculate with RVB states nor to represent them. Following Rice and Joynt he proposed to use a representation in terms of Gutzwiller projected BCS states:

$$|\text{RVB}\rangle \;\equiv\; P_N P \, |\text{BCS}\rangle \tag{6.6}$$

$$|\text{BCS}\rangle \;\equiv\; \prod_{\mathbf{k}} \left(u_{\mathbf{k}} + v_{\mathbf{k}} c_{\mathbf{k}\uparrow}^{\dagger} c_{-\mathbf{k}\downarrow}^{\dagger} \right) |0\rangle \tag{6.7}$$

The operator P projects out completely double occupancy and P_N is also a projection operator but which extracts the states with a fixed particle number N. It is convenient to use the t–J model in conjunction with these states since the Gutzwiller projection operators P appear already naturally in the Hamiltonian. Sometimes a real space representation of the RVB states is more suggestive:

$$|\text{RVB}\rangle \;\propto\; P_N P \exp \left(\sum_{\mathbf{k}} \frac{v_{\mathbf{k}}}{u_{\mathbf{k}}} c_{\mathbf{k}\uparrow}^{\dagger} c_{-\mathbf{k}\downarrow}^{\dagger} \right) |0\rangle \tag{6.8}$$

$$=\; P_N P \exp \left(\sum_{i,j} a(i,j) c_{i\uparrow}^{\dagger} c_{j\downarrow}^{\dagger} \right) |0\rangle \tag{6.9}$$

$$\propto\; P \left(\sum_{i,j} a(i,j) c_{i\uparrow}^{\dagger} c_{j\downarrow}^{\dagger} \right)^{N/2} |0\rangle \tag{6.10}$$

where $a(i,j) = \sum_{\mathbf{k}} \frac{v_{\mathbf{k}}}{u_{\mathbf{k}}} e^{i\mathbf{k}(\mathbf{R_i}-\mathbf{R_j})}$. Therefore this state can be viewed as a linear superposition of configurations consisting of singlet pairs and empty sites as one

would expect for an RVB state. The singlet bonds correspond to preformed pairs and the empty sites to holes which were introduced upon doping.

Within the framework of the t–J model and Gutzwiller projected states there are roughly speaking two complementary approaches available: Formulating a mean field theory or doing a variational Monte Carlo (VMC) calculation. The latter approach can be used to examine the ground–state energy by plugging in various trial states. It has the advantage that the Gutzwiller projection can be evaluated exactly. Thus VMC can show if the RVB state really gives the lowest energy ground–state, but unfortunately it gives only information about the ground–state and limits in the system size of the numerical calculation can be a problem. Alternatively a mean field theory, although it needs to introduce a rough approximation to perform the Gutzwiller projection, can in principle give a more complete theory where we can study quasiparticle–excitations and thermodynamics. In this chapter these two approaches are applied to investigate the idea of RVB on the honeycomb lattice and in the special case of CNT.

6.3   Results for the 2D honeycomb lattice

6.3.1   Mean field theory

The most systematic approach up to date to formulate an RVB mean field theory is based on the slave boson representation [108] which factorizes the electron operators into charge and spin parts $c_{i\sigma}^{\dagger} = f_{i\sigma}^{\dagger} b_i$ called holons and spinons. The charged boson operator b_i destroys an empty site (hole) and $f_{i\sigma}^{\dagger}$ is a fermionic creation operator which carries the spin of the physical electron. The constraint of no doubly occupied site can now be implemented by requiring $\sum_{\sigma} f_{i\sigma}^{\dagger} f_{i\sigma} + b_i^{\dagger} b_i = 1$ at each site. In the slave boson formalism the t–J model becomes [109]

$$
\begin{aligned}
H &= -t \sum_{\langle i,j \rangle \sigma} \left(f_{i\sigma}^{\dagger} f_{j\sigma} b_j^{\dagger} b_i + \text{h.c.} \right) - \mu_0 \sum_i n_i \\
&\quad + J \sum_{\langle i,j \rangle} \left(\boldsymbol{S}_i \cdot \boldsymbol{S}_j - \frac{n_i n_j}{4} \right) + \sum_i \lambda_i \left(\sum_{\sigma} f_{i\sigma}^{\dagger} f_{i\sigma} + b_i^{\dagger} b_i - 1 \right)
\end{aligned} \tag{6.11}
$$

where $\boldsymbol{S}_i = \frac{1}{2} \sum_{\sigma\sigma'} f_{i\sigma}^{\dagger} \boldsymbol{\sigma}_{\sigma\sigma'} f_{i\sigma'}$ and $n_i = \sum_{\sigma} f_{i\sigma}^{\dagger} f_{j\sigma}$. This Hamiltonian is gauge invariant by simultaneous local transformation of the holon and spinon $f_{i\sigma} \to f_{i\sigma} e^{i\phi_i}$ and $b_{i\sigma} \to b_{i\sigma} e^{i\phi_i}$. Now one can make a mean field approximation by a decoupling in a series of expectation values $\chi_{ij} = \sum_{\sigma} \left\langle f_{i\sigma}^{\dagger} f_{j\sigma} \right\rangle$, $\Delta_{ij} = \sum_{\sigma} \left\langle f_{i\uparrow} f_{j\downarrow} - f_{i\downarrow} f_{j\uparrow} \right\rangle$ and $B_i = \left\langle b_i^{\dagger} \right\rangle$. Further one sets all the Lagrange multipliers λ_i equal to a single value which replaces the local constraints by one global constraint. Following references [105, 110] we present the basic results for the square lattice in figure
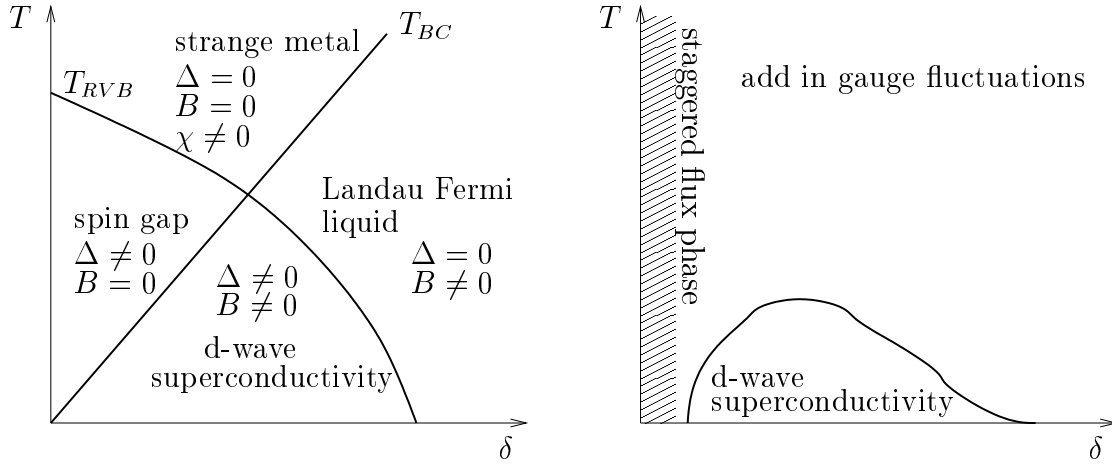
Figure 6.1: The mean field phase diagram on the square lattice without (left hand side) and including (right hand side) phase fluctuations. The region $\Delta \neq 0$ and $B = 0$ is called "spin gap phase" since the mean field theory gives an anisotropic gap in the single particle excitation spectrum with maxima at $\mathbf{k} = (\pm\pi, 0)$. However this gap is annihilated in some regions of the Brillouin zone. These diagrams can be found in references [105, 110].

6.1 (left hand side). To have a superconducting state in the slave boson representation it is not sufficient that the fermions form Cooper pairs but also the bosons need to be in a coherent state of a Bose condensate. On the square lattice one finds that the particle–particle expectation values have d–wave symmetry, *i.e.* $\Delta_x = -\Delta_y$. The mean field phase diagram suggests some phase transitions, however χ_{ij}, Δ_{ij}, and B_i cannot be true order parameters since they are not gauge invariant. In fact Ubbens and Lee [110] have shown that gauge fluctuations destroy completely these phases and only a d–wave superconducting dome is left over (*cf* the right hand side of figure 6.1). Moreover these fluctuations diminish also the tendency for superconductivity and seem to destroy it completely near half–filling where they believe that it is unstable towards more complicated phases such as a staggered flux phase. However it is not clear up to what temperature these results are valid.

In this section we will use a simplified version of the previously mentioned RVB theory. Despite of its simplicity this theory should nevertheless predict the correct symmetry of the superconducting order parameter and be able to make some predictions about the spinon excitations. In fact this simplified RVB theory predicts d–wave superconductivity on the square lattice [109] and was also applied to the Shastry–Sutherland [111] and triangular lattice [112]. It is based on a decoupling of the superexchange term in singlet operators. Given the

identity

$$\boldsymbol{S}_i \cdot \boldsymbol{S}_j - \frac{n_i n_j}{4} = -\frac{1}{2} B^\dagger(i,j) B(i,j) \tag{6.12}$$

$$\text{where} \qquad B(i,j) \equiv f_{i\uparrow} f_{j\downarrow} - f_{i\downarrow} f_{j\uparrow}, \tag{6.13}$$

a decoupling in $\Delta_{ij} \equiv \langle B(i,j) \rangle$ seems to be the natural choice. To handle the bosons one assumes that all the λ_i are equal to a single value λ which plays the role of the boson chemical potential. We replace the boson operators by a static value which is chosen such that $\left\langle b_i^\dagger b_j \right\rangle = \delta$ for all i, j [109–112]. Thus in this approximation the effect of the slave bosons (or equivalently of the Gutzwiller projection) is included in a very simplified way which effectively multiplies the kinetic energy of the spinons by the hole concentration δ and redefines their chemical potential $\mu \to \mu_0 + \lambda$:

$$
\begin{aligned}
H_{tJ}^{\mathrm{MF}} \;=\; & -t\delta \sum_{\langle i,j \rangle \sigma} \left(f_{i\sigma}^\dagger f_{j\sigma} + \text{h.c.} \right) - \mu \sum_i n_i \\
& -\frac{J}{2} \sum_{\langle i,j \rangle} \left(\left\langle B^\dagger(i,j) \right\rangle B(i,j) + B^\dagger(i,j) \left\langle B(i,j) \right\rangle - \left\langle B^\dagger(i,j) \right\rangle \left\langle B(i,j) \right\rangle \right)
\end{aligned}
\tag{6.14}
$$

In addition we make a simple ansatz for the RVB order parameter Δ_{ij}: In the honeycomb lattice each site has three nearest neighbour bonds $\perp$, 1 $\|$, 2 $\|$ (cf figure 2.1). We assume that the amplitude is uniform, $i.e.$ $|\Delta_{ij}| = \Delta$ but each bond is allowed his own phase $\theta_\perp$, $\theta_{1\|}$, $\theta_{2\|}$. Of course, only relative phases matter and we choose to set $\theta_{2\|} = 0$. We show the analytic diagonalization of the mean field Hamiltonian in appendix D. The mean field solution is obtained by minimizing the resulting free energy density

$$\phi = -\mu + \frac{3}{4} J \Delta^2 - \frac{1}{L} \sum_{\mathbf{k}j} \left(\varepsilon_j(\mathbf{k}) + \frac{2}{\beta} \ln\left[1 + \exp(-\beta \varepsilon_j(\mathbf{k})) \right] \right) \tag{6.15}$$

with respect to Δ, $\theta_\perp$, $\theta_{1\|}$ and under the conservation of particle number constraint

$$\frac{\partial \phi}{\partial \mu} = -\frac{N}{L} \qquad \Rightarrow \qquad \delta = -\frac{1}{L} \sum_{\mathbf{k}j} \frac{\partial \varepsilon_j(\mathbf{k})}{\partial \mu} \tanh\left(\frac{\beta \varepsilon_j(\mathbf{k})}{2} \right). \tag{6.16}$$

$\varepsilon_{j=\pm}(\mathbf{k})$ are the dispersions of the single particle spinon excitations above the ground–state. They are given by

$$\varepsilon_\pm(\mathbf{k}) = \sqrt{ \mu^2 + J^2 |B(\mathbf{k})|^2 + \delta^2 |\xi(\mathbf{k})|^2 \pm 2\delta \sqrt{ J^2 |B(\mathbf{k})|^2 \left(\mathrm{Im}\, \xi(\mathbf{k}) \right)^2 + \mu^2 |\xi(\mathbf{k})|^2 } }$$

$$\tag{6.17}$$
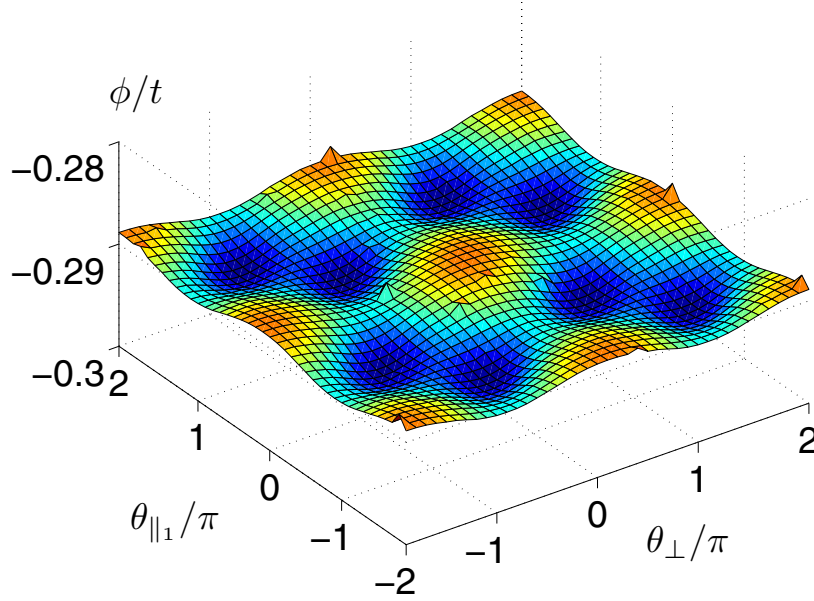
Figure 6.2: The mean field energy density (ϕ at zero temperature) as a function of the phases $\theta_\perp$, $\theta_{1\parallel}$ in the singlet order parameter associated with two different bonds in the honeycomb unit cell.

$$\text{where} \qquad \xi(\mathbf{k}) = t\left(e^{i(\alpha_2 - \alpha_1)} + e^{i\alpha_2} + 1\right), \qquad (6.18)$$

$$\text{and} \qquad B(\mathbf{k}) = \Delta/2\left(e^{-i\theta_{1\parallel}}\cos(\alpha_2 - \alpha_1) + e^{-i\theta_\perp}\cos\alpha_2 + 1\right). \qquad (6.19)$$

Again we have used the projections on the reciprocal basis vectors: $\mathbf{k} = \alpha_1/2\pi\,\mathbf{b_1} + \alpha_2/2\pi\,\mathbf{b_2}$.

Let us discuss the solutions of this mean field theory. The first information we would like to get out is the symmetry of the mean field order parameter, *i.e.* what values of $\theta_\perp$ and $\theta_{1\parallel}$ give the lowest ground–state energy. We find that the phases $\theta_\perp = 2/3\,\pi$, $\theta_{1\parallel} = 4/3\,\pi$ give the lowest energy. We checked this for $J/t = 0.2$, 0.4, 0.8 and all possible hole dopings. Of course one can interchange $\theta_\perp$ and $\theta_{1\parallel}$ and also add or subtract 2π to each of these phases and still having the same energy. All this is shown in figure 6.2. These values were also found in the triangular lattice [112] which has hexagonal symmetry as well. In figure 6.3 we plot the RVB mean field expectation value Δ as a function of hole doping. We want to emphasize that Δ is not the superconducting order parameter which is actually given in our approximation by $\left\langle c_{i\uparrow}^\dagger c_{j\downarrow}^\dagger \right\rangle = \left\langle b_i f_{i\uparrow}^\dagger b_j f_{j\downarrow}^\dagger \right\rangle \simeq \left\langle b_i b_j \right\rangle \left\langle f_{i\uparrow}^\dagger f_{j\downarrow}^\dagger \right\rangle$. At zero temperature we have $\left\langle c_{i\uparrow}^\dagger c_{j\downarrow}^\dagger \right\rangle \simeq \delta\Delta$. As it is shown in figure 6.3, Δ decreases with doping and we obtain the famous superconducting dome (*cf* figure 6.1) as a generic feature of the RVB mean field theory.
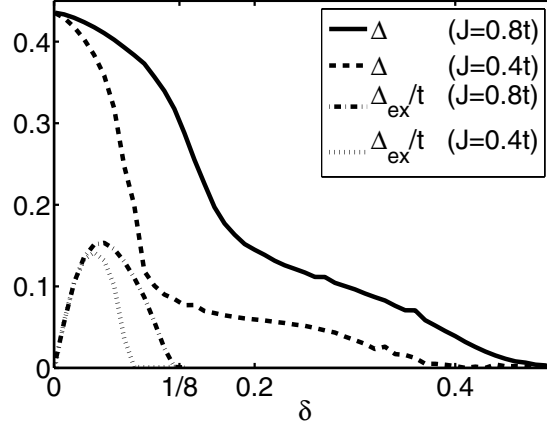
Figure 6.3: The mean field order parameter Δ and the spinon excitation gap $\Delta_{\mathrm{ex}} = 2\min_{\mathbf{k}}\varepsilon_-(\mathbf{k})$ as a function of hole doping.

We turn now to the excitation spectra. Two of them are shown in figure 6.4 with the corresponding density of states for $J = 0.8t$ and hole doping of $\delta = 0.1$ and 0.2 respectively. They are exemplary for the two possible regimes which one can obtain. At low doping the spinon spectrum is gapped whereas at dopings above the van Hove singularity at $\delta = 1/8$ (*cf* figure 2.2) the spectrum has gapless single–quasiparticle excitations on the ΓK line. This point is further illustrated in figure 6.3 where the spinon excitations gap $\Delta_{\mathrm{ex}} = 2\min_{\mathbf{k}}\varepsilon_-(\mathbf{k})$ is plotted as a function of doping for $J/t = 0.8$ and 0.4. Δ_{ex} can survive maximally up to the doping corresponding to the van Hove singularity. For small values ($J \lesssim 0.4\,t$) the rapidly decreasing singlet order parameter Δ kills it already before that point. A remarkable fact is that this gap is zero at half–filling and rises up (this rise seems to be independent of the J value) to a maximum value of approximatively $0.15\,t$ and decreases to zero again. For comparison we note that the gap is always zero in the square lattice, in the triangular lattice it is finite at any doping except at half–filling. Whereas the Shastry–Sutherland lattice has a spinon gap at half–filling which decreases to zero with doping. For all these lattices one recovers the correct behaviour at half–filling, as it is known the square, the triangular, and the honeycomb lattices have gapless spin excitations but a spin gap shows up in the Shastry–Sutherland model.

The van Hove singularity at $\delta = 1/8$ does not only kill the spin gap, but on quite general grounds one expects that a Kanamori ferromagnetic state[5] is favored over the RVB state for $\delta \geq 1/8$. This and other instabilities of the ground–state are studied in the next subsection by variational Monte Carlo simulations.

---

[5]The Kanamori criterion consists of correcting the Stoner criterion $U\rho(\varepsilon_F) = 1$ for large U/t, *cf* reference [94] p. 423.
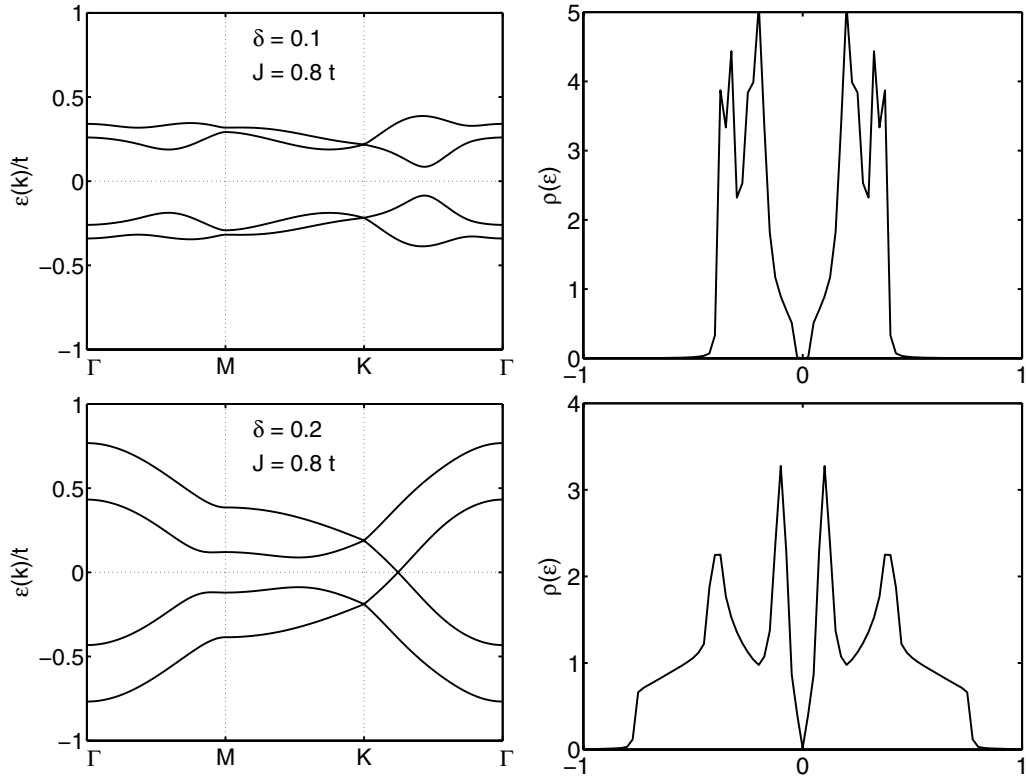
Figure 6.4: The two plots on the left show the spinon dispersion $\varepsilon_\pm$ (given by equation (6.17)) along the high symmetry lines for two different values of hole doping $\delta = 0.1$, 0.2 and $J = 0.8\,t$. The right hand side shows the corresponding density of states.

6.3.2   Variational Monte Carlo calculation

The variational Monte Carlo (VMC) method allows to evaluate numerically the Gutzwiller projection P of some product state $|\Psi_0\rangle$ which is in general defined as the ground–state of a mean field Hamiltonian.[6] The expectation value of an operator A in $|\Psi\rangle \equiv PP_{S^z}P_N |\Psi_0\rangle$ [7] can be brought quite easily into a form which is susceptible of a MC evaluation:

$$\langle A \rangle = \frac{\langle \Psi| A |\Psi\rangle}{\langle \Psi|\Psi\rangle} \tag{6.20}$$

$$= \sum_\alpha \underbrace{\left(\sum_\beta \frac{\langle \alpha| A |\beta\rangle \langle \beta|\Psi\rangle}{\langle \alpha|\Psi\rangle} \right)}_{f(\alpha)} \underbrace{\frac{|\langle \alpha|\Psi\rangle|^2}{\langle \Psi|\Psi\rangle}}_{\rho(\alpha)} \tag{6.21}$$

$|\alpha\rangle$ (respectively $|\beta\rangle$) belongs to a basis set which allows to calculate easily $\langle \alpha|\Psi\rangle$ and $A |\alpha\rangle$. In practice often one uses

$$|\alpha\rangle = c_{i_1\uparrow}^\dagger \ldots c_{i_{N/2}\uparrow}^\dagger c_{i_1\downarrow}^\dagger \ldots c_{i_{N/2}\downarrow}^\dagger |0\rangle . \tag{6.22}$$

$\rho(\alpha)$ satisfies the requirements of a probability density and therefore $\langle A \rangle$ can be evaluated by a random walk through configuration space using the Metropolis algorithm (see *e.g.* [115]), and one has

$$\langle A \rangle = \frac{1}{N_{\mathrm{MC}}} \sum_{i=1}^{N_{\mathrm{MC}}} f(\alpha_i) \tag{6.23}$$

where N_{MC} is the total number of MC measurements.

The VMC method is now used to examine which trial states have the lowest energy in the t–J model on the honeycomb lattice as a function of hole doping. The variational wave functions are built out of the ground–states of the following mean field like Hamiltonian:

$$H_{tJ}^{\mathrm{MF}} = -t \sum_{\langle i,j \rangle,\sigma} \left(c_{i\sigma}^\dagger c_{j\sigma} + \mathrm{h.c.} \right) + \sum_{\langle i,j \rangle} (\Delta_{i,j} B(i,j) + \mathrm{h.c.})$$

$$+ \sum_i \boldsymbol{h}_i \cdot \boldsymbol{S}_i - \mu \sum_{i,\sigma} n_{i,\sigma} \quad (6.24)$$

This Hamiltonian is slightly more general than the previously studied Hamiltonian (6.14) as it contains also a decoupling in the particle hole channel. We have considered the following class of variational wave functions to study the honeycomb lattice:

---

[6]For a nice introduction to VMC one can consult references [113] and [114].

[7]For technical reason and because total electron number and total S^z are exact quantum numbers of the t–J Hamiltonian one projects also on states with fixed particle number and on the sector with $S^z = 0$.
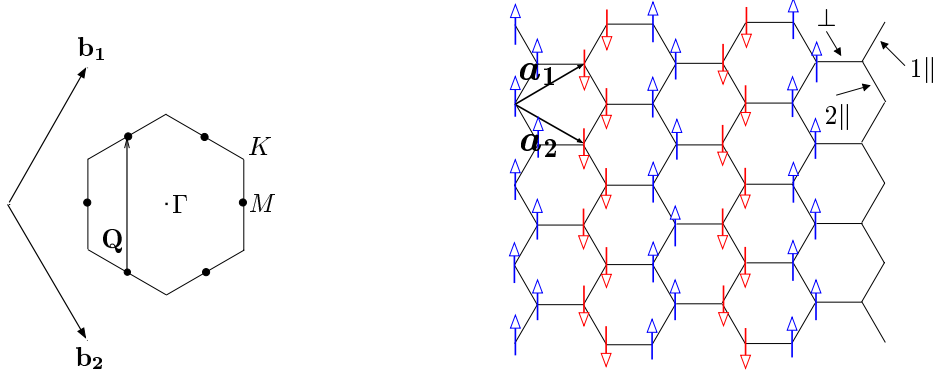
Figure 6.5: Illustration of the **Q**–SDW phase: On the left hand side we show the first Brillouin zone and the vector **Q** which connects two of the M points. It is at the M points where the van Hove singularity occurs. On the right hand side we draw a real space representation of this instability. It corresponds to ferromagnetic stripes. The stripes itself align antiferromagnetically.

lattice	Fermi sea	Best VMC	exact
triangular	$-0.3547(2)$	$-0.533(1)$ [116]	$-0.5458(1)$ [117]
square	$-0.4270(2)$	$-0.664(1)$ [118]	$-0.6693(1)$ [119]
honeycomb	$-0.5275(2)$	$-0.5430(2)$	$-0.545(1)$ [102]

Table 6.1: Comparison of the ground–state energy estimation for the Heisenberg model on different lattices. The first column is just the expectation value of the Gutzwiller projected Fermi sea, the second column shows the best VMC result, and the last column is obtained by QMC or exact diagonalization. All energies are given in units of J.

- Our reference state is the Fermi sea: $\Delta_{ij} \equiv 0$ and $\boldsymbol{h}_i \equiv \boldsymbol{0}$

- A staggered antiferromagnetic order (AF): $\Delta_{ij} \equiv 0$ and $\boldsymbol{h}_i \equiv (-1)^i \boldsymbol{h}$

- A superconducting phase (RVB): Δ_{ij} as studied in the subsection 6.3.1 and $\boldsymbol{h}_i \equiv \boldsymbol{0}$.

- A ferromagnetic state (F): $\Delta_{ij} \equiv 0$ and $\boldsymbol{h}_i \equiv \boldsymbol{h}$

- A commensurable spin density wave (SDW) of wave vector $\boldsymbol{Q} = \frac{1}{2}(\boldsymbol{b_1} - \boldsymbol{b_2}) = 2\pi/a\,(0,1)$ (see figure 6.5): $\Delta_{ij} \equiv 0$ and $\boldsymbol{h}_i \equiv \boldsymbol{h}\cos(\boldsymbol{Q} \cdot \boldsymbol{R}_i)$

Before discussing the VMC phase diagram we note that in the Heisenberg model on the honeycomb lattice the Gutzwiller projected Fermi sea gives already a ground–state energy which is very close to the exact value. As it is shown in table 6.1, the difference is about 0.017 J. This value is very small compared to the ones in the square and triangular lattices. Even smaller are therefore the energy
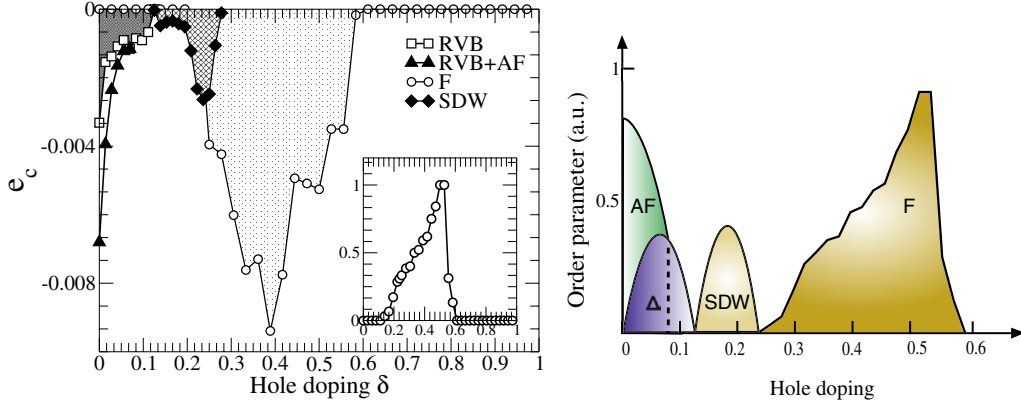
Figure 6.6: On the left hand side we plot the condensation energies (in units of t), *i.e.* the energy gain with respect to the Gutzwiller projected Fermi sea. The inset shows the ferromagnetic polarization divided by the saturation value. The right hand side is a sketchy representation of the resulting zero temperature phase diagram as a function of doping. All VMC results presented in this chapter were obtained from a 144 site cluster at $J = 0.4\ t$. Results on a 72 site lattice with the same geometry showed no significant difference.

gains which can be obtained from the various trial states. They are plotted on the left hand side of figure 6.6. Close to half–filling a mixed phase of an RVB and an antiferromagnetic state is stabilized. The RVB state is killed at the van Hove singularity and the antiferromagnetic correlations disappear slightly earlier. We have already discussed previously that at a doping of $1/8$ the Fermi surface touches the M points. These are the points where the van Hove singularity occurs and the Fermi surface is partially nested with wave vector $\boldsymbol{Q} = 2\pi/a\,(0, 1)$ (*cf* figure 6.5). Close to $\delta = 1/8$ a SDW phase with this wave vector is stabilized. But at dopings of $\delta \gtrsim 0.25$ the ferromagnetic state wins.

The VMC simulations confirm the results of the RVB mean field theory. The minimization of the RVB state gives the same symmetry of Δ_{ij} in both methods: Δ_{ij} has the same magnitude on the three links and the phases are $\theta_\perp = 2/3\,\pi$, $\theta_{1\|} = 4/3\,\pi$, $\theta_{2\|} = 0$. Once one has found the best RVB state, VMC makes it possible to evaluate the singlet superconducting order parameters $S_{\alpha,\beta}$ [116]

$$S^2_{\alpha,\beta} = \frac{1}{4L} \lim_{r \to \infty} \sum_i \frac{\left\langle \Psi \left| B^\dagger(i, i+\alpha) B(i+r, i+r+\beta) \right| \Psi \right\rangle}{\langle \Psi | \Psi \rangle} \tag{6.25}$$

where α and β are chosen from the three links $\perp$, 1 $\|$, 2 $\|$. Actually we found that

$$S^2_{\alpha,\beta} = \left| S^2_{\alpha,\beta} \right| e^{i(\theta_\alpha + \theta_\beta)} \tag{6.26}$$

and that $\left| S^2_{\alpha,\beta} \right|$ is independent of the choice of α and β. In figure 6.7 we plot
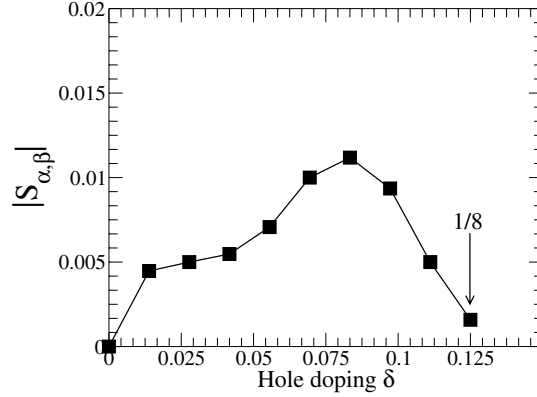
Figure 6.7: We show the singlet superconducting order parameter (6.25) in the RVB + AF wave function.

$|S_{\alpha,\beta}| \equiv \sqrt{\left|S_{\alpha,\beta}^2\right|}$ as a function of hole doping and we obtain a superconducting dome which is characteristic of the RVB theory. The maximal amplitude of $S_{\alpha,\beta}$ is rather small, *e.g.* it is about four times smaller than in the square lattice.

6.4 CNT

In the previous section we have studied the ground–state phase diagram of the t–J model on the honeycomb lattice upon hole doping. Between half–filling and the van Hove singularity at $\delta = 1/8$ we found that a mixture between an RVB and an antiferromagnetic state gives the best variational ground–state energy. In this section we study also this region for CNT. This investigation is motivated by the experimentally observed intrinsic superconductivity in ropes of SWCNT.[8] SWCNT are one–dimensional systems and therefore no continuous symmetry can be broken. This is however necessary for superconductivity (broken $U(1)$) and also for antiferromagnetism and the spin density wave (broken $SU(2)$). Although these phases cannot form the true ground–state, the fluctuations around them can still be important for determining its physics. For example one could imagine that such fluctuations stabilize a superconducting state in ropes of SWCNT. In consideration of this argument we believe that it is pertinent to study the tendency of superconductivity in SWCNT.

After the discussion of section 3.7 on the microscopic parameters for CNT in the Hubbard model, we expect quite a large exchange coupling of $J \simeq t$. However we decided to set it again to $J = 0.4t$ which gives us the possibility to make a comparison with the previous results. We believe that the conclusions will not depend on the exact value, but a larger value of J will enforce the tendency to

---

[8] *cf* reference [15] and section 5.5.

lattice	e VMC	e QMC	M_{AF}	$\Delta_{2\|,2\|}$	$\theta_{2\|}$	$\theta_{1\|}$	$\theta_\perp$
2D	$-0.5430(1)$	$-0.545(1)$	$0.330(2)$	$0.0016(4)$	0	$2\pi/3$	$4\pi/3$
(3,0)	$-0.5458(1)$	$-0.5498(1)$	$0.290(2)$	$0.0032(4)$	0	$\approx 3\pi/2$	$\approx \pi$
(2,2)	$-0.5435(1)$	$-0.5482(1)$	$0.290(2)$	$0.0032(4)$	0	$\approx 5\pi/4$	$\approx \pi$
(4,0)	$-0.5425(1)$	$-0.5468(1)$	$0.320(2)$	$0.0008(4)$	0	$\approx 5\pi/4$	$\approx \pi/4$
(2,1)	$-0.5475(1)$	$-0.5529(1)$	$0.240(2)$	$0.0016(4)$	0	$\approx 5\pi/4$	$\approx \pi/4$

Table 6.2: Heisenberg energy and staggered magnetization extrapolated to the thermo-dynamic limit for the 2D lattice and some CNT in the Heisenberg limit (half–filling). Also the maximal values (as a function of doping) of the superconductivity order parameters are depicted. The values were obtained for $J = 0.4t$.
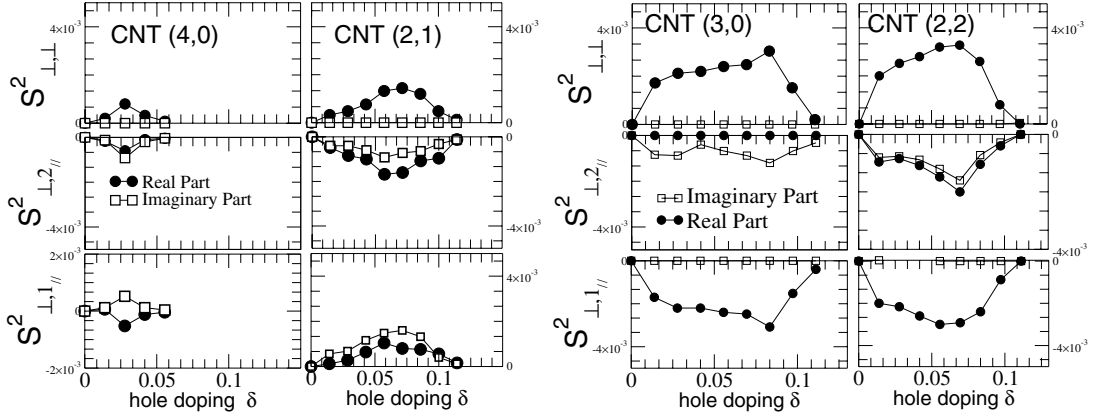
Figure 6.8: We show the superconducting order parameters for CNT at $J = 0.4t$. Their definition is given in equation 6.25.

superconductivity.

The results of the VMC calculation of the RVB + AF phase in CNT are listed in table 6.2, which contains also a comparison with the 2D honeycomb results. We observe that the antiferromagnetic correlations are slightly reduced. We note also that the phases of the singlet order parameters depend on chirality and more importantly also the amplitudes. For the (2,2) and (3,0) CNT super-conductivity is enhanced considerably compared to the 2D honeycomb lattice, whereas it is reduced substantially for the (4,0) chirality. This seems to suggest a relation between superconductivity and the Heisenberg spin gap (*cf* table 5.2). Unfortunately the (2,1) tube does not fit into this picture, it has a larger spin gap than (2,2) and (3,0) but the tendency to superconductivity is weaker. The superconducting order parameters are further illustrated in figure 6.8 where the real and the imaginary parts of $S^2_{\alpha,\beta}$ are plotted for all investigated CNT. We see that superconductivity in the (4,0) zigzag CNT is not only reduced in magnitude,

		Fermi sea	RVB	RVB + AF	exact
(2,2)	Bond 1∥	-0.368	-0.349	-0.356	-0.360
	Bond 2∥	-0.360	-0.350	-0.360	-0.360
	Bond ⊥	-0.316	-0.379	-0.372	-0.376
(3,0)	Bond 1∥	-0.362	-0.377	-0.373	-0.374
	Bond 2∥	-0.330	-0.336	-0.348	-0.354
	Bond ⊥	-0.360	-0.374	-0.369	-0.374
(4,0)	Bond 1∥	-0.376	-0.386	-0.370	-0.369
	Bond 2∥	-0.310	-0.313	-0.351	-0.356
	Bond ⊥	-0.370	-0.372	-0.364	-0.367
(2,1)	Bond 1∥	-0.355	-0.353	-0.359	-0.373
	Bond 2∥	-0.264	-0.308	-0.329	-0.339
	Bond ⊥	-0.434	-0.430	-0.410	-0.392
honeycomb				-0.360	

Table 6.3: Comparison of the bond strengths $3 \times \left\langle S_i^z S_j^z \right\rangle$ in the Heisenberg model as evaluated by VMC and SSE QMC (*cf* chapter 5).

but it already disappears at very low doping $\delta \simeq 0.05$.

At half–filling we can compare the VMC results to the exact SSE QMC calculations of chapter 5. From table 6.2 we can read off that the energy densities follow the exact values quite closely with the correct relative order. As it is shown in table 6.3 it reproduces also quite nicely the bond strengths for all chiralities we looked at. The necessary ingredients to obtain these results are the exact Gutzwiller projection and the BCS type mean field state. In contrast, the Gutzwiller projected Fermi sea is *not* able to reproduce these results as it gives wrong values for the (2,2) armchair CNT. Because of this agreement with the exact QMC simulations we are confident that our RVB trial state gives a good description of the physics near half–filling.

Chapter 7

Conclusion

In this thesis we have studied CNT with an emphasis on the interplay between electronic correlations and chirality which has been considered in a variety of situations:

- Hubbard model $\longrightarrow$ charge gap (chapter 3)

- $\left.\begin{array}{l} \text{tight--binding model} \\ \text{Anderson model} \end{array}\right\} \longrightarrow$ persistent current, charge stiffness (chapter 4)

- Heisenberg model $\longrightarrow$ spin gap (chapter 5)

- t–J model $\longrightarrow$ RVB superconducting order parameter (chapter 6)

We are not going to repeat the details of our results here as they are outlined in the summaries at the beginning of each chapter. But we would like to place our results within a broader context.

More generally speaking we challenged the two most common theoretical approaches to CNT which consists of either completely neglecting the electronic correlations in a band structure calculation or including it perturbatively in a weak coupling theory in the continuous limit of the honeycomb lattice. We have seen in chapter 3 that neither of these two approaches can be used when it comes to the computation of the charge gap. In one dimensional systems strong correlations are expected and a single particle charge gap should be present at half–filling. It was argued by Balents and Fisher [30] and subsequently used by many others that in CNT correlations were strongly reduced as the electrons can delocalize around the circumference. Consequently CNT with a large enough diameter could be treated as a weakly interacting system. We showed that this is however not the case as one cannot neglect the effects of the higher one dimensional bands. This is an example of the complicated interplay between the detailed lattice structure and strong correlations. Other examples are the spin gap (chapter 5) and the RVB theory of superconductivity (chapter 6). In chapter 4 we could exhibit some

effects of chirality on the persistent currents when a magnetic field is applied. But the role of correlations is still an open question in this context.

To summarize, we are convinced that CNT have to be considered as materials where electronic correlations are strong. At the moment not many experimental results are available to test our predictions. But there are are ongoing experimental efforts to produce SWCNT in a better and better controlled way, and low temperature experimental investigations on SWCNT start to make observations in the meV regime. Thus we are confident that soon the conclusions of this thesis can be tested experimentally.

Appendix A

The Hartree–Fock approximation for the repulsive Hubbard model

A.1   Summary

In this appendix we expose in detail the H–F results used in chapter 3. We derive the self-consistency equation for the antiferromagnetic order parameter in an unfrustrated bipartite lattice at half–filling. We also calculate the spin susceptibility within this approximation.

A.2   The method

The H–F theory was originally introduced as a variational method to get approximate ground states for atoms, which is a many–body problem due to the Coulomb interaction. In the variational procedure one restricts the Hilbert space (where the Hamiltonian $\hat{H}$ acts) to a tractable subspace $\mathcal{F} = \{\Psi_j\}$ and one looks for a minimum of the following functional

$$\frac{\langle \Psi_j | \hat{H} | \Psi_j \rangle}{\langle \Psi_j | \Psi_j \rangle} \tag{A.1}$$

which is an upper bound to the true ground state energy E_0, i.e.

$$E_0 \leq \inf \frac{\langle \Psi_j | \hat{H} | \Psi_j \rangle}{\langle \Psi_j | \Psi_j \rangle}. \tag{A.2}$$

The H–F states $\mathcal{F}_{HF}$ are the determinants of one–particle orbitals $\phi_j(x_i, \sigma_i)$,

$$\Psi_{HF} = \frac{1}{\sqrt{N!}} \det \left[\phi_j(x_i, \sigma_i) \right]_{1 \leq i,j \leq N} \tag{A.3}$$

where x_i are the space and σ_i the spin variables, and N is the number of particles. It is clear that these states conserve the particle number, but they are not necessarily eigenstates of other conserved quantities such as the total spin or the total angular momentum. In the following we consider the repulsive Hubbard model, in this case the H–F states are sufficient to describe the mean–field[1] physics of this hamiltionian. In the attractive case however they are not general enough since one has to allow bound states, where the particle number is not conserved, a famous example is the BCS theory of superconductivity. A more general H–F theory can be formulated in terms of the one–particle density matrix which overcomes this restriction and allows to treat the attractive and the repulsive Hubbard model on equal footing [120].

We will specialize the discussion to the repulsive Hubbard model on a lattice with nearest neighbour hopping, as described in chapter 3. The H–F theory gives the following effective single particle Hamiltonian [31]:

$$H_{HF} = \sum_{\langle i,j \rangle \sigma} \left(t_{ij} c_{i\sigma}^\dagger c_{j\sigma} + \text{h.c.} \right) + \hat{V}_{HF} \tag{A.4}$$

The Hubbard interaction term is split into a direct (Hartree) term and an exchange (Fock) term

$$\hat{V}_{HF} = \hat{V}^d + \hat{V}^e \tag{A.5}$$

$$\hat{V}^d = U \sum_i \left[n_{i\uparrow} \langle n_{i\downarrow} \rangle + \langle n_{i\uparrow} \rangle n_{i\downarrow} - \langle n_{i\uparrow} \rangle \langle n_{i\downarrow} \rangle \right] \tag{A.6}$$

$$\hat{V}^e = -U \sum_i \left[S_i^+ \langle S_i^- \rangle + S_i^- \langle S_i^+ \rangle - \langle S_i^+ \rangle \langle S_i^- \rangle \right] \tag{A.7}$$

where $S_i^+ = c_{i\uparrow}^\dagger c_{i\downarrow}$ and $S_i^+ = c_{i\downarrow}^\dagger c_{i\uparrow} = \left(S_i^- \right)^\dagger$. Although the H–F Hamiltonian has the form of a single electron problem, it is still a tough problem to solve in general, since it depends on the expectation values $\langle n_{i\sigma} \rangle$, $\langle S_i^+ \rangle$ and $\langle S_i^- \rangle$ which have to be determined self-consistently. Thus in principle, one has to determine the minimal free energy in the space of all self-consistent solutions. For the Hamiltionian (A.4) there are two rigorous results which are exact within H–F theory [31, 120]:

1. For $U/t = \infty$ the ground state is always fully ferromagnetically polarized if we are below half–filling.

2. If we are at half–filling and on a bipartite lattice with non–frustrated hopping, the H–F theory gives always anti–ferromagnetic ordering for any value of the interaction strength U/t. In particular the expectation values are given by

$$\langle n_{i\sigma} \rangle = 1/2 \left(1 + m(-1)^i \lambda_{\uparrow\sigma} \right), \tag{A.8}$$

where $\lambda_{\sigma\sigma} = 1$, $\lambda_{\sigma-\sigma} = -1$ and $m = |\langle n_{i\uparrow} \rangle - \langle n_{i\downarrow} \rangle|$.

---

[1] The mean–field Hamiltonian is obtained by the most general decoupling of the interaction term(s) compatible with Wick's theorem.

The second statement implies that the spin in the z direction is conserved, and thus one can chose the axis of quantization in such a way that the exchange term (A.7) vanishes. In the following we derive the self–consistent equation for the case where this applies.

A.3 The self–consistency equation on a bipartite lattice at half–filling

We consider now in more detail the case of a bipartite lattice at half–filling and where the hopping is unfrustrated. We have seen in the previous section that in this special case the exchange term (A.7) vanishes and the expectation values are given by (A.8). We replace these expection values into the H–F Hamiltonian (A.4) and we obtain

$$H_{HF} = \sum_{\langle i,j \rangle \sigma} \left(t_{ij} c_{i\sigma}^{\dagger} c_{j\sigma} + \text{h.c.} \right) + \frac{Um}{2} \sum_{i\sigma} (-1)^i \lambda_{\uparrow\sigma} \, n_{i\sigma} + \frac{U}{4} \left(1 + m^2 \right) L \, \hat{\mathbb{I}}. \quad (A.9)$$

We have denoted by L the total number of lattice sites. As we are on a bipartite lattice we can separate our lattice into two sublattices A and B where all the nearest neighbours of every site of lattice A belong to the sublattice B and vice versa. Then to diagonalize the Hamiltonian (A.9) we treat the two sublattices independently by defining new fermionic operators for each sublattice:

$$a_{\mathbf{k}}^{\dagger} \equiv \frac{1}{\sqrt{L/2}} \sum_{\mathbf{R} \in A} e^{-i\mathbf{k} \cdot (\mathbf{R} + \mathbf{v})} \, c_{\mathbf{R}}^{\dagger} \quad (A.10)$$

$$b_{\mathbf{k}}^{\dagger} \equiv \frac{1}{\sqrt{L/2}} \sum_{\mathbf{R} \in B} e^{-i\mathbf{k} \cdot (\mathbf{R} + \mathbf{u})} \, c_{\mathbf{R}}^{\dagger} \quad (A.11)$$

It is straightforward to obtain the expressions for the hermitian conjugates $a_{\mathbf{k}}$ and $b_{\mathbf{k}}$. $\mathbf{k}$ belongs to the first Brioullin zone. The unit cell contains two atoms, one
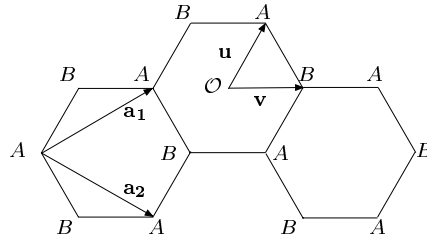
Figure A.1: The two sublattices A and B are shown. The basis vectors are as before $\mathbf{a_1} = a/2 \left(\sqrt{3}, 1 \right)$ and $\mathbf{a_2} = a/2 \left(\sqrt{3}, -1 \right)$. The vectors connecting the sublattices are $\mathbf{u} = a/\sqrt{3} \left(1/2, \sqrt{3}/2 \right)$ and $\mathbf{v} = a/\sqrt{3} \left(1, 0 \right)$. $\mathcal{O}$ is the origin from which the positions $\mathbf{R}$ are measured.

of sublattice A and one of sublattice B, thus the number of different k–vectors is $L/2$. With the help of these new operators we go to the reciprocal space:

$$
\begin{aligned}
H_{HF} \;=\; & \sum_{\mathbf{k}\sigma} \left[\left(\sum_i t_{ij} e^{i\mathbf{k}(\mathbf{R_i}+\mathbf{v}-\mathbf{R_j}-\mathbf{u})} \right) a^\dagger_{\mathbf{k}\sigma} b_{\mathbf{k}\sigma} + \text{h.c} \right] \\
& + \frac{Um}{2} \sum_{\mathbf{k}\sigma} \lambda_{\uparrow\sigma} \left(a^\dagger_{\mathbf{k}\sigma} a_{\mathbf{k}\sigma} - b^\dagger_{\mathbf{k}\sigma} b_{\mathbf{k}\sigma} \right) + \frac{U}{4} \left(1+m^2\right) L\,\hat{\mathbb{I}}. \quad \text{(A.12)}
\end{aligned}
$$

We define the new operators

$$
\overline{a}^\dagger_{\mathbf{k}\sigma} = \frac{\sum_i t_{ij} e^{i\mathbf{k}(\mathbf{R_i}+\mathbf{v}-\mathbf{R_j}-\mathbf{u})}}{\epsilon(\mathbf{k})} \; a^\dagger_{\mathbf{k}\sigma} \tag{A.13}
$$

$$
\text{where} \quad \epsilon(\mathbf{k}) = \left| \sum_i t_{ij} e^{i\mathbf{k}(\mathbf{R_i}+\mathbf{v}-\mathbf{R_j}-\mathbf{u})} \right|. \tag{A.14}
$$

Clearly the sums over i are independent of $\mathbf{R_j}$ because of the translation invariance of t_{ij}. Let us express this hamiltonian with the help of the operators $\overline{a}^\dagger_{\mathbf{k}\sigma}$:

$$
H_{HF} = \sum_{\mathbf{k}\sigma} \epsilon(\mathbf{k}) \left(\overline{a}^\dagger_{\mathbf{k}\sigma} b_{\mathbf{k}\sigma} + b^\dagger_{\mathbf{k}\sigma} \overline{a}_{\mathbf{k}\sigma} \right) + \frac{Um}{2} \sum_{\mathbf{k}\sigma} \lambda_{\uparrow\sigma} \left(\overline{a}^\dagger_{\mathbf{k}\sigma} \overline{a}_{\mathbf{k}\sigma} - b^\dagger_{\mathbf{k}\sigma} b_{\mathbf{k}\sigma} \right) + \frac{U}{4} \left(1+m^2\right) L\,\hat{\mathbb{I}}
$$
$$\tag{A.15}$$

This Hamiltonian can be diagonalized by a Bogoliubov transformation of the following form:

$$
\begin{aligned}
\overline{a}^\dagger_{\mathbf{k}\sigma} &= -\sin\phi_{\mathbf{k}\sigma} \alpha^\dagger_{\mathbf{k}\sigma} + \cos\phi_{\mathbf{k}\sigma} \beta^\dagger_{\mathbf{k}\sigma} \tag{A.16} \\
b^\dagger_{\mathbf{k}\sigma} &= \cos\phi_{\mathbf{k}\sigma} \alpha^\dagger_{\mathbf{k}\sigma} + \sin\phi_{\mathbf{k}\sigma} \beta^\dagger_{\mathbf{k}\sigma} \tag{A.17}
\end{aligned}
$$

To cancel the non–diagonal terms the $\phi_{\mathbf{k}\sigma}$ have to satisfy

$$
\tan\left(2\phi_{\mathbf{k}\sigma}\right) = \lambda_{\uparrow\sigma} \frac{2\epsilon(\mathbf{k})}{Um}, \tag{A.18}
$$

and we obtain the H–F Hamiltonian in it's diagonal form

$$
\begin{aligned}
H_{HF} \;=\; & \sum_{\mathbf{k}} \left[\sqrt{\frac{U^2 m^2}{4} + \epsilon^2(\mathbf{k})} \left(\beta^\dagger_{\mathbf{k}\uparrow} \beta_{\mathbf{k}\uparrow} + \alpha^\dagger_{\mathbf{k}\downarrow} \alpha_{\mathbf{k}\downarrow} \right) \right. \\
& \left. - \sqrt{\frac{U^2 m^2}{4} + \epsilon^2(\mathbf{k})} \left(\beta^\dagger_{\mathbf{k}\downarrow} \beta_{\mathbf{k}\downarrow} + \alpha^\dagger_{\mathbf{k}\uparrow} \alpha_{\mathbf{k}\uparrow} \right) \right] \\
& + \frac{U}{4} \left(1+m^2\right) L\,\hat{\mathbb{I}}. \tag{A.19}
\end{aligned}
$$

This Hamiltonian depends on one self–consistent parameter, the sublattice magnetisation m. Using equation (A.18) we can write down an implicit equation for m. By definition:

$$m \;=\; \frac{1}{L}\left(\sum_{i\in A} |\langle n_{i\uparrow}\rangle - \langle n_{i\downarrow}\rangle| - \sum_{i\in B} |\langle n_{i\uparrow}\rangle - \langle n_{i\downarrow}\rangle| \right) \tag{A.20}$$

$$\;=\; \frac{1}{L}\sum_{\mathbf{k}} \left(\langle a^{\dagger}_{\mathbf{k}\downarrow} a_{\mathbf{k}\downarrow}\rangle - \langle a^{\dagger}_{\mathbf{k}\uparrow} a_{\mathbf{k}\uparrow}\rangle - \langle b^{\dagger}_{\mathbf{k}\downarrow} b_{\mathbf{k}\downarrow}\rangle + \langle b^{\dagger}_{\mathbf{k}\uparrow} b_{\mathbf{k}\uparrow}\rangle \right) \tag{A.21}$$

For the ground state we have

$$\langle \beta^{\dagger}_{\mathbf{k}\downarrow} \beta_{\mathbf{k}\downarrow}\rangle = \langle \alpha^{\dagger}_{\mathbf{k}\uparrow} \alpha_{\mathbf{k}\uparrow}\rangle = 1\,, \tag{A.22}$$

whereas all other expectation values are zero. Then we can evaluate the sublattice magnetisation when the system is in the ground state:

$$m \;=\; \frac{1}{L}\sum_{\mathbf{k}} \left(\cos^2\phi_{\mathbf{k}\downarrow} - \sin^2\phi_{\mathbf{k}\uparrow} + \cos^2\phi_{\mathbf{k}\uparrow} + \sin^2\phi_{\mathbf{k}\downarrow} \right) \tag{A.23}$$

$$\;=\; \frac{1}{L}\sum_{\mathbf{k}} \left(\cos(2\phi_{\mathbf{k}\uparrow}) + \cos(2\phi_{\mathbf{k}\downarrow}) \right) \tag{A.24}$$

$$\;=\; \frac{1}{L}\sum_{\mathbf{k}\sigma} \frac{1}{\sqrt{1 + \tan^2(2\phi_{\mathbf{k}\sigma})}} \tag{A.25}$$

$$\overset{(A.18)}{=}\; \frac{2}{L}\sum_{\mathbf{k}} \frac{Um}{\sqrt{U^2 m^2 + 4\epsilon^2(\mathbf{k})}} \tag{A.26}$$

This is the central equation of the presented H–F theory.

A.4 The RPA susceptibility

Now we want to determine at which value of U the antiferromagnetic instability (A.8) sets in. We expect that at the onset of antiferromagnetism the static staggered spin susceptibility will diverge. To calculate this susceptibility in H–F theory we have to couple the electrons to an external staggered field by an additional Zeeman term

$$H_B = g\mu_B \sum_i (-1)^i B S_i^z, \tag{A.27}$$

$g \simeq 2$ is the gyromagnetic ratio, $\mu_B = \frac{e\hbar}{2m} \simeq 5.8$ eV/T the Bohr magneton and B the amplitude of the applied staggered field. The Hamiltonian (A.9) becomes (neglecting the constant terms):

$$H_{HF} = \sum_{\langle i,j\rangle\sigma} \left(t_{ij} c^{\dagger}_{i\sigma} c_{j\sigma} + \text{h.c.} \right) + \frac{Um + g\mu_B B}{2} \sum_{i\sigma} (-1)^i \lambda_{\uparrow\sigma}\, n_{i\sigma} \tag{A.28}$$

We see that the results from the previous section are still valid when Um is replaced by $Um + g\mu_B B$. Then the self–consistency equation (A.26) reads

$$m = \frac{2}{L} \sum_{\mathbf{k}} \frac{Um + g\mu_B B}{\sqrt{(Um + g\mu_B B)^2 + 4\epsilon^2(\mathbf{k})}} \overset{\text{first order}}{\approx} (Um + g\mu_B B) \underbrace{\frac{2}{L} \sum_{\mathbf{k}} \frac{1}{2|\epsilon(\mathbf{k})|}}_{\chi_0},$$

$$\text{(A.29)}$$

and we get the magnetisation in first order in the applied field

$$m = g\mu_B B \frac{\chi_0}{1 - U\chi_0}. \tag{A.30}$$

The staggered static susceptibility is defined at zero temperature for small fields by the following partial derivative of the ground state energy E_0:

$$\chi = \frac{1}{L} \left. \frac{\partial^2 E_0}{\partial B^2} \right|_{B=0} \tag{A.31}$$

As we do not know the exact ground state energy of the original Hamiltonian (3.7) we evaluate it in the H–F ground state:

$$\chi_{RPA} = \frac{1}{L} \frac{\partial^2}{\partial B^2} \left(\langle HF| H |HF \rangle + \frac{g\mu_B B}{2} \sum_i \underbrace{\langle HF| (-1)^i S_i^z |HF \rangle}_{m} \right) \Bigg|_{B=0}$$

$$\Rightarrow \quad \chi_{RPA} \overset{(A.30)}{=} (g\mu_B)^2 \frac{\chi_0}{1 - U\chi_0} \tag{A.32}$$

We see that the susceptibility diverges if

$$U_{cr}^{HF} \chi_0 = 1. \tag{A.33}$$

This equation determines the onset of the antiferromagnetic instability in the H–F approximation.

Appendix B

Weakly interacting fermions in one dimension

B.1   Summary

This appendix has two goals. First it should give an introduction to the very special physics of one–dimensional systems. This is an extreme view of a CNT but it is expected that many signatures of this physics should actually be observed in CNT [1] and on a practical level, it has the advantage that all the technical tools of one–dimensional physics are then available. A huge amount of work is published on CNT from this point of view mainly to study correlation effects. Some of them are cited in this thesis. Secondly in chapter two I make use of a renormalization group equation for the one–dimensional Hubbard model to compute the charge gap for a CNT. The derivation of this equation is given below.

B.2   The g–ology model

This section follows closely the review article by Sólyom [121]. We want to define an effective low–energy model for electrons of spin one half on a *one*–dimensional chain of length ℓ and lattice spacing a interacting via the Coulomb interaction. We start from a tight–binding description of the problem ignoring the Coulomb interaction:

$$H_0 = -2t \sum_{k\sigma} \cos(ak)\, c_{k\sigma}^\dagger c_{k\sigma} \tag{B.1}$$

In the following we make the assumption that the interaction can be regarded as "weak", *i.e.* we consider only electrons which lie near the Fermi surface. Under this assumption we are allowed to linearize the dispersion relation around the Fermi points $\pm k_F$. We will impose a cutoff on the bandwidth by restricting the

---

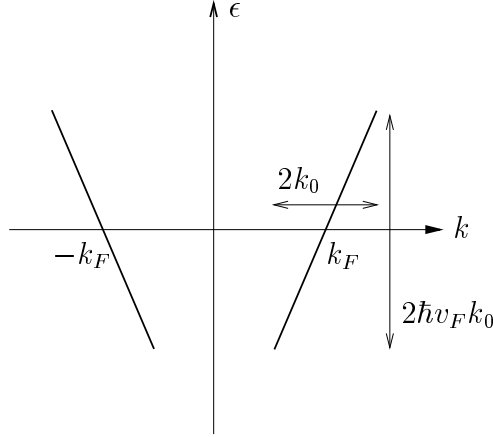[1]See *e.g.* section 10.3 of [73] and the references given there.

Figure B.1: The two branches of the linearized tight–binding band with a finite band-width cutoff $E_0 = 2\hbar v_F k_0$.

summation on the wave vector. Then the dispersion is split into two branches, the left moving electrons with negative momenta and the right moving ones with positive momenta as it is shown in figure B.1. The lattice spacing a can serve as a natural cutoff for the wave vector $k_0 \approx 1/a$ which leads to a bandwith cutoff $E_0 = 2v_F k_0$. Using this cutoff the wave vectors for the left branch take values in the interval $[-k_F - k_0, -k_F + k_0]$ and for the right branch in the interval $[k_F - k_0, k_F + k_0]$. Noting the operators of the left moving electrons by $b_{k\sigma}$, and respectively by $a_{k\sigma}$ the right moving ones, the tight–binding hamiltonian becomes

$$H_0 = \sum_{k\sigma} \underbrace{v_F(k - k_F)}_{\epsilon_a(k)}\, a^\dagger_{k\sigma} a_{k\sigma} + \sum_{k\sigma} \underbrace{v_F(-k - k_F)}_{\epsilon_b(k)}\, b^\dagger_{k\sigma} b_{k\sigma}. \qquad \text{(B.2)}$$

Now we want to analyze which interaction processes dominate the low–energy physics of one–dimensional electrons within the model with bandwith cutoff. Electrons interact via the Coulomb interaction which can be written as [33]

$$H_{int} = \frac{1}{2\ell} \sum_{qkk'\sigma\sigma'} V(q)\, c^\dagger_{k+q\sigma} c^\dagger_{k'-q\sigma'} c_{k'\sigma'} c_{k\sigma}. \qquad \text{(B.3)}$$

As it is shown in figure B.2, all scattering processes which act close to the Fermi surface can be classified into four groups. The first ones are the backscattering processes. They exchange electrons from one branch to another, thus the momen-tum transfer involved is $2k_F$. The associated coupling constant is denoted by g_1. The coupling constants g_2 and g_4 correspond to forward scattering, the momen-tum exchange is small ($q \approx 0$). The umklapp process g_3 scatters two fermions, initially on the same branch, to the opposite one. This process does not conserve momentum. In fact the difference in momentum between the incoming and the
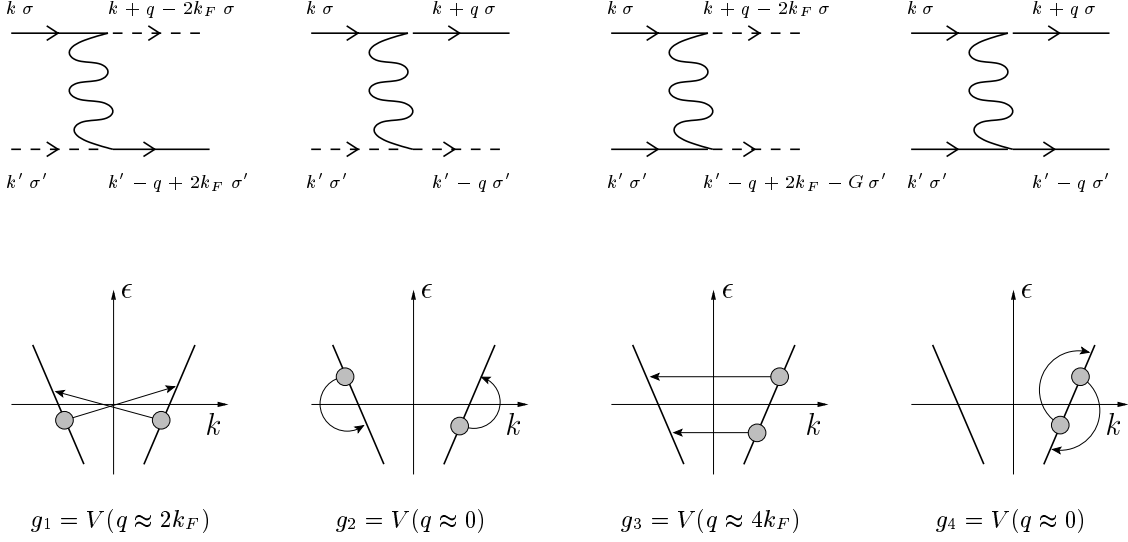
$$g_1 = V(q \approx 2k_F) \qquad g_2 = V(q \approx 0) \qquad g_3 = V(q \approx 4k_F) \qquad g_4 = V(q \approx 0)$$

Figure B.2: We show the four different types of low energy processes. A full (dashed) line stands for a rightmoving (leftmoving) electron. We note by g_i the associated coupling constants.

outgoing particles is $4k_F$. Such a process gives a non–zero contribution if $4k_F$ equals a vector of the reciprocal lattice. In one dimension, it is only the case for half–filling.

Further we note a process with coupling constant $g_{i\parallel}$ if the spins of the scattering electrons are equal and by $g_{i\perp}$ if they are opposite. Then the Coulomb interaction can be written as follows

$$
\begin{aligned}
H_{int} \;=\;& \frac{1}{\ell} \sum_{qkk'\sigma\sigma'} \left(g_{1\parallel}\delta_{\sigma\sigma'} + g_{1\perp}\delta_{\sigma,-\sigma'} \right) a_{k\sigma}^\dagger b_{k'\sigma'}^\dagger a_{k'+2k_F+q\sigma'} b_{k-2k_F-q\sigma} \\
&+ \frac{1}{\ell} \sum_{qkk'\sigma\sigma'} \left(g_{2\parallel}\delta_{\sigma\sigma'} + g_{2\perp}\delta_{\sigma,-\sigma'} \right) a_{k\sigma}^\dagger b_{k'\sigma'}^\dagger b_{k'+q\sigma'} a_{k-q\sigma} \\
&+ \frac{1}{2\ell} \sum_{qkk'\sigma\sigma'} \left(g_{3\parallel}\delta_{\sigma\sigma'} + g_{3\perp}\delta_{\sigma,-\sigma'} \right) \left(a_{k\sigma}^\dagger a_{k'\sigma'}^\dagger b_{k'-2k_F+q\sigma'} b_{k+2k_F-q-G\sigma} \right. \\
&\qquad\qquad\qquad\qquad \left. + b_{k\sigma}^\dagger b_{k'\sigma'}^\dagger a_{k'+2k_F+q\sigma'} a_{k-2k_F-q+G\sigma} \right) \\
&+ \frac{1}{2\ell} \sum_{qkk'\sigma\sigma'} \left(g_{4\parallel}\delta_{\sigma\sigma'} + g_{4\perp}\delta_{\sigma,-\sigma'} \right) \left(a_{k\sigma}^\dagger a_{k'\sigma'}^\dagger a_{k'+q\sigma'} a_{k-q\sigma} \right. \\
&\qquad\qquad\qquad\qquad \left. + b_{k\sigma}^\dagger b_{k'\sigma'}^\dagger b_{k'+q\sigma'} b_{k-q\sigma} \right) .
\end{aligned}
\tag{B.4}
$$

This is the most general two–body interaction for weakly interacting fermions in one dimension. However, in the following we assume that our hamiltonian respects spin rotation invariance and consequently we can write $g_i \equiv g_{i\perp} \equiv g_{i\parallel}$.
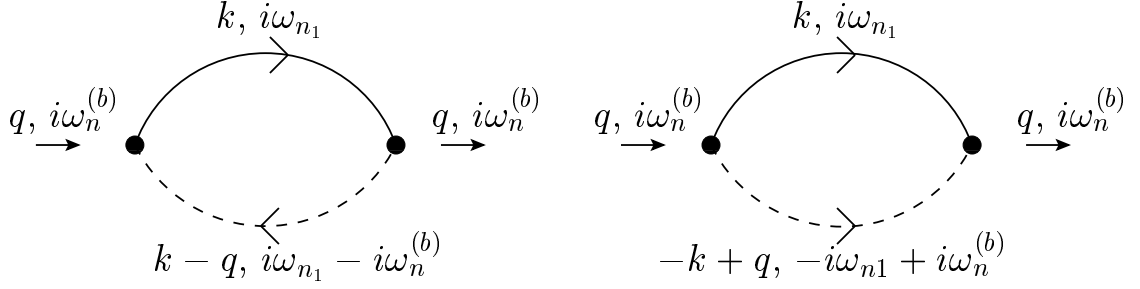
Figure B.3: The diagrams for the bare Peierls (left) and Cooper (right) susceptibilities. As before, a solid line corresponds to a rightmoving electron and a dashed line to a leftmoving one.

B.3   Perturbation Theory

The main line of argument of this section is based on the book by Giamarchi [73]. Usually, systems with weak interactions are treated by perturbation theory. However in *one* dimension its correct computation is a difficult problem. The difficulty is due to the fact that in *one* dimension it leads to logarithmic singularities simultaneously in the Peierls (particle–hole) and in the Cooper (particle–particle) channel. The elementary diagrams of these two channels are shown in figure B.3. The Peierls channel describes the density fluctuations around a charge density wave with wavevector $2k_F$ [2]

$$O_{\text{Peierls}}\left(q = 2k_F,\, i\omega_n^{(b)}\right) = \sum_{k,\,n_1,\,\sigma} \tilde{b}_{k-2k_F,\sigma}^\dagger(i\omega_{n_1} - i\omega_n^{(b)})\tilde{a}_{k\sigma}(i\omega_{n_1}). \tag{B.9}$$

---

[2]Here we work in the Fourier–Matsubara space, *e.g*:

$$\tilde{b}_k^\dagger(i\omega_n) = \int_0^\beta \mathrm{d}\tau\, e^{i\omega_n\tau}\,\hat{b}_k^\dagger(\tau) \tag{B.5}$$

$$\hat{b}_k^\dagger(\tau) = e^{\tau H_0} b_k^\dagger e^{-\tau H_0} = e^{\tau\epsilon_b(k)b_k^\dagger b_k} b_k^\dagger e^{-\tau\epsilon_b(k)b_k^\dagger b_k} = e^{-\tau\epsilon_b(k)} b_k^\dagger \tag{B.6}$$

The fermionic Matsubara frequencies are defined by

$$e^{i\omega_n\beta} = -1 \quad \text{or} \quad \omega_n = \frac{(2n+1)\pi}{\beta} \tag{B.7}$$

wich reflect the anticommutation relations of fermions. In equation B.9 and the following expressions one has to keep in mind that ω_{n_1} and the sums $\omega_{n_1} \pm \omega_n^{(b)}$ have to be fermionic frequencies. This is only possible if $\omega_n^{(b)}$ is a bosonic frequency:

$$\omega_n^{(b)} = \frac{2n\pi}{\beta} \tag{B.8}$$

For more details one can consult for example reference [33], pages 110*ff*.

The Cooper channel stands for the pair fluctuations around

$$O_{\text{Cooper}}\left(q = 0,\, i\omega_n^{(b)}\right) = \sum_{k,\, n_1,\, \sigma = \pm 1/2} \sigma \, \tilde{b}_{-k,-\sigma}(-i\omega_{n_1} + i\omega_n^{(b)}) \, \tilde{a}_{k,\sigma}(i\omega_{n_1}). \quad \text{(B.10)}$$

The corresponding susceptibilities are given by

$$\chi_\mu(i\omega_n^{(b)}) = -\frac{1}{\beta\ell} \left\langle O_\mu(i\omega_n^{(b)}) O_\mu^\dagger(i\omega_n^{(b)}) \right\rangle. \quad \text{(B.11)}$$

The non–interacting contributions can be found by evaluating the diagrams in figure B.3 [3]. For example the contribution to the Peierls channel from this diagram is

$$\chi_P(i\omega_n^{(b)}) = \frac{2}{\beta\ell} \sum_{k,n_1} G_b^{(0)}(k - 2k_F, i\omega_{n_1} - i\omega_n^{(b)}) G_a^{(0)}(k, i\omega_{n_1}) \quad \text{(B.12)}$$

$$= \frac{2}{\beta\ell} \sum_{k,n_1} \frac{1}{i\omega_{n_1} - i\omega_n^{(b)} - \epsilon_b(k - 2k_F)} \frac{1}{i\omega_{n_1} - \epsilon_a(k)} \quad \text{(B.13)}$$

There is a straightforward procedure to evaluate quite generally sums over Matsubara frequencies (fermionic or bosonic). Restrict ourselves to the fermionic case where we want to calculate a sum of the form

$$\frac{1}{\beta} \sum_n \phi(i\omega_n) \quad \text{(B.14)}$$

where $\phi(z)$ is a meromorphic function with simple poles only in $z = z_l$ and residual r_l. Further we assume that the poles do not coincide with the Matsubara frequencies. We note that the Fermi–Dirac distribution, analytically continued to the complex plane,

$$f_{\text{FD}}(z) \equiv \frac{1}{1 + e^{\beta z}} \quad \text{(B.15)}$$

has its poles at the fermionic Matsubara frequencies, and the same residual $-1/\beta$ for all poles. We apply the residual theorem to the integral

$$\lim_{R \to \infty} \int_{C_R} \frac{\mathrm{d}z}{2\pi i} \, f_{\text{FD}}(z) \phi(z) \quad \text{(B.16)}$$

where the contour C_R is chosen to be a circle of radius R around the origin which gives

$$\frac{1}{\beta} \sum_n \phi(i\omega_n) = \sum_l r_l f_{FD}(z_l). \quad \text{(B.17)}$$

---

[3] *cf e.g.* [122], p. 300*ff.*

This formula can directly be applied to our sum:

$$
\chi_P\left(i\omega_n^{(b)}\right) = \frac{2}{\ell}\sum_k \left\{ \frac{f_{\mathrm{FD}}(\epsilon_a(k))}{\epsilon_a(k) - i\omega_n^{(b)} - \epsilon_b(k - 2k_F)} + \frac{f_{\mathrm{FD}}(\epsilon_b(k - 2k_F) + i\omega_n^{(b)})}{\epsilon_b(k - 2k_F) + i\omega_n^{(b)} - \epsilon_a(k)} \right\}
$$

$$
= \frac{2}{\ell}\sum_k \frac{f_{\mathrm{FD}}(\epsilon_a(k)) - f_{\mathrm{FD}}(\epsilon_b(k - 2k_F))}{-i\omega_n^{(b)} + \epsilon_a(k) - \epsilon_b(k - 2k_F)} \tag{B.18}
$$

The measurable quantity is however the retarded susceptibility which is obtained by analytic continuation $i\omega_n^{(b)} \to \hbar\omega + i\delta$:[4]

$$
\overline{\chi}_P^{(\mathrm{ret})}(\omega) = \frac{2}{\ell}\sum_k \frac{f_{\mathrm{FD}}(\epsilon_a(k)) - f_{\mathrm{FD}}(\epsilon_b(k - 2k_F))}{\hbar\omega + \epsilon_a(k) - \epsilon_b(k - 2k_F) + i\delta} \tag{B.19}
$$

In a completely analogous way one obtains the non–interacting retarded susceptibility for the Cooper channel

$$
\overline{\chi}_C^{(\mathrm{ret})}(\omega) = \frac{2}{\ell}\sum_k \frac{f_{\mathrm{FD}}(\epsilon_a(k)) - f_{\mathrm{FD}}(-\epsilon_b(-k))}{\hbar\omega - \epsilon_a(k) - \epsilon_b(-k) + i\delta}. \tag{B.20}
$$

We observe that the one dimensional dispersions $\epsilon_a(k)$ and $\epsilon_b(k)$ defined in equation (B.2) have the two following properties which are uniquely due to time reversal symmetry

$$
\epsilon_b(-k) = \epsilon_a(k), \tag{B.21}
$$

$$
\epsilon_b(k - 2k_F) = -\epsilon_a(k). \tag{B.22}
$$

These relations have drastic consequences on the behavior of the susceptibilities[5]:

$$
\mathrm{Re}\,\overline{\chi}_P^{(\mathrm{ret})}(\omega) = -\frac{1}{\ell}\sum_k \frac{\tanh(\beta\epsilon_a(k)/2)}{\epsilon_a(k)} \tag{B.23}
$$

$$
\stackrel{\ell\to\infty}{=} -\int_{-E_0/2}^{E_0/2} \mathrm{d}\epsilon\,\rho(\epsilon)\,\frac{\tanh(\beta\epsilon/2)}{2\epsilon} \tag{B.24}
$$

We remind that E_0 is the energy cutoff introduced in section B.2 and $\rho(\epsilon)$ is the density of states per unit volume where the factor 2 comes from the spin degeneracy. If the density of states does not vanish at the Fermi level ($\epsilon = 0$) we have a logarithmic singularity at wave vector $2k_F$, regularized by the temperature:

$$
\mathrm{Re}\,\overline{\chi}_P^{(\mathrm{ret})}(2k_F) \approx -\rho(0)\left(-\int_{-E_0/2}^{-k_BT/2} \mathrm{d}\epsilon\,\frac{1}{2\epsilon} + \int_{k_BT/2}^{E_0/2} \mathrm{d}\epsilon\,\frac{1}{2\epsilon}\right) \tag{B.25}
$$

$$
= -\rho(0)\ln(E_0\beta) \tag{B.26}
$$

---

[4] *cf e.g.* [33], p. 121.

[5] Here we show the real part only. However the imaginary part can always be obtained using the Kramers–Kronig relations, *cf e.g.* [33] p. 360.
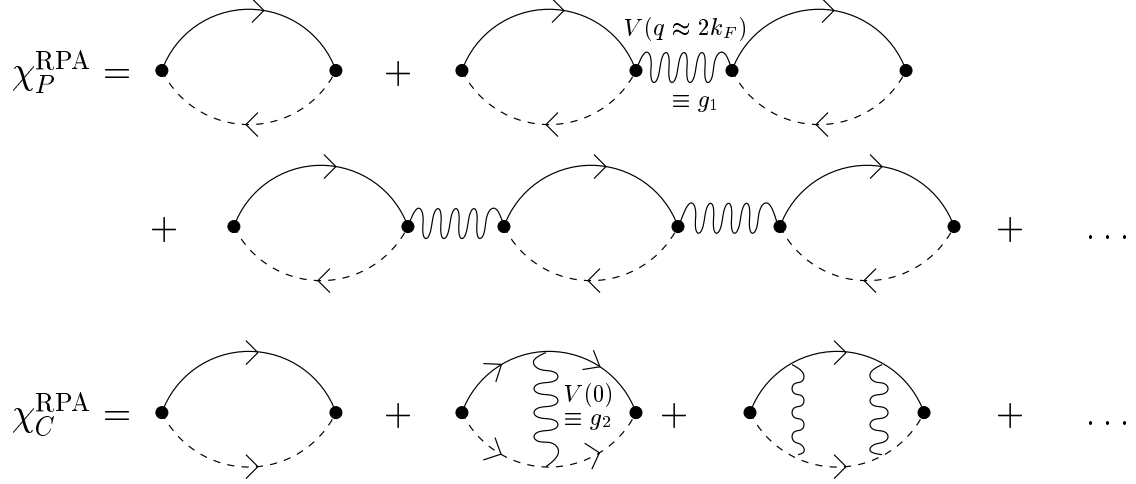
Figure B.4: In the RPA approximation we sum up the bubble diagrams for the Peierls channel and the ladder diagrams for the Cooper channel.

Here the temperature acts as a regulator but one could also use a finite frequence ω, or a momentum k slightly different from $2k_F$ and $\ln(E_0/k_B T)$ should be replaced by $\ln(E_0/\max(k_B T, \hbar v_F k, \hbar\omega))$. The same calculation for the Cooper channel leads to

$$\operatorname{Re}\overline{\chi}_C^{(\text{ret})}(0) = \rho(0)\ln(E_0\beta). \tag{B.27}$$

We have shown that the elementary diagrams in figure B.3 have logarithmic singularities. Consequently these singularities will appear in all orders of perturbation theory when we include interactions. This is in general not a major problem because it is possible to sum up all these divergencies to all orders. This is achieved by the evaluation of the diagrammatic series shown in figure B.4. The nth order contribution for these diagrams is then just

$$\chi_\mu(q,\omega)\left[-\chi_\mu(q,\omega)V(q)\right]^n, \tag{B.28}$$

which can be summed up for each channel separately as a geometric series

$$\chi_\mu^{\text{RPA}}(q,\omega) = \frac{\chi_\mu(q,\omega)}{1 + \chi_\mu(q,\omega)V(q)}. \tag{B.29}$$

The approximation to restrict the summation to this particuliar subsets of bubble (ladder) diagrams is called RPA (random phase approximation) and it is completely equivalent to the calculation which was done in appendix A. We observe that the RPA cures the singularity in the susceptibility if one has $\chi_\mu \to \infty$. However it diverges when $\chi_\mu(q,\omega)V(q) = -1$. As it was discussed in appendix A the later divergence indicates a phase transition to an ordered state. Since χ_μ has different signs for the Peierls and the Cooper channels, a divergence can occur

in only one channel for a given sign of $V(q)$. In higher dimensions the RPA has proven to be a nice tool to put many phase transitions on microscopic grounds. In *one* dimension however RPA clearly fails to produce correct predictions since a one dimensional system cannot have a finite temperature phase transition. This is already true at a classical level [123] and quantum fluctuation will prevent even more such a phase transition. Thus in one dimension the bubbles and ladders in figure B.4 cannot be summed up separately and mixed diagrams have to be considered. This was done in 1966 by Bychkov *et al.* [124] by the summation of the so–called parquet diagrams. We will not continue this line and we present a much more convenient way to treat the logarithmic singularities wich is shown in the next section.

B.4 The Kadanoff–Wilson renormalization group

B.4.1 The method

In this section we present a method to treat in a convenient and systematic way the singularities met in the previous section. The present description follows a review article by Bourbonnais *et al.* [125]. A more detailed introduction can be found in the book by Peskin and Schroeder [100].

The goal of an renormalization group (RG) approach is that starting from a given theory (*e.g.* a Lagrangian) one wants to construct a new theory (most preferably simpler to solve) which has the same low energy behaviour as the original theory but the high–energy degrees of freedom are "integrated out". This means that we are interested in the long distance behaviour of the problem only. The complexity of the new theory depends crucially on how the low– and high–energy degrees of freedom are coupled together. The RG–procedure is most easily implemented in the euclidean path integral formulation using fermion coherent states [85]:

$$Z = \prod_{p=a,b;\,\sigma\tilde{k}} \int Dz_{p\sigma}^*(\tilde{k}) \int Dz_{p\sigma}(\tilde{k})\; e^{-\frac{1}{\hbar}S[z^*,z]} \qquad (B.30)$$

We have introduced for each mode defined by the numbers p (left or right moving fermions), $\tilde{k} = (k, i\omega_n)$ (Fourier–Matsubara space), σ (spin) a Grassmann variable $z_{p\sigma}(\tilde{k})$. After the discussion in the previous section, the action for weakly

interacting electrons in one dimension is given by

$$
\begin{aligned}
S \;=\;& \sum_{p\sigma\tilde{k}} \frac{1}{\beta} \left[G_p^{(0)}(\tilde{k}) \right]^{-1} z_{p\sigma}^*(\tilde{k}) z_{p\sigma}(\tilde{k}) \\
&+\frac{\hbar\pi v_F g_1}{\beta\ell} \sum_{\substack{\sigma\sigma'\\ \tilde{k}\tilde{k}'\tilde{q}}} (\delta_{\sigma,\sigma'} + \delta_{\sigma,-\sigma'})\, z_{a\sigma}^*(\tilde{k}) z_{b\sigma'}^*(\tilde{k}) z_{a\sigma'}(\tilde{k}' + (2k_F,0) + \tilde{q}) z_{b\sigma}(\tilde{k} - (2k_F,0) - \tilde{q}) \\
&+\frac{\hbar\pi v_F g_2}{\beta\ell} \sum_{\substack{\sigma\sigma'\\ \tilde{k}\tilde{k}'\tilde{q}}} (\delta_{\sigma,\sigma'} + \delta_{\sigma,-\sigma'})\, z_{a\sigma}^*(\tilde{k}) z_{b\sigma'}^*(\tilde{k}) z_{b\sigma'}(\tilde{k}' + \tilde{q}) z_{a\sigma}(\tilde{k} - \tilde{q}) \\
&+\frac{\hbar\pi v_F g_3}{2\beta\ell} \sum_{\substack{p\sigma\sigma'\\ \tilde{k}\tilde{k}'\tilde{q}}} (\delta_{\sigma,\sigma'} + \delta_{\sigma,-\sigma'}) \left(z_{a\sigma}^*(\tilde{k}) z_{a\sigma'}^*(\tilde{k}) z_{b\sigma'}(\tilde{k}' - (2k_F,0) + \tilde{q}) z_{b\sigma}(\tilde{k} - (2k_F,0) - \tilde{q}) \right. \\
&\left. \qquad\qquad +z_{b\sigma}^*(\tilde{k}) z_{b\sigma'}^*(\tilde{k}) z_{a\sigma'}(\tilde{k}' + (2k_F,0) + \tilde{q}) z_{a\sigma}(\tilde{k} + (2k_F,0) - \tilde{q}) \right).
\end{aligned}
\tag{B.31}
$$

All the couplings are expressed in units of $\hbar v_F \pi/a$. As it is usually done in the literature, one neglects the contributions from g_4, assuming that their only effect is a renormalization of Fermi velocities.[6] Then the parameter space for the RG procedure is given by

$$
\mu_S = (G_p^0, g_1, g_2, g_3).
\tag{B.32}
$$

Now we want to integrate out the momenta far from k_F. These are the momenta corresponding to the energy shell $1/2 E_0(l)\mathrm{d}l$ on both sides of the Fermi level (*cf* figure B.1) where l counts the number of succesive iterations of this procedure and $E_0(l) = E_0 e^{-l}$. In other words, the reduction of the bandwith is parametrized by l. The RG scheme is implemented by separating the integration variables $z_{p\sigma}(\tilde{k})$ in an inner and an outer shell:

$$
z_{p\sigma}(\tilde{k}) = \begin{cases} z_{<p\sigma}(\tilde{k}) & \text{for} \quad 2\hbar v_F k \in [-E_0(l)(1+\mathrm{d}l), -E_0(l)] \\ z_{>p\sigma}(\tilde{k}) & \text{for} \quad 2\hbar v_F k \in [E_0(l), E_0(l)(1+\mathrm{d}l)] \end{cases}
\tag{B.33}
$$

We would like to find after the integration over the outer shell an expression of the following form

$$
\begin{aligned}
Z \;=\;& e^{A(l)} \int Dz_<^* \int Dz_<\, e^{S[z_<^*, z_<]_<} \int Dz_>^* \int Dz_>\, e^{S[z_<^*, z_<, z_>^*, z_>]_{\mathrm{d}l}} \\
=\;& e^{A(l+\mathrm{d}l)} \int Dz_<^* \int Dz_<\, e^{S[z_>^*, z_>]_{l+\mathrm{d}l}}.
\end{aligned}
\tag{B.34}
$$

So that this procedure of reducing the cut–off becomes a continuous transformation of the action $S(l)$ and the free energy density $A(l)$ in the limit $\mathrm{d}l \ll 1$. The RG transformation will generate a flow in the parameter space

$$
\mathrm{RG}_{\mathrm{d}l}[\mu(l)] = \mu_S(l + \mathrm{d}l)
\tag{B.35}
$$

---

[6]*cf e.g.* reference [121].

where

$$\mu_S(l) = \left(z(l)G_p^0,\ z_1(l)g_1,\ z_2(l)g_2,\ z_3(l)g_3 \right),\qquad (B.36)$$

and there is nothing which forbids the RG transformation to generate new inter-action terms which were not contained in the original action.

After each RG step the energy cut–off is changed by the factor $s = e^{dl} > 1$ and the energies are rescaled to be

$$
\begin{aligned}
\epsilon'_p &= s\epsilon_p,\\
\omega'_n &= s\omega_n.
\end{aligned}
\qquad (B.37)
$$

The fields are rescaled in such a way that S_0 is a fixed point of the transformation

$$z'_{p\sigma}(\tilde{k}) = z^{-1/2}s^{-1/2}z_{p\sigma}(\tilde{k}). \qquad (B.38)$$

Then the coupling constants g_i transform as

$$g'_i = g_i z_i z^2 \quad i = 1,2,3. \qquad (B.39)$$

In general one is not able to implement the RG equations exactly but one tries to set up a perturbative scheme for small coupling constants. To do so, first one decomposes the action in a contribution from the inner shell only plus the rest

$$S[z^*, z] = S[z^*_<, z_<]_< + S[z^*_<, z_<, z^*_>, z_>] \qquad (B.40)$$

where

$$S[z^*_<, z_<, z^*_>, z_>] = S_0[z^*_>, z_>] + \sum_{i=1}^{4} S_{I,i}[z^*_<, z_<, z^*_>, z_>] \qquad (B.41)$$

and S_I, i having i $z'_>$ in the outer momentum shell. "Integrating out" the low energy modes can then be done perturbatively with respect to $S_0[z^*_>, z_>]$ using the linked cluster theorem[7] :

$$
\begin{aligned}
Z &= e^{A(l)} \int Dz^*_< \int Dz_<\ e^{S[z^*_<, z_<]_<} \int Dz^*_> \int Dz_>\ e^{S_0[z^*_>, z_>]} \exp\left\{ \sum_{i=1}^{4} S_{I,i}[z^*_<, z_<, z^*_>, z_>] \right\}\\
&= e^{A(l)} \int Dz^*_< \int Dz_<\ \exp\left\{ S[z^*_<, z_<]_< + \sum_{n=1}^{\infty} \frac{1}{n!} \left\langle \left(\sum_{i=1}^{4} S_{I,i}[z^*_<, z_<, z^*_>, z_>] \right)^n \right\rangle_{0>,c} \right\}
\end{aligned}
$$

It tells us that the exponential function is developped using the average over the outer momentum shell corresponding to all connected diagrams

$$\langle\ldots\rangle_{0>,c} = Z_{0>}^{-1} \int Dz^*_> \int Dz_>\ (\ldots)\, e^{S_0[z^*_>, z_>]}. \qquad (B.42)$$

In the next section the contribution from the one–loop diagrams are computed, these are the terms coming from $1/2 \left\langle (S_{I,2})^2 \right\rangle_{0>,c}$.

---

[7]See *e.g.* reference [85], p. 96*f*.

B.4.2 One–loop calculations

Incommensurate band filling

At incommensurate filling one can neglegt umklapp scattering g_3 and to calculate the RG flow equations in the running coupling constants up to one–loop level we write $S_{I,2}$ as a sum over different channels where typical terms are shown:

$$S_{I,2} = S_{I,2}^C + S_{I,2}^P + S_{I,2}^L \qquad (B.43)$$
$$S_{I,2}^C \Leftrightarrow z_{a\sigma>}^* z_{b\sigma>}^* z_{b\sigma<} z_{a\sigma<} + \text{c.c.}$$
$$S_{I,2}^P \Leftrightarrow z_{a\sigma>}^* z_{b\sigma<}^* z_{b\sigma>} z_{a\sigma<} + \text{c.c.}$$
$$S_{I,2}^{g_4} \Leftrightarrow z_{a\sigma>}^* z_{b\sigma<}^* z_{b\sigma<} z_{a\sigma>} + z_{a\sigma<}^* z_{b\sigma>}^* z_{b\sigma>} z_{a\sigma<}$$

As it was mentioned previously the g_4 channel does not give logarithmic contributions and at the one–loop level it only readjusts the chemical potential. The flow equations for g_1 and g_2 (neglecting g_4) are computed from the diagrams in figure B.5:

$$z_1(\mathrm{d}l) = 1 - 2g_1(l)I_P(\mathrm{d}l) + g_2(l)\left[I_P(\mathrm{d}l) + I_C(\mathrm{d}l)\right] \qquad (B.44)$$

$$z_2(\mathrm{d}l) = 1 + \frac{g_1^2(l)}{g_2(l)}I_C(\mathrm{d}l) + g_2(l)\left[I_p(\mathrm{d}l) + I_C(\mathrm{d}l)\right] \qquad (B.45)$$

The contribution *e.g.* from the Peierls channel can be evaluated in exactly the same way as in the previous section:

$$
I_P(\mathrm{d}l) \stackrel{(B.12)}{=} -\frac{\hbar\pi v_F}{\beta\ell}\sum_{k_>,n_1} G_b^{(0)}(k - 2k_F, i\omega_{n_1} - i\omega_n^{(b)})G_a^{(0)}(k, i\omega_{n_1})
$$

$$
\stackrel{(B.24)}{\underset{(\ell\to\infty)}{=}} \hbar\pi v_F \left(\int_{-E_0(l)/2}^{-E_0(l+\mathrm{d}l)/2} + \int_{E_0(l+\mathrm{d}l)/2}^{E_0(l)/2} \right) \mathrm{d}\epsilon\, \rho(\epsilon)\frac{\tanh(\beta\epsilon/2)}{4\epsilon}
$$

$$
= \frac{1}{2}\mathrm{d}l + \mathcal{O}(\mathrm{d}l^2) \qquad (B.46)
$$

The density of states for a linear dispersion in one dimension equals the constant $1/(\hbar\pi v_F)$ which cancels the prefactor in the second equation. We know from the previous calculation that

$$I_P(\mathrm{d}l) = -I_C(\mathrm{d}l). \qquad (B.47)$$

This allows us to write down the flow equations at the one–loop level

$$\frac{\mathrm{d}g_1}{\mathrm{d}l} = -g_1^2, \qquad (B.48)$$

$$\frac{\mathrm{d}}{\mathrm{d}l}\left(2g_2 - g_1\right) = 0. \qquad (B.49)$$

The first equation can be integrated:

$$g_1(l) = \frac{g_1(0)}{1 + g_1(0)l} \qquad (B.50)$$
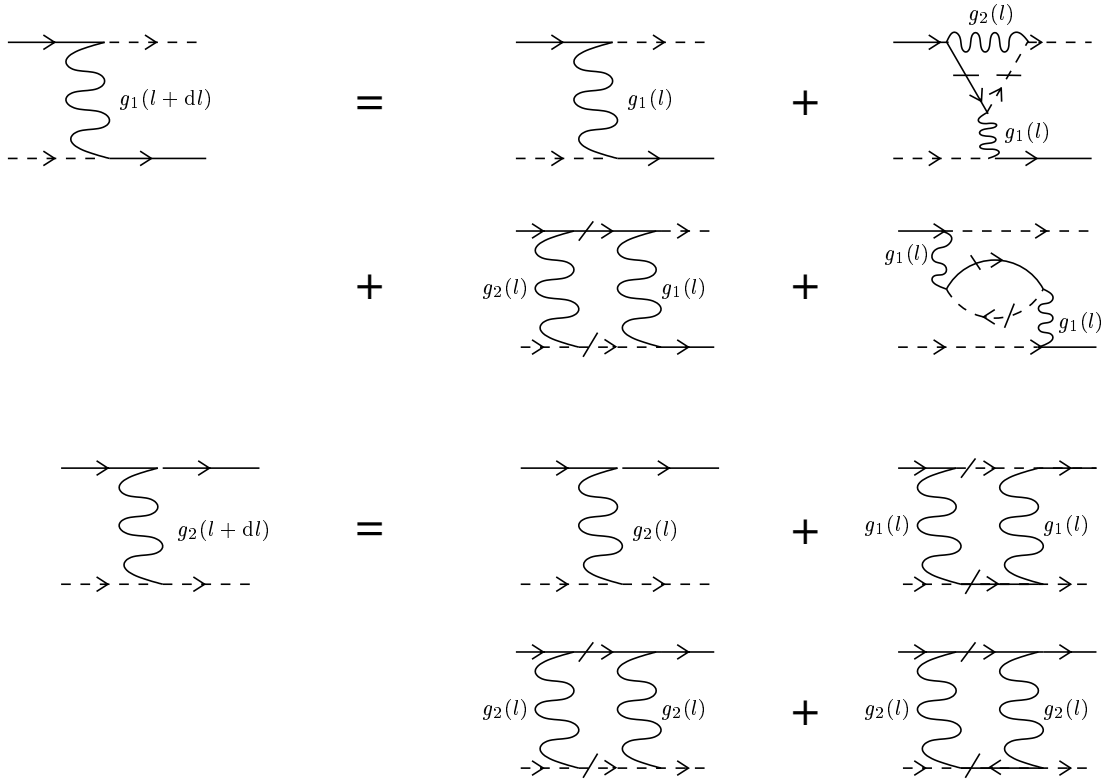
Figure B.5: The one loop diagrams for the flow equations of the Cooper and the Peierls channel. The slashed propagator lines refer to a particle or hole in the outer shell.

From this solution one sees that if $g_1(0)$ is repulsive g_1 scales to zero, what means that backward scattering is marginally irrelevant. If $g_1(0)$ is attractive, g_1 flows to the strong coupling region and diverges eventually, indicating that g_1 is marginally relevant and the system should develop a spin gap[8]. Although the divergence is an artefact of the one–loop calculation, the flow to strong coupling is believed to be preserved to all orders. A good reason to believe that this is true comes from the fact that the system can be solved exactly by bosonization at the Luther–Emery line wich is at $g_1(l_{LE}) = -\,^6/_5$. This calculation confirms the existence of a spin gap [126].

Two other important properties or the one–dimensional electron gas can be deduced from the flow equations. First the combination $2g_2 - g_1$ is invariant under the flow. It has been shown [127] that this is a consequence of particle conservation on each branch separately in the absence of umklapp scattering processes g_3. Moreover the two equations are completely decoupled. It has been noted by Dzyaloshinskii and Larkin that the interaction terms of the action for g_1 and g_2 can be rewritten as [128]

$$S_I[z_<^*, z_<]_l = -\hbar\pi v_F(2g_2(l) - g_1(l))\sum_{p\tilde{q}} n_p(\tilde{q})n_{-p}(-\tilde{q}) + \hbar\pi v_F g_1(l)\sum_{p\tilde{q}} \mathbf{S}_p(\tilde{q})\cdot\mathbf{S}_{-p}(-\tilde{q})$$

(B.51)

where n_p is the particle density and $\mathbf{S}_p$ the spin density at cut-off $l \gg 0$

$$n_p(\tilde{q}) = \frac{1}{2}\sqrt{\frac{1}{\beta\ell}}\sum_{\sigma\tilde{k}_<} z_{p\sigma<}^*(\tilde{k} + \tilde{q})z_{p\sigma<}(\tilde{k}),$$

(B.52)

$$\mathbf{S}_p(\tilde{q}) = \frac{1}{2}\sqrt{\frac{1}{\beta\ell}}\sum_{\sigma\sigma'\tilde{k}_<} z_{p\sigma<}^*(\tilde{k} + \tilde{q})\boldsymbol{\sigma}_{\sigma\sigma'}z_{p\sigma'<}(\tilde{k}).$$

(B.53)

One deduces that the long wavelength spin degrees of freedom are independent of their charge counter part. This property is true to all orders and it is not restricted to perturbation theory. It is known as *spin–charge separation* in a *Luttinger liquid*[9].

---

[8]The reason for this expectation is most easily seen using bosonization. From the bosonized Hamiltonian one can argue that in the limit $g_1 \to \infty$ the system is locked in one of the classical minima, and hence all the excitations of the bosonic fields are massive, *i.e.* there is a gap in the spectrum. A pedagogical description on this subject can be found in reference [73], p. 63 *f.*

[9]Bosonization can give complementary insight to the phenomenon of spin–charge separation in one–dimensional systems, *c.f.* p. 50 *ff* in reference [73]. The notion of a Luttinger liquid refers to the breakdown of the Fermi liquid picture of quasi–particles excitations [129]. One shows quite generally for one–dimensional systems [73] that the density of states vanishes as a power law at the Fermi level

$$\rho(\epsilon) \propto |\epsilon|^{\frac{1}{4}[K_\rho + K_\rho^{-1}] - \frac{1}{2}}$$

(B.54)

Half–filling

As we have shown previously, the g_3 umklapp scattering processes become possible at half–filling. The additional contributions to $S_{I,2}$ are:

$$
\begin{aligned}
S_{I,2}^{g_3} &\Leftrightarrow z_{a\sigma>}^* z_{a\sigma<}^* z_{b\sigma>} z_{b\sigma>} + \text{c.c.} \\
&\Leftrightarrow z_{a\sigma>}^* z_{a\sigma>}^* z_{b\sigma<} z_{b\sigma<} + z_{a\sigma<}^* z_{a\sigma<}^* z_{b\sigma>} z_{b\sigma>} + \text{c.c.}
\end{aligned}
\tag{B.56}
$$

Only the first line gives logarithmic corrections at the one–loop level and the same analysis as for the case of incommensurate filling gives the following flow equations:

$$
\frac{\mathrm{d}g_1}{\mathrm{d}l} = -g_1^2
\tag{B.57}
$$

$$
\frac{\mathrm{d}}{\mathrm{d}l}\left(2g_2 - g_1\right) = g_3^2
\tag{B.58}
$$

$$
\frac{\mathrm{d}g_3}{\mathrm{d}l} = g_3\left(2g_2 - g_1\right)
\tag{B.59}
$$

One observes that the umklapp scattering influences only the charge sector, and the spin sector stays completely uncoupled. Umklapp scattering changes right–moving electrons into left–moving ones (and vice versa) and the associated rate of change is shown in the second flow equation. If one injects the third equation into the second one, one obtains

$$
\left(2g_2 - g_1\right)\frac{\mathrm{d}}{\mathrm{d}l}\left(2g_2 - g_1\right) - g_3\frac{\mathrm{d}}{\mathrm{d}l}g_3 = 0
\tag{B.60}
$$

which says that the flow follows hyperbolae given by

$$
C = \left(2g_2 - g_1\right)^2 - g_3^2.
\tag{B.61}
$$

The possible flows are shown in figure B.6. We see that if $g_1 - 2g_2 > |g_3|$, g_3 scales to zero. Otherwise $g_1 - g_2$ and g_3 flow to strong coupling and one expects an energy gap towards charge excitations.

---

where the exponent is controlled by the Luttinger liquid parameter K_ρ defined by

$$
K_\rho = \left[\frac{1 + g_4 - (2g_2 - g_1)/2}{1 + g_4 + (2g_2 - g_1)/2}\right].
\tag{B.55}
$$

The interpretation of this result needs some care as the vanishing single–particle density does not indicate that there are no states available close to the Fermi level. It shows "only" that there are no low–energy single–particle excitations but the system is actually a metal due to collective excitations only!
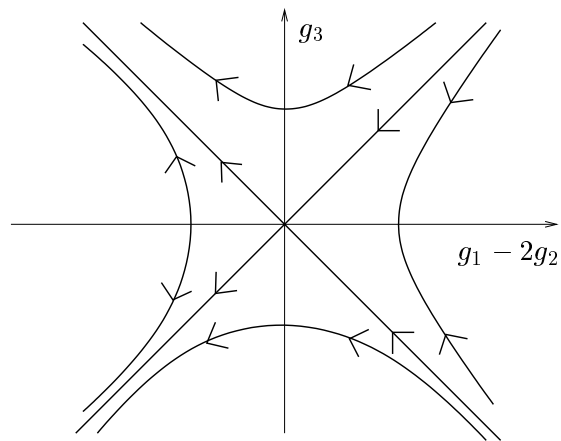
Figure B.6: A contour sketch of the flow equations in the charge sector.

Appendix C

Stochastic series expansion: a QMC algorithm

C.1 Summary

In chapter 5 we study numerically the Heisenberg model on the honeycomb lattice for CNT. This is done using quantum Monte Carlo (QMC) techniques. Here we give the technical details of the algorithm used there, namely the stochastic series expansion (SSE) representation with directed loops updates.

We start this appendix with a short and very sketchy introduction to QMC methods and we reference to the ALPS project which makes available an efficient SSE code as open source. Then we describe the SSE representation and subsequently the update scheme used, followed by a discussion about how to evaluate observables such as total energy, susceptibility, and imaginary time correlation functions. At the end, one can find supplementary data of our MC simulations presented in chapter 5.

However we do not give an introduction to MC simulation in general as this can be found in countless textbooks. A nice and concise introduction can be found in the book by Hammersley and Handscomb [115], *cf* in particular chapter 9. For the elementary mathematical background one can consult chapter XV in Feller's book [130].

The subsequent descriptions of the SSE representation and the update schemes follow closely reference [131].

C.2   Overview of QMC representations and SSE update schemes

We give an overview of the most common QMC algorithms which are concerned with the evaluation of the partition function

$$Z = \text{Tr} \exp \left(-\beta \hat{H} \right) \qquad\qquad (C.1)$$

for a quantum mechanical Hamiltonian $\hat{H}$. To bring this expression into a tractable form one needs to find a mapping which reduces the problem to the evaluation of a classical partition function. Following Wessel [132], three different routes to such a mapping are known

- The *world line* representation is based on the mapping of spin–1/2 systems onto a classical Ising model. It can only be used to a very limited number of systems (*e.g.* isotropic Heisenberg model) but it gives usually very efficient algorithms.

- The *path integral* method is a continous time representation based on the perturbative expansion of the path integral using the Trotter–Suzuki formula. This reprenstation can be used quite generally and gives good efficiency if the diagonal terms are large compared to the off–diagonal terms. However its implementation is often quite complicated and very system dependent.

- The *SSE* representation is discrete in time and is a high–temperature series expansion of the partition function. This representation is most widely used nowadays. This is due to its universal applicability, its good efficiency, and its relatively easy implementation.

Here we will only describe the SSE representation. This method was introduced in 1991 by Sandvik and Kurkijärvi [133, 134] by generalizing an old method due to Handscomb[1]. In the original formulation of the method, *local* MC updates were used. These updates suffer from critical slowing down near phase transitions and give rise to long autocorrelation times of observables[2]. These issues were improved considerably by Sandvik's non–local *operator–loop* update [135]. More recently it was realized that the operator–loop udate is just one possibility out of a whole class of update algorithms. This lead to the even more efficient *directed loop* algorithm [131, 136, 137].

---

[1] *cf* p. 124 of reference [115].

[2] Defintion of the autocorrelation time: We note by $A(t)$ the measurement of the observable A at the MC step t. The autocorrelation time τ_A depends on the observable and it is defined from the expression $\langle A_t A_{t+\tau_0} \rangle - \langle A \rangle^2 \propto \exp\left(-\tau_0/\tau_A \right)$ for $\tau_0 \gg 1$.

To obtain the results of chapter 5 we used and modified the ALPS[3] SSE code which was written by Alet and Troyer. This code implements the generalized directed loop method [131] and can be used for unfrustrated spin systems. A description of the SSE representation and the generalized directed loop updates follows in the subsequent sections.

C.3 SSE representation

The starting point of the SSE method is the high temperature series expansion of the partition function

$$Z = \sum_n^\infty \sum_\alpha \frac{\beta^n}{n!} \langle \alpha | \left(-\hat{H} \right)^n | \alpha \rangle \qquad (C.2)$$

where $\{|\alpha\rangle\}$ is an orthonormal basis set of the Hilbert space in which the Hamiltionian $\hat{H}$ acts. The SSE algorithm outlined below can be applied quite generally, *e.g.* to systems with multiple particle exchange or long–range interactions. However in this appendix we will limit the discussion to lattice Hamiltonians with two–particle short range interactions and we will consider the isotropic spin 1/2 Heisenberg model (defined in equation 5.1) as an example. Such Hamiltonians can be written as a sum over single–bond terms only

$$\hat{H} = -\sum_{b=1}^M H_b \qquad (C.3)$$

where M is the number of different operators H_b where each of them associated with one of the lattice bonds B. We define $B = (i(b), j(b))$ as the bond connecting sites i and j. For the Heisenberg model such a decomposition is easily done, a bond Hamiltonian H_b can be either non–diagonal in the S^z basis

$$H_b = -\frac{J}{2} \left(S^+_{i(b)} S^-_{j(b)} + S^-_{i(b)} S^+_{j(b)} \right) = H^o_{ij} \qquad (C.4)$$

or diagonal

$$H_b = -J S^z_{i(b)} S^z_{j(b)} = H^d_{ij}. \qquad (C.5)$$

---

[3]ALPS stands for Algorithms and Libraries for Physics Simulations and it is "an open source effort aiming at providing high-end simulation codes for strongly correlated quantum mechanical systems as well as C++ libraries for simplifying the development of such code. ALPS strives to increase software reuse in the physics community." A description of this project is given in F. Alet *et al.*, cond-mat/0410407 and M. Troyer, B. Ammon and E. Heeb, Lecture Notes in Computer Science, Vol. 1505, p. 191 (1998). The source code can be obtained at http://alps.comp-phys.org/.

Therefore the number of bond Hamiltonians M is twice the total number of bonds in the Heisenberg model. We rewrite equation (C.2) using the bond operators

$$Z = \sum_{n=0}^{\infty} \sum_{\{S_n\}} \sum_{\alpha(0),...,\alpha(n)} \frac{\beta^n}{n!} \prod_{p=1}^{n} \langle \alpha(p)| H_{b_p} |\alpha(p-1)\rangle \tag{C.6}$$

where $\{S_n\}$ is the set of all operator strings which are the concatenations of n bond Hamiltonians. Basis sets $\{|\alpha(p)\rangle\}$ have been inserted between each pair of bond Hamiltonians. Therefore the state $|\alpha(p)\rangle$ can be regarded as the p–step propagated state from the initial state:

$$|\alpha(p)\rangle = \prod_{j=1}^{p} H_{b_j} |\alpha(0)\rangle \tag{C.7}$$

As we are evaluating a trace, we have to assure periodicity, *i.e.* $|\alpha(n)\rangle = |\alpha(0)\rangle$.

In practice the infinite sum over n is truncated at a value of order $L\beta$, where L is the number of lattice sites. The exact value is determined and adjusted during equilibration of the simulation. After equilibration the cut–off is fixed.

In order to facilitate implementation, it is desirable to work with operator strings of constant length Λ. This is achieved by inserting $(\Lambda - n)$ unity operators. There are $\begin{pmatrix} \Lambda \\ n \end{pmatrix} = \frac{\Lambda!}{n!(\Lambda-n)!}$ different ways to do this. If we define $H_0 = \text{Id}$, the truncated high–temperature expansion can be written as

$$Z = \sum_{n=0}^{\Lambda} \sum_{\{S_{\Lambda,n}\}} \sum_{\alpha(0),...,\alpha(\Lambda)} \frac{\beta^n (\Lambda - n)!}{\Lambda!} \prod_{p=1}^{\Lambda} \langle \alpha(p)| H_{b_p} |\alpha(p-1)\rangle \tag{C.8}$$

where n now denotes the number of non–unity operators in the operator string $S_\Lambda = (b_1, \ldots, b_\Lambda)$, with $0 \le b_p \le M$, $p = 1, \ldots, \Lambda$. In figure C.1 we consider a very simple example of an operator string in the four site Heisenberg model as an illustration. From equation (C.8) we deduce that the weight associated to a configuration is given by

$$W(\alpha(0), S_{\Lambda,n}) = \frac{\beta^n (\Lambda - n)!}{\Lambda!} \langle \alpha(0)| \prod_{p=1}^{\Lambda} H_{b_p} |\alpha(0)\rangle . \tag{C.9}$$

A MC importance sampling is however only possible if we can interpret the associated weights as probabilities, *i.e.* all the matrix elements of bond operators should be positive. Negative diagonal matrix elements can be cured just by adding a positive constant $C = C_0 + \epsilon$, where C_0 is the minimal value for which all diagonal matrix elements are positive. In our example of the Heisenberg model $C_0 = |J|/4$. $\epsilon \ge 0$ is an additional offset which can influence the efficiency of the
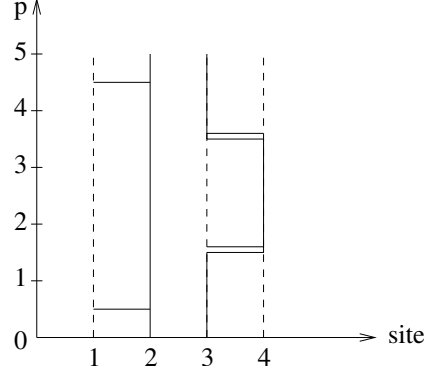
Figure C.1: We consider the example of the four site Heisenberg model and we give a graphical representation (after reference [135]) of the operator string $S_\Lambda = \left(H^d_{(1,2)}, H^o_{(3,4)}, \mathrm{Id}, H^o_{(3,4)}, H^d_{(1,2)} \right)$ where we have set the cutoff Λ to 5. The horizontal axis is used to show the different sites and the vertical axis represents the propagation index. The initial state is chosen as $|\alpha(0)\rangle = |\downarrow\uparrow\uparrow\downarrow\rangle$. Solid (dashed) vertical lines indicate up (down) spin states. Diagonal non–unity operators are drawn as a single horizontal line, whereas non–diagonal operators are drawn as a double line.

SSE algorithm[4]. Unfortunately there exists no general strategy to get rid of negative off–diagonal matrix elements. This is known as the "sign problem" in QMC. A solution is however possible for bosonic models, ferromagnetic spin models, and antiferromagnetic models on bipartite lattices (*e.g.* the Heisenberg model on the honeycomb lattice). In the case of antiferromagnetically coupled spins on a bipartite lattice the simple remedy is to perform a local gauge transformation on one sublattice only:

$$S_i^\pm \quad \longrightarrow \quad (-1)^i \, S_i^\pm \tag{C.10}$$

$$J/2 \left(S_i^+ S_j^- + S_i^- S_j^+ \right) \quad \longrightarrow \quad -J/2 \left(S_i^+ S_j^- + S_i^- S_j^+ \right) \tag{C.11}$$

Once we have a model and a basis set where we can guarantee the positivity of all matrix elements, we have to generate new configurations from an initial one to evaluate stochastically the partition function. In practice an algorithm which generates new configurations has to be *ergodic* (all configurations can be obtained in a finite number of MC steps from any other configuration) and to satisfy *detailed balance*[5], *i.e.* the transition probabilities P to go from a state

---

[4] *cf* references [136] and [131] for details.

[5] In the mathematical literature (*cf e.g.* references [130] and [115]) instead of "ergodicity" one would read "irreducible, aperiodic Markov chain" and the detailed balance condition (*e.g.* equation (9.3.8) in reference [115]) is a somewhat stronger condition what is actually needed to prove the convergence theorem for Markov chains but a very useful one in applications.

$(\alpha(0), S_{\Lambda,n})$ to a new state $(\alpha'(0), S'_{\Lambda,n'})$ have to satisfy

$$\frac{\mathrm{P}\left[(\alpha(0), S_{\Lambda,n}) \to (\alpha'(0), S'_{\Lambda,n'})\right]}{\mathrm{P}\left[(\alpha'(0), S'_{\Lambda,n'}) \to (\alpha(0), S_{\Lambda,n})\right]} = \frac{W(\alpha'(0), S'_{\Lambda,n'})}{W(\alpha(0), S_{\Lambda,n})}. \tag{C.12}$$

In the next two sections we will describe such update algorithms: the *operator loop* and the *directed loop* updates.

C.4   Operator loop updates

A MC step in Sandvik's SSE algorithm with operator loop updates [135] in the operator string consists of two parts. First one attemps to insert or remove identity operators into the operator string and secondly to make non-local worm updates which will change the initial state and the operator string but without affecting the expansion order. During the diagonal updates one proposes to insert, respectively to remove, unity operators. Evidently such substitutions changes the expansion order n. This diagonal update are done by traversing the whole operator string $S_{\Lambda,n}(p)$, $p = 1, \ldots, \Lambda$. If $S_{\Lambda,n}(p)$ is a unity operator H_0 it is replaced by a bond Hamiltonian with a probability compatible with detailed balance given below. The reverse process is the substitution of a bond Hamiltionian H_{b_p} by a unity operator. Such an update is only meaningful if H_{b_p} is diagonal, *i.e.* H_{b_p} does not change the propagated state $(|\alpha(p)\rangle = |\alpha(p-1)\rangle)$, otherwise the associated weight is zero.

As mentioned before the acceptance probabilities have to verify detailed balance. As there are M possible choices for H_{b_p} we have

$$\frac{\mathrm{P}(H_0 \to H_{b_p})}{\mathrm{P}(H_{b_p} \to H_0)} = \frac{M W(\alpha, S_{\Lambda,n+1})}{W(\alpha, S_{\Lambda,n})}. \tag{C.13}$$

For such updates it is possible to use the Metropolis algorithm

$$\mathrm{P}(H_0 \to H_{b_p}) = \min\left[1, \frac{M\beta \langle \alpha(p)| H_{b_p} |\alpha(p-1)\rangle}{\Lambda - n}\right], \tag{C.14}$$

$$\mathrm{P}(H_{b_p} \to H_0) = \min\left[1, \frac{(\Lambda - n + 1)\delta_{|\alpha(p)\rangle, |\alpha(p-1)\rangle}}{M\beta \langle \alpha(p)| H_{b_p} |\alpha(p-1)\rangle}\right] \tag{C.15}$$

which always satisfies detailed balance by construction.

Now we come to the second part of the update procedure: We modify the configuration obtained from the preceding local update by a fixed number of non–local, so–called operator loop updates. During these updates the expansion order n is constant and it has been shown to be useful to employ a new representation of the operator string in terms of linked vertices. We associate a vertex (*cf* figure C.2) with each non–unity operator (*i.e.* $H_{b_p} \neq H_0$) in the operator string. This
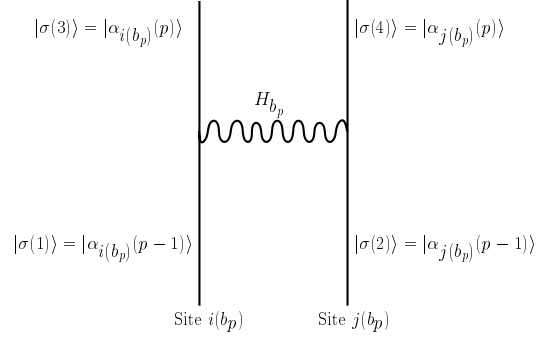
$|\sigma(3)\rangle = |\alpha_{i(b_p)}(p)\rangle$

$|\sigma(4)\rangle = |\alpha_{j(b_p)}(p)\rangle$

H_{b_p}

$|\sigma(1)\rangle = |\alpha_{i(b_p)}(p-1)\rangle$

$|\sigma(2)\rangle = |\alpha_{j(b_p)}(p-1)\rangle$

Site $i(b_p)$ Site $j(b_p)$

Figure C.2: The vertex state $\boldsymbol{\Sigma}_p$ is equal to the direct product of the local states on its four legs: $\boldsymbol{\Sigma}_p = |\sigma(1)\rangle \otimes |\sigma(2)\rangle \otimes |\sigma(3)\rangle \otimes |\sigma(4)\rangle$. This figure is taken from reference [131].

means that each horizontal wiggly line in figure C.1 corresponds to a vertex. More precisely a vertex consists of a non–unity bond Hamiltonian H_{b_p} and four legs. The two lower legs (1 and 2) carry the local states $|\alpha_{i(b_p)}(p-1)\rangle$ and $|\alpha_{j(b_p)}(p-1)\rangle$ before the action of H_{b_p} and the upper legs (3 and 4) carry these states when propagated by H_{b_p}, as it is shown in figure C.2. Let us define the vertex state by

$$\boldsymbol{\Sigma}_p = |\sigma(1)\rangle \otimes |\sigma(2)\rangle \otimes |\sigma(3)\rangle \otimes |\sigma(4)\rangle, \tag{C.16}$$

and at each bond the weight of this vertex is given by

$$W(b_p, \boldsymbol{\Sigma}_p) = (\langle\sigma(3)| \otimes \langle\sigma(4)|)\tilde{H}_{b_p}(|\sigma(1)\rangle \otimes \sigma(2)\rangle), \tag{C.17}$$

where $\tilde{H}_b$ is the restriction of the bond Hamiltonian H_b to the states at sites $i(b)$ and $j(b)$. Therefore the vertex weights equal the matrix elements in equation (C.8)

$$W(b_p, \boldsymbol{\Sigma}_p) = \langle\alpha(p)|H_{b_p}|\alpha(p-1)\rangle. \tag{C.18}$$

To summarize, the operator string can be represented conveniently as a list of vertices $\boldsymbol{\Sigma}_p$, $0 \leq p \leq n-1$. To understand this representation better we mention that in a programming language the vertex list would be represented by two one–dimensional containers [136]:

- vtx[p], $p = 0, \ldots, n-1$
  This list gives the type of the operator H_{b_p} for each vertex.

- link[j], $j = 0, \ldots, 4n-1$
  link[4p+i] ($p = 0, \ldots, n-1$; $i = 0, 1, 2, 3$) gives the link (an integer referring to another element in link[ ]) for the leg $i+1$ of vertex p. This list is double–linked, *i.e.* link[a] = b $\Leftrightarrow$ link[b] = a.

The basic idea of the operator–loop update is to make changes in this vertex list along *closed* loops defining a new operator string $S'_{\Lambda,n'}$ and new initial state $|\alpha'(0)\rangle$. The closed operator–loop is contructed with the help of a *worm*.

Inserting the worm: A worm is created by the insertion of the product of two operators, A_0 and its hermitian conjugate $A_0^\dagger$, at a random leg l_1 in the vertex list. The state at leg l_1 is denoted by $|s_1\rangle$. One of the two operators will represent the head of the worm and the other one the tail. In general the head and the direction of propagation will be selected by two random choices:

1. Choose between insertion of $A_0^\dagger A_0$ or $A_0 A_0^\dagger$.

2. Choose either A_0 or $A_0^\dagger$ to be the head. If the first operator in the product is chosen the propagation is in positive direction of propagation (increasing p), and if the second operator is chosen the direction of propagation is negative (decreasing p).

Only the head of the worm will move as the tail is kept fixed. Actually the head will be moved until it comes back to the insertion leg l_1. Then the construction of the worm is terminated and the worm annihilates. During its way, the worm has updated all vertices where it passed by. Let us say we have choosen A ($= A_0$ or $A_0^\dagger$) to be the head of the worm. The head will act on the state $|s_1\rangle$ by an operator $\widetilde{T}_0$ which gives again a normalized state

$$\widetilde{T}_0 \, |s_1\rangle = \frac{T_0 \, |s_1\rangle}{||T_0 \, |s_1\rangle \, ||} \tag{C.19}$$

where the operator T_0 is given by

$$T_0 = \begin{cases} A^\dagger, & \text{for positive direction of propagation,} \\ A, & \text{for negative direction of propagation.} \end{cases} \tag{C.20}$$

Figure C.3 illustrates this transformation. In general a worm is inserted with a certain probability $P_{\text{insert}}(T_0, s_1)$. In our example of a spin$-\frac{1}{2}$ model[6] we always insert a worm, because we define the following insertion probabilities

$$P_{\text{insert}}(S^\pm, m) = \delta_{m, \mp 1/2}. \tag{C.21}$$

Moving the worm up to annihilation: According to the direction of propagation the worm enters the first vertex V_1 on the entrance leg l_1. Before the arrival of the worm, the leg l_1 carries the state $|s_1\rangle$. This state will be transformed to $\widetilde{T}_0 \, |s_1\rangle$ by the worm. Then the worm chooses an exit l_1', one of the four legs of vertex V_1, with probabilities compatible with detailed balance. This probabilities are defined in the next section. We note that the direction of propagation can be inverted, depending on what leg is chosen. The new operator A_1 on the head is:

$$\begin{aligned} A_1 &= A_0 \,, & \text{no inversion of direction of propagation} \\ A_1 &= A_0^\dagger, & \text{inversion of direction of propagation} \end{aligned} \tag{C.22}$$

Following the vertex list, the worm will enter next into vertex V_2 on leg $l_2 =$

---

[6]Other models are discussed on page 9 of reference [131].
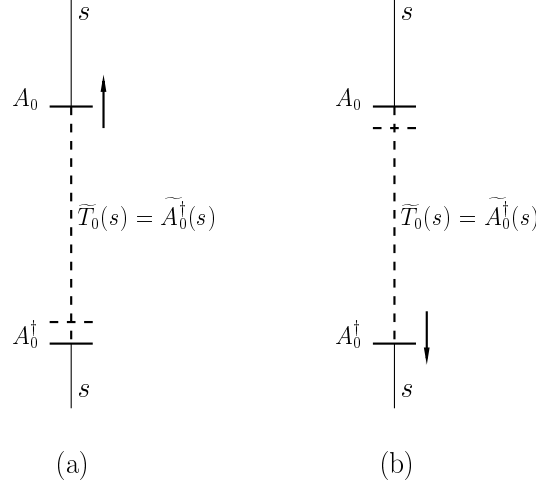
Figure C.3: The two possibilities of moving the worm after insertion of an initial pair $A_0^\dagger A_0$. (a) The operator A_0 is moved *upwards* in propagation direction. As a result, the transformation induced on the state s is $T_0 = A_0^\dagger$ (the new state is $\widetilde{T}_0(s) = \widetilde{A}_0^\dagger(s)$). (b) The operator $A_0^\dagger$ is moved *downwards* in negative propagation direction. The transformation induced on the state s is again $T_0 = A_0^\dagger$ (the new state being $\widetilde{T}_0(s) = \widetilde{A}_0^\dagger(s)$). Dashed horizontal lines indicate where the operators were before they were moved. Figure and caption are taken from reference [131].
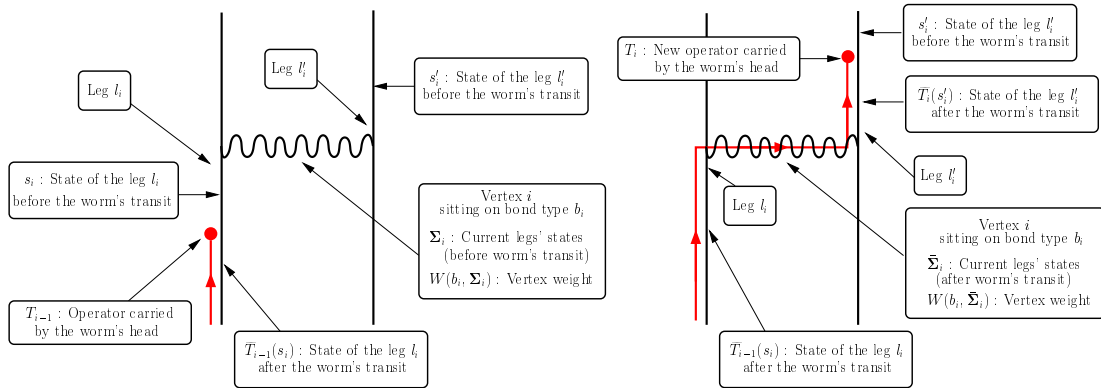
Figure C.4: Worm entering (left hand side) and leaving (right hand side) the i-th vertex during its construction. The figures were taken from reference [131].

l_1'. Again the state $|s_2\rangle$ carried by the leg l_2 is transfered to $\widetilde{T}_1 |s_2\rangle$ and the worm continuous through exit leg l_2' to another vertex. This procedure of worm propagation is shown in figure C.4 and it is continued until the worm returns to its initial leg. Then the worm is closed and the operator loop update is finished.

In the next section we discuss what probabilities have to be assigned to an exit leg to get an efficient algorithm which satisfies detailed balance.

C.5 Generalized directed loops

C.5.1 Worm weights and local detailed balance

As previously discussed, we still have to determine the conditional probability $P_{b_i}(\boldsymbol{\Sigma}_i, T_{i-1} \to T_i, l_i \to l_i')$ of exiting on leg l_i', knowing the worm has entered on leg l_1. Originally Sandvik [135] proposed

$$P_{b_i}(\boldsymbol{\Sigma}_i, T_{i-1} \to T_i, l_i \to l_i') \propto W(b_i, \bar{\boldsymbol{\Sigma}}_i) \qquad (C.23)$$

where $\bar{\boldsymbol{\Sigma}}_i$ is the vertex after the passage of the worm. This choice is often called *heat–bath solution* and it is generic for all models. However it suffers from serious efficiency problems due to *bounce* processes [136] which are processes where the worm enters and exits through the same leg, *i.e.* $l_i = l_i'$. Therefore Syljuåsen and Sandvik looked for probability assignments which minimize bounces [136, 137]. In particular they showed that it is sufficient to assure detailed balance at each vertex separately

$$W(b_i, \boldsymbol{\Sigma}_i)P_{b_i}(\boldsymbol{\Sigma}_i, T_{i-1} \to T_i, l_i \to l_i') = W(b_i, \bar{\boldsymbol{\Sigma}}_i)P_{b_i}(\bar{\boldsymbol{\Sigma}}_i, T_i^\dagger \to T_{i-1}^\dagger, l_i' \to l_i)$$
$$(C.24)$$

to fulfill detailed balance for the operator loop update. Evidently equation (C.23) satisfies this condition. Alet, Wessel and Troyer generalized equation (C.24) by adding an additional weight factor which is the worm's head matrix element

$$f(T, s) \equiv \langle \widetilde{T}(s)|T|s\rangle = \langle s|\widetilde{T}^\dagger T|s\rangle. \qquad (C.25)$$

Their local detailed balance condition then writes

$$f(T_{i-1}, s_i)W(b_i, \boldsymbol{\Sigma}_i)P_{b_i}(\boldsymbol{\Sigma}_i, T_{i-1} \to T_i, l_i \to l_i') \; =$$
$$f(T_i^\dagger, \widetilde{T}_i(s_i'))W(b_i, \bar{\boldsymbol{\Sigma}}_i)P_{b_i}(\bar{\boldsymbol{\Sigma}}_i, T_i^\dagger \to T_{i-1}^\dagger, l_i' \to l_i) \qquad . \qquad (C.26)$$

The proof that this condition implies detailed balance is reproduced in the next section. Before we come to this point let us make some remarks:

- The condition which is actually needed to prove detailed balance is

$$f(T^\dagger, \widetilde{T}(s)) = f(T, s) \qquad (C.27)$$

which is satisfied by the choice (C.25), due to $\widetilde{T}^\dagger \widetilde{T} T^\dagger \widetilde{T} = \widetilde{T}^\dagger \widetilde{T} \widetilde{T}^\dagger T = \widetilde{T}^\dagger \mathrm{Id} T$.

- The generalized directed loop equations (C.26) are a true generalization of equations (C.24). They can be recovered by setting $f(T, s) \equiv 1$ which satisfies (C.27) equally.

- Minimizing the bounce probabilities under the restriction of local detailed balance will lead to a *linear programming* problem, discussed in section C.5.3.

- The worm weights in our example are

$$f(S^\pm, m) = \langle m \pm 1 | S^\pm | m \rangle = \sqrt{3/4 - m(m \pm 1)} \qquad m = \pm \, 1/2. \quad \text{(C.28)}$$

C.5.2 Proof of detailed balance

We start with the probability to create a worm w, which comes back to initial position by passing through exactly N vertices:

$$P^w = P_{\text{init}} \cdot P_{\text{insert}}(T_0, s_1) \cdot \prod_{i=1}^{N} P_{b_i}(\boldsymbol{\Sigma}_i, T_{i-1} \to T_i, l_i \to l_i') \qquad \text{(C.29)}$$

P_{init} denotes the uniform probability of choosing the insertion leg. The *antiworm* $\bar{w}$ is inserted at the same leg as w but it will pass the N vertices in reverse order:

$$P^{\bar{w}} = P_{\text{init}} \cdot P_{\text{insert}}(T_N^\dagger, \widetilde{T}_N(s_N')) \cdot \prod_{i=1}^{N} P_{b_i}(\bar{\boldsymbol{\Sigma}}_i, T_i^\dagger \to T_{i-1}^\dagger, l_i' \to l_i) \qquad \text{(C.30)}$$

Then the detailed balance condition can be expressed as

$$\frac{P^w}{P^{\bar{w}}} = \prod_{i=1}^{N} \frac{W(b_i, \boldsymbol{\Sigma}_i)}{W(b_i, \bar{\boldsymbol{\Sigma}}_i)}. \qquad \text{(C.31)}$$

Now we want to show that detailed balance is a consequence of equations (C.26) and (C.27):

$$\frac{P^w}{P^{\bar{w}}} \quad = \quad \frac{P_{\text{insert}}(T_0, s_1)}{P_{\text{insert}}(T_N^\dagger, \widetilde{T}_N(s_N'))} \prod_{i=1}^{N} \frac{P_{b_i}(\boldsymbol{\Sigma}_i, T_{i-1} \to T_i, l_i \to l_i')}{P_{b_i}(\bar{\boldsymbol{\Sigma}}_i, T_i^\dagger \to T_{i-1}^\dagger, l_i' \to l_i)} \quad \text{(C.32)}$$

$$\overset{(C.26)}{=} \quad \frac{P_{\text{insert}}(T_0, s_1)}{P_{\text{insert}}(T_N^\dagger, \widetilde{T}_N(s_N'))} \prod_{i=1}^{N} \frac{f(T_{i-1}, s_i) W(b_i, \boldsymbol{\Sigma}_i)}{f(T_i^\dagger, \widetilde{T}_i(s_i')) W(b_i, \bar{\boldsymbol{\Sigma}}_i)} \quad \text{(C.33)}$$

$$\overset{(C.27)}{=} \quad \frac{P_{\text{insert}}(T_0, s_1)}{P_{\text{insert}}(T_N^\dagger, \widetilde{T}_N(s_N'))} \prod_{i=1}^{N} \frac{W(b_i, \boldsymbol{\Sigma}_i)}{W(b_i, \bar{\boldsymbol{\Sigma}}_i)} \quad \text{(C.34)}$$

Thus we have detailded balance if

$$P_{\text{insert}}(T_0, s_1) = P_{\text{insert}}(T_N^\dagger, \widetilde{T}_N(s_N')). \qquad \text{(C.35)}$$

When the worm returns to the initial leg l_1, $T_N^\dagger$ equals either T_0, *i.e.* the worm reenters l_1 from vertex $V_N = V_1$, or equals $T_0^\dagger$ if $V_N \neq V_1$. In the first case we have $T_N^\dagger = T_0$ and $\widetilde{T}_N \, |s'_N\rangle = |s_1\rangle$ and therefore eqation (C.27) tells us that (C.35) is always satisfied. If $T_N = T_0$ we have $|s'_N\rangle = |s_1\rangle$ and we need to impose on the insertion probabilities that

$$P_{\text{insert}}(T_0^\dagger, \widetilde{T}_0(s_1)) = P_{\text{insert}}(T_0, s_1). \tag{C.36}$$

We note that the trivial insertion probabilities (C.21) which we defined for spin–$\frac{1}{2}$ models satisfy this condition.

C.5.3   Exit probabilities

We finish the description of the SSE algorithm by outlining how one computes the minimal bounce probabilities. This is achieved by constructing 4×4 "scattering" matrices P for all different types of possible vertices, with elements

$$P_{kl} = P_{b_i}(\boldsymbol{\Sigma}_i, T_{i-1} \to T_i, l_i \to l'_i) \qquad k = l'_i \bmod 4, l = l_i \bmod 4. \tag{C.37}$$

There are three constraints on these matrix elements:

1. They are probabilities: $0 \leq P_{kl} \leq 1$

2. A worm always leaves the vertex: $\sum\limits_{k=1}^{4} P_{kl} = 1$

3. local detailed balance (C.26)

The quantity we want to minimize is Tr P. The minimization of a linear equation subjected to linear constraints defines a *linear programming* problem which can be solved numerically without difficulty prior to the simulation using the simplex algorithm [138].

C.6   Observables

The internal energy is related to the partition function by $E = -\frac{\partial}{\partial \beta} \ln Z$. Evaluating this expression in the SSE representation (C.8) we obtain directly

$$E = -1/\beta \, \langle n \rangle + C \cdot \#(\text{diag. matrix elements}). \tag{C.38}$$

We recall that C is the energy offset which was added to render all diagonal matrix elements positive.

In the following we restrict the discussion to observables which are diagonal in the basis $|\alpha\rangle$ but all the forumulae can be generalized to non–diagonal observables

[133, 134]. The thermal expectation value of a diagonal observable A can be written in the SSE representation as

$$\langle A \rangle \quad = \quad \mathrm{Tr} \left\{ A \exp \left(-\beta \hat{H} \right) \right\} \tag{C.39}$$

$$\stackrel{(C.6)}{=} \quad \frac{1}{Z} \sum_{n=0}^{\infty} \sum_{\{S_n\}} \sum_{\alpha(0),...,\alpha(n)} \frac{\beta^n}{n!} \prod_{p=1}^{n} \langle \alpha(p) | H_{b_p} | \alpha(p-1) \rangle \tag{C.40}$$

$$= \quad \frac{\sum_{n=0}^{\infty} \sum_{\{S_n\}} \sum_{\alpha(0)} a[\alpha(0)] W(\alpha(0), S_n)}{\sum_{n=0}^{\infty} \sum_{\{S_n\}} \sum_{\alpha(0)} W(\alpha(0), S_n)} \tag{C.41}$$

$$= \quad \langle a[\alpha(0)] \rangle \tag{C.42}$$

where $A |\alpha(0)\rangle = a[\alpha(0)] |\alpha(0)\rangle$ and $W(\alpha, S_n) = \frac{\beta^n}{n!} \langle \alpha | \prod_{p=1}^{n} H_{b_p} | \alpha \rangle$. The statistics can be improved by taking

$$\langle A \rangle = \left\langle \frac{1}{n} \sum_{p=1}^{n} a[\alpha(p)] \right\rangle . \tag{C.43}$$

Further we will have to evaluate time dependent correlation functions $\langle A_1(\tau) A_2(0) \rangle$ for two diagonal operators A_1 and A_2. It was shown in the references [133, 134] that they are given by a binomial distribution of time propagation Δp in the correlator

$$C_{12}(\Delta p) = \frac{1}{n} \sum_{p=0}^{n-1} a_1[\alpha(p+\Delta p)] a_2[\alpha(p)] : \tag{C.44}$$

$$\langle A_1(\tau) A_2(0) \rangle = \left\langle \sum_{\Delta p=0}^{n-1} \binom{n}{\Delta p} \left(\frac{\tau}{\beta} \right)^{\Delta p} \left(1 - \frac{\tau}{\beta} \right)^{n-\Delta p} C_{12}(\Delta p) \right\rangle \tag{C.45}$$

As it is done in these formulae one has to ignore the unity operators in the operator string when making measurements. But it has been argued by Dorneich and Troyer [139] that the identity operators were uniformly distributed and would not influence the mapping from index to imaginary time. We have verified this claim when we calculated the staggered magnetization correlation function. The results in table C.2 are obtained by summing over the whole operator string (including the identity operators) whereas table C.1 was obtained with the non–unity operators only. The results are identical within statistical uncertainties.

C.7   Detailed MC simulation data for CNT

	# of sites	β	MCS	energy density	Δ_2	Δ_4
(1,1)	64	20	1.2×10^6	-0.57807(5)	0.5027(14)	0.5001(27)
	128	20	5×10^5(SKIP 20)	-0.5781(1)	0.502(8)	0.498(14)
(2,2)	256	20	2.3×10^4 *(SKIP 20)	-0.5479(1)	0.1131(7)	0.1116(8)
	512	20	2.3×10^4 *(SKIP 20)	-0.5479(1)	0.112(1)	0.110(2)
	512	50	3486*(SKIP 20)	-0.5481(1)	0.100(2)	0.099(3)
	768	50	1742*(SKIP 20)	-0.5480(1)	0.093(3)	0.093(4)
(2,0)	512	20	(SKIP 20)	-0.5612(2)	0.132(2)	0.120(2)
	256	40	(SKIP 20)	-0.5616(2)	0.089(3)	0.081(3)
	512	40	(SKIP 20)	-0.5617(2)	0.098(4)	0.093(5)
	512	50	4008*(SKIP 20)	-0.5618(1)	0.090(2)	0.084(2)
	512	60	2746*(SKIP 20)	-0.5616(1)	0.091(3)	0.088(3)
	512	70	1044*(SKIP 20)	-0.5617(2)	0.087(5)	0.084(7)
	768	50	1825*(SKIP 20)	-0.5618(1)	0.094(3)	0.089(4)
(3,0)	96	50		-0.5500(2)	0.135(1)	0.134(2)
	384	50	3822*(SKIP 20)	-0.5499(1)	0.119(3)	0.117(4)
	576	50	2699*(SKIP 20)	-0.5495(3)	0.121(4)	0.121(6)
	768	50	1676*(SKIP 20)	-0.5498(3)	0.125(5)	0.127(8)

Table C.1: Idem table C.2 except that these values were calculated by evaluating the correlator C_{12} as it is given in equation (C.44), *i.e.* summing over S_n without the identity operators.

	# of sites	β	MCS	energy density	Δ_2	Δ_4
(1,1)	64	20	5.8×10^6	-0.57802(2)	0.50309(65)	0.5019(12)
	64	40	1.9×10^5*(SKIP 50)	-0.57803(4)	0.491(11)	0.445(37)
	128	20	4×10^5*(SKIP 50)	-0.57808(3)	0.5056(26)	0.5055(48)
(2,2)	128	20	2.8×10^6	-0.54797(3)	0.12454(10)	0.12275(12)
	128	50	3.9×10^6	-0.54818(2)	0.11124(10)	0.11080(13)
	128	75	5.8×10^5	-0.54822(3)	0.11109(36)	0.11093(58)
	128	80	2×10^4		0.1121(22)	0.1131(18)
	256	50	4×10^4*(SKIP 50)	-0.54809(4)	0.09960(66)	0.09930(90)
	512	50	2.3×10^4*(SKIP 50)	-0.54817(4)	0.0965(9)	0.0960(12)
	1024	50	3872*(SKIP 50)	-0.54817(7)	0.0967(19)	0.0967(25)
(2,0)	64	20	5×10^6	-0.56172(3)	0.16757(10)	0.15922(12)
(3,0)	96	20	1.3×10^6	-0.54971(5)	0.14674(18)	0.14465(20)
	96	50	1.5×10^5		0.14002(74)	0.1389(11)
	96	80	4.9×10^4		0.1355(23)	0.1315(40)
	192	50	2.4×10^4		0.1250(16)	0.1251(21)
	768	50	1872 * (SKIP 100)	-0.54984(12)	0.1145(42)	0.1126(58)
(4,0)	128	20	2.8×10^6	-0.54663(3)	0.10654(8)	0.10440(10)
	128	50	3.5×10^6	-0.54691(2)	0.08748(8)	0.08689(10)
	128	75	1×10^6	-0.54690(2)	0.08659(18)	0.08645(25)
	512	50	2000 * (SKIP 100)	-0.54651(13)	0.0530(12)	0.0522(14)
	512	100	1584 * (SKIP100)	-0.54675(11)	0.0470(14)	0.0469(18)
	1024	50	1632 *(SKIP100)	-0.54700(12)	0.0497(12)	0.0484(14)
	1024	100	332 * (SKIP100)	-0.54648(17)	0.0440(36)	0.0431(45)
(2,1)	112	50	6.4×10^5		0.16338(50)	0.16060(79)
	112	80	2×10^5		0.1625(19)	0.1605(44)
	224	50	1.2×10^5		0.1574(10)	0.1548(15)
	224	80	1.2×10^4		0.1582(66)	0.154(15)
	448	50	2000 * (SKIP 100)	-0.55287(13)	0.1498(71)	0.141(11)
(3,1)	104	50	1×10^6		0.10153(22)	0.09985(29)
	156	50	6.6×10^5		0.07755(20)	0.07580(25)
	208	50	1.2×10^5		0.06574(28)	0.06366(33)
	520	50	2000 * (SKIP 100)	-0.54717(13)	0.0481(11)	0.0462(13)
	520	80	2000 * (SKIP 100)	-0.54729(11)	0.0388(9)	0.0370(11)
	1040	50	944 * (SKIP 100)	-0.54702(25)	0.0469(14)	0.0455(16)
	1040	80	520 * (SKIP 100)	-0.54724(14)	0.0356(17)	0.0339(22)

Table C.2: Following Todo and Kato [103] we estimate the spin gap by $\Delta_n = \lim\limits_{L,\beta\to\infty} \dfrac{1}{\xi_\tau^{(n)}}$, where $\xi_\tau^{(n)}$ stands respectively for the second– and forth–moment estimators which are given by $\xi_\tau^{(2)} = \dfrac{\beta}{2\pi}\sqrt{\dfrac{\tilde{C}(0)}{\tilde{C}(2\pi/\beta)} - 1}$ and $\xi_\tau^{(4)} = \dfrac{\beta}{4\pi}\sqrt{3\dfrac{\tilde{C}(0)-\tilde{C}(2\pi/\beta)}{\tilde{C}(2\pi/\beta)-\tilde{C}(4\pi/\beta)} - 1}$. $\tilde{C}(\omega)$ is the Fourier transform of the correlation function of the staggered magnetization in imaginary time $C(\tau) = \dfrac{1}{L^2\beta} \sum\limits_{i,j=1}^{L} \int_0^\beta \mathrm{d}t \left\langle (-1)^{|i-j|} S_i^z(t) S_j^z(t+\tau) \right\rangle$. These results are obtained by summing over the fixed sized operator string $S_{\Lambda,n}$ with identity operators.

Appendix D

Resonating valence bond mean field calculation

In this appendix we outline the details of the diagonalisation of the RVB mean field Hamiltonian (6.14) used in chapter 6

$$
H_{tJ}^{\mathrm{MF}} = \delta \sum_{\langle i,j\rangle\sigma} t_{ij} \left(f_{i\sigma}^{\dagger} f_{j\sigma} + \mathrm{h.c.} \right) - \mu \sum_i n_i \tag{D.1}
$$
$$
- \frac{J}{2} \sum_{\langle i,j\rangle} \left(\langle B^{\dagger}(i,j)\rangle \left(f_{i\downarrow} f_{j\uparrow} - f_{i\uparrow} f_{j\downarrow} \right) + \langle B(i,j)\rangle \left(f_{j\uparrow}^{\dagger} f_{i\downarrow}^{\dagger} - f_{j\downarrow}^{\dagger} f_{i\uparrow}^{\dagger} \right) \right) - \frac{3}{4} L J \Delta^2
$$

where we have set $\langle B(i,j)\rangle = \Delta e^{i\theta_{ij}}$. This calculation follows the same lines as the Hartree–Fock calculation in appendix A. Therefore we transform our Hamiltonian into reciprocal space again by equations (A.10) and (A.11). This has already be done in appendix A for the first two terms of H_{tJ}^{MF} and the exchange term can be transformed by exactly the same manipulations. Then the Hamiltonian (D.1) can be written in reciprocal space as

$$
H_{tJ}^{\mathrm{MF}} = \delta \sum_{\mathbf{k},\sigma} \left(\xi(\mathbf{k}) a_{\mathbf{k}\sigma}^{\dagger} b_{\mathbf{k}\sigma} + \mathrm{h.c.} \right) - \mu \sum_{\mathbf{k}\sigma} \left(a_{\mathbf{k}\sigma}^{\dagger} a_{\mathbf{k}\sigma} + b_{\mathbf{k}\sigma}^{\dagger} b_{\mathbf{k}\sigma} \right)
$$
$$
- J/2 \sum_{\mathbf{k}} \left[B(\mathbf{k}) \left(a_{\mathbf{k}\uparrow}^{\dagger} b_{-\mathbf{k}\downarrow}^{\dagger} + b_{-\mathbf{k}\uparrow}^{\dagger} a_{\mathbf{k}\downarrow}^{\dagger} \right) + \mathrm{h.c.} \right] - \frac{3}{4} L J \Delta^2 \tag{D.2}
$$

$\xi(\mathbf{k})$ and $B(\mathbf{k})$ are given in equations (6.18) and (6.19). Their explicit expressions are not needed here. Following reference [111] we rewrite this Hamiltonian with the help of a column vector $\boldsymbol{\Psi}_{\mathrm{C}\uparrow}(\mathbf{k}) \equiv \begin{pmatrix} a_{\mathbf{k}\uparrow} \\ b_{\mathbf{k}\uparrow} \end{pmatrix}$ and a row vector

$\mathbf{\Psi}_{\mathrm{R}\uparrow}(-\mathbf{k}) \equiv (a_{-\mathbf{k}\downarrow},\, b_{-\mathbf{k}\downarrow})$:

$$H_{tJ}^{\mathrm{MF}} = \sum_{\mathbf{k}} \left\{ \mathrm{Tr}\,[\mathrm{T}(-\mathbf{k})] + \left(\mathbf{\Psi}_{\mathrm{C}\uparrow}^{\dagger}(\mathbf{k}),\, \mathbf{\Psi}_{\mathrm{R}\uparrow}(-\mathbf{k})\right) \overbrace{\left(\begin{array}{cc} \mathrm{T}(\mathbf{k}) & \mathrm{D}(\mathbf{k}) \\ \mathrm{D}^{\dagger}(\mathbf{k}) & -\mathrm{T}(\mathbf{k}) \end{array}\right)}^{A(\mathbf{k})} \left(\begin{array}{c} \mathbf{\Psi}_{\mathrm{C}\uparrow}(\mathbf{k}) \\ \mathbf{\Psi}_{\mathrm{R}\uparrow}^{\dagger}(-\mathbf{k}) \end{array}\right) \right\} - \frac{3}{4} L J \Delta^2$$

$$\tag{D.3}$$

$A(\mathbf{k})$ is a symplectic and hermitian 4 by 4 matrix where

$$\mathrm{D}(\mathbf{k}) = \left(\begin{array}{cc} 0 & B^*(\mathbf{k}) \\ B^*(\mathbf{k}) & 0 \end{array}\right) \qquad \text{and} \qquad \mathrm{T}(\mathbf{k}) = \left(\begin{array}{cc} -\mu & \delta\xi(\mathbf{k}) \\ \xi^*(\mathbf{k}) & -\mu \end{array}\right). \tag{D.4}$$

Hermitian implies that the eigenvalues are real and from symplectic follows that they come in pairs of $\pm\varepsilon$. Doing now the algebra to find the eigenvalues of A: We write the eigenvalue equation in simplified notations:

$$A \left(\begin{array}{c} \mathbf{\Psi} \\ \mathbf{\Phi} \end{array}\right) = \left(\begin{array}{cc} \mathrm{T} & \mathrm{D} \\ \mathrm{D}^{\dagger} & -\mathrm{T} \end{array}\right) \left(\begin{array}{c} \mathbf{\Psi} \\ \mathbf{\Phi} \end{array}\right) = \varepsilon \left(\begin{array}{c} \mathbf{\Psi} \\ \mathbf{\Phi} \end{array}\right) \tag{D.5}$$

This gives the following system of matrix equations

$$\mathrm{T}\mathbf{\Psi} + \mathrm{D}\mathbf{\Phi} = \mathbf{\Psi}, \tag{D.6}$$

$$\mathrm{D}^{\dagger}\mathbf{\Psi} - \mathrm{T}\mathbf{\Phi} = \mathbf{\Phi} \tag{D.7}$$

which can be solved *e.g.* for $\mathbf{\Psi}$ to give:

$$(\varepsilon - \mathrm{T})\mathbf{\Psi} = \mathrm{D}(\varepsilon + \mathrm{T})^{-1}\mathrm{D}^{\dagger}\mathbf{\Psi} \tag{D.8}$$

$$\Rightarrow \qquad \varepsilon - \mathrm{T} = J^2|B|^2 \left(\sigma^x(\varepsilon + \mathrm{T})\sigma^x\right)^{-1}$$

$$\Rightarrow \quad (\varepsilon + \sigma^x\mathrm{T}\sigma^x)(\varepsilon - \mathrm{T}) = J^2|B|^2 \tag{D.9}$$

But T is nothing else than

$$T = -\mu + \delta\,\mathrm{Re}(\xi)\sigma^x + \delta\,\mathrm{Im}(\xi)\sigma^y \tag{D.10}$$

and therefore

$$\sigma^x\mathrm{T}\sigma^x = \mathrm{T}^{\dagger}. \tag{D.11}$$

Now we can evaluate equation (D.9):

$$(\varepsilon + \sigma^x\mathrm{T}\sigma^x)(\varepsilon - \mathrm{T}) = (\varepsilon + \mathrm{T}^{\dagger})(\varepsilon - \mathrm{T}) = J^2|B|^2$$

$$\left(\begin{array}{cc} \varepsilon^2 - \mu^2 - (\delta\xi^*)^2 & -\delta\xi(\varepsilon - \mu) + \delta\xi^*(\varepsilon + \mu) \\ -\delta\xi^*(\varepsilon - \mu) + \delta\xi(\varepsilon + \mu) & \varepsilon^2 - \mu^2 - (\delta\xi)^2 \end{array}\right) = J^2|B|^2 \tag{D.12}$$

$$\Rightarrow \quad \det\left(\begin{array}{cc} \varepsilon^2 - \mu^2 - (\delta\xi^*)^2 - J^2|B|^2 & -\delta\xi(\varepsilon - \mu) + \delta\xi^*(\varepsilon + \mu) \\ -\delta\xi^*(\varepsilon - \mu) + \delta\xi(\varepsilon + \mu) & \varepsilon^2 - \mu^2 - (\delta\xi)^2 - J^2|B|^2 \end{array}\right) = 0 \tag{D.13}$$

$$\Rightarrow \quad \left(\varepsilon^2 - \mu^2 - J^2|B|^2 - \delta^2|\xi|^2\right)^2 = 4\delta^2\left[\mu^2|\xi|^2 + J^2|B|^2(\operatorname{Im}\xi)^2\right] \qquad \text{(D.14)}$$

And finally we obtain the expressions for the four eigenvalues of A:

$$\varepsilon_\pm^2 = \mu^2 + J^2|B|^2 + \delta^2|\xi|^2 \pm 2\delta\sqrt{\mu^2|\xi|^2 + J^2|B|^2(\operatorname{Im}\xi)^2} \qquad \text{(D.15)}$$

Coming back to the mean–field Hamiltonian, it reads in diagonalized form

$$\begin{aligned}
H_{tJ}^{\mathrm{MF}} &= \sum_{\mathbf{k},j=\pm}\varepsilon_j(\mathbf{k})\gamma_{\mathbf{k}j}^\dagger\gamma_{\mathbf{k}j} - \varepsilon_j(\mathbf{k})\beta_{\mathbf{k}j}^\dagger\beta_{\mathbf{k}j} - L\mu + 3/2LJ\Delta^2 \\
&= \sum_{\mathbf{k},j=\pm}\varepsilon_j(\mathbf{k})\left(\gamma_{\mathbf{k}}^\dagger\gamma_{\mathbf{k}j} + \beta_{\mathbf{k}j}^\dagger\beta_{\mathbf{k}j}\right) - L\mu + 3/2LJ\Delta^2. \qquad \text{(D.16)}
\end{aligned}$$

Now we can get the mean field free energy density ϕ by:

$$\begin{aligned}
e^{-\beta\phi} &= \operatorname{Tr}\exp\left(-\beta H_{tJ}^{\mathrm{MF}}\right) \qquad \text{(D.17)} \\
&= \prod_{\mathbf{k}j}\sum_{\substack{n_{\gamma_{\mathbf{k}j}}=0,1 \\ n_{\beta_{\mathbf{k}j}}=0,1}}\left\langle\{n_{\gamma_{\mathbf{k}j}}\},\{n_{\gamma_{\mathbf{k}j}}\}\right|\exp\left(-\beta H_{tJ}^{\mathrm{MF}}\right)\left|\{n_{\gamma_{\mathbf{k}j}}\},\{n_{\gamma_{\mathbf{k}j}}\}\right\rangle \\
&= \prod_{\mathbf{k}j}\exp\left[-\beta\left(-\mu + 3/4J\Delta^2 - \sum_{\mathbf{k}',j'}\varepsilon_{j'}(\mathbf{k}')\right)\right]\left[1 + \exp\left(-\beta\varepsilon_j(\mathbf{k})\right)\right]^2
\end{aligned}$$

$$\Rightarrow \phi = -\mu + 3/4J\Delta^2 - \sum_{\mathbf{k},j}\left\{\varepsilon_j(\mathbf{k}) + 2/\beta\ln\left[1 + \exp\left(-\beta\varepsilon_j(\mathbf{k})\right)\right]\right\} \qquad \text{(D.18)}$$

The mean field parameters Δ, θ_{ij}, and μ are obtained by finding the minimum in the free energy function under the constraint of fixed particle density:

$$\frac{\partial\phi}{\partial\mu} = -\frac{N}{L} \qquad \Rightarrow \qquad \delta \equiv 1 - \frac{N}{L} = -\frac{1}{L}\sum_{\mathbf{k}j}\frac{\partial\varepsilon_j(\mathbf{k})}{\partial\mu}\tanh\left(\frac{\beta\varepsilon_j(\mathbf{k})}{2}\right) \qquad \text{(D.19)}$$

Bibliography

[1] R. Saito, G. Dresselhaus, and M.S. Dresselhaus. *Physical properties of carbon nanotubes*. Imperial College Press, 1998.

[2] M. S. Dresselhaus, G. Dresselhaus, and P. Avouris, editors. *Nanotubes: Synthesis, structure, properties, and applications*, volume 80 of *Topics in applied physics*. Springer, 2001.

[3] C. Thomsen, S. Reich, and J. Maultzsch. *Carbon nanotubes*. Wiley–VCH, Weinheim, 2004.

[4] S. Iijima. Helical microtubules of graphitic carbon. *Nature*, 354:56, 1991.

[5] S. Iijima and T. Ichihashi. Single-shell carbon nanotubes of 1-nm diameter. *Nature*, 363:603, 1993.

[6] D. S. Bethune, C. H. Klang, M. S. de Vries, G. Gorman, R. Savoy, J. Vazquez, and R. Beyers. Cobalt-catalysed growth of carbon nanotubes with single–atomic–layer walls. *Nature*, 363:605, 1993.

[7] S. J. Tans, A. R. M. Verschueren, and C. Dekker. Room-temperature transistor based on a single carbon nanotube. *Nature*, 393:49, 1998.

[8] D. Mann, A. Javey, J. Kong, Q. Wang, and H. Dai. Ballistic transport in metallic nanotubes with reliable Pd ohmic contacts. *Nano Lett.*, 3:1541, 2003.

[9] J. W. G. Wildöer, L. V. Venema, A.G. Rinzler, R. E. Smalley, and C. Deeker. Electronic structure of atomically resolved carbon nanotubes. *Nature*, 391:59, 1998.

[10] T. W. Odom, J.-L. Huang, P. Kim, and C. M. Lieber. Atomic structure and electronic properties of single-walled carbon nanotubes. *Nature*, 391:62, 1998.

[11] S. J. Tans, L. Zhang, N. Wang, X. X. Zhang, G. H. Wen, G. D. Li, J. N. Wang, C. T. Chan, and P. Sheng. Individual single–wall carbon nanotubes as quantum wires. *Nature*, 386:474, 1997.

[12] M. Bockrath, D. H. Cobden, J. Lu, A. G. Rinzler, R. E. Smalley, L. Balents, and P. L. McEuen. Luttinger-liquid behaviour in carbon nanotubes. *Nature*, 397:598, 1999.

[13] W. Liang, M. Bockrath, D. Bozovic, J. H. Hafner, M. Tinkham, and H. Park. Fabry–Perot interference in a nanotube electron waveguide. *Nature*, 411:665, 2001.

[14] J. Kong, E. Yenilmez, T. W. Tombler, W. Kim, H. Dai, R. B. Laughlin, L. Liu, C. S. Jayanthi, and S. Y. Wu. Quantum interference and ballistic transmission in nanotube electron waveguides. *Phys. Rev. Lett.*, 87:106801, 2001.

[15] A. Kasumov, M. Kociak, M. Ferrier, R. Deblock, S. Guéron, B Reulet, I. Khodos, O. Stéphan, and H. Bouchiat. Quantum transport through carbon nanotubes: proximity induced and intrinsic superconductivity. *Phys. Rev. B*, 68:214521, 2003.

123

[16] T. W. Ebbesen. Carbon nanotubes. *Phys. Today*, page 26, june 1996.

[17] J. W. Mintmire, B. I. Dunlap, and C. T. White. Are fullerene tubules metallic? *Phys. Rev. Lett.*, 68:631, 1992.

[18] P. R. Wallace. The band theory of graphite. *Phys. Rev.*, 71:622, 1947.

[19] R. Saito, M. Fujita, G. Dresselhaus, and M. S. Dresselhaus. Electronic structure of graphene tubules based on C_{60}. *Phys. Rev. B*, 46:1804, 1992.

[20] N. Hamada, S. Sawada, and A. Oshiyama. New one–dimensional conductors: graphite microtubules. *Phys. Rev. Lett.*, 68:1579, 1992.

[21] N. Brandt, S. M. Chudinov, and Ya.G. Ponomarev. *Semimetals: Graphite and its compounds*, volume 20 of *Modern problems in condensed matter sciences*. North-Holland, 1988.

[22] W. A. Harrison. *Electronic structure and the properties of solids: the physics of the chemical bond.* Dover Publications, 1989.

[23] S. Reich, C. Thomsen, and P. Ordejón. Electronic band structure of isolated and bundled carbon nanotubes. *Phys. Rev. B*, 65:155411, 2002.

[24] J. W. Mintmire and C. T. White. Universal density of states for carbon nanotubes. *Phys. Rev. Lett.*, 81:2506, 1998.

[25] S. Reich, J. Maultzsch, C. Thomsen, and P. Ordejón. Tight–binding description of graphene. *Phys. Rev. B*, 66:35412, 2002.

[26] C. L. Kane and E. J. Mele. Size, shape, and low energy electronic structure of carbon nanotubes. *Phys. Rev. Lett.*, 78:1932, 1997.

[27] A. Kleiner and S. Eggert. Curvature, hybridization, and STM images of carbon nanotubes. *Phys. Rev. B*, 64:113402, 2001.

[28] X. Blase, L. X. Benedict, E. L. Shirley, and S. G. Louie. Hybridization effects and metallicity in small radius carbon nanotubes. *Phys. Rev. Lett.*, 72:1878, 1994.

[29] M. Ouyang, J.-L. Huang, C. L. Cheung, and C. M. Lieber. Energy gaps in "metallic" single–walled carbon nanotubes. *Science*, 292:702, 2001.

[30] L. Balents and M. P. A. Fisher. Correlation effects in carbon nanotubes. *Phys. Rev. B*, 55:R11973, 1997.

[31] F. Gebhard. *The Mott metal–insulator transition.* Springer, 1997.

[32] N. F. Mott. *Metal–insulator transitions.* Taylor and Francis, London, second edition, 1990.

[33] G. D. Mahan. *Many-particle physics.* Kluwer Academic/Plenum Publishers, third edition, 2000.

[34] J. E. Hirsch. Two–dimensional Hubbard model: Numerical simulation study. *Phys. Rev. B*, 31:4403, 1985.

[35] J. E. Hirsch and S. Tang. Antiferromagnetism in the two–dimensional Hubbard model. *Phys. Rev. Lett.*, 62:591, 1989.

[36] S. R. White, D. J. Scalapino, R. L. Sugar, E. Y. Loh, J. E. Gubernatis, and R. T. Scalettar. Numerical study of the two-dimensional Hubbard model. *Phys. Rev. B*, 40:506, 1989.

[37] S. Sorella, A. Parola, M. Parrinello, and E. Tosatti. Numerical study of the 2d Hubbard model at half filling. *Int. J. Mod. Phys. B*, 3:1875, 1989.

[38] L. Perfetti, T. A. Gloor, F. Mila, H. Berger, and M. Grioni. Unexpected periodicity in the quasi–two-dimensional Mott insulator $1T$-TaS$_2$ revealed by angle–resolved photoemission. *Phys. Rev. B*, 71:153101, 2005.

[39] S. Sorella and E. Tosatti. Semi-metal-insulator transition of the Hubbard model in the honeycomb lattice. *Europhys. Lett.*, 19:699, 1992.

[40] N. Furukawa. Antiferromagnetism of the Hubbard model on a layered honeycomb lattice. *J. Phys. Soc. Jpn.*, 70:1483, 2001.

[41] T. Paiva, R.T. Scalettar, W. Zheng, R.R.P. Singh, and J. Oitmaa. Ground state and finite temperature signatures of quantum phase transitions in the half-filled Hubbard model on a honeycomb lattice. *cond-mat/0406535*.

[42] L. M. Martelo, M. Dzierzawa, L. Siffert, and D. Baeriswyl. Mott–Hubbard transition and antiferromagnetism on the honeycomb lattice. *Z. Phys. B*, 103:335, 1997.

[43] M. P. López Sancho, M. C. Muñoz, and L. Chico. Coulomb interactions in carbon nanotubes. *Phys. Rev. B*, 63:165419, 2001.

[44] K. Penc and F. Mila. Charge gap in the one–dimensional dimerized Hubbard model at quarter–filling. *Phys. Rev. B*, 50:11429, 1994.

[45] A. I. Larkin and J. Sak. Boundary conditions for renormalisation group equations in one–dimensional fermi gas. *Phys. Rev. Lett.*, 39:1025, 1977.

[46] S. Kuwajima and Z. G. Soos. Aromacity and electron correlation. *J. Am. Chem. Soc.*, 109:107, 1987.

[47] E. Jeckelmann and D. Baeriswyl. Solitons in the one–dimensional Peierls-Hubbard model. *Synthetic Metals*, 69:651, 1995.

[48] S. Chakravarty, S. Khlebnikov, and S. Kivelson. Comment on "electron-phonon coupling and superconductivity in alkali-intercalated C$_{60}$ solid". *Phys. Rev. Lett.*, 69:212, 1992.

[49] O. Gunnarsson and G. Zwicknagl. Coulomb pseudopotential, screening and superconductivity in C$_{60}$. *Phys. Rev. Lett.*, 69:957, 1992.

[50] A. L. Tchougreeff and R. Hoffmann. Charge and spin density waves in the electronic structure of graphite. Application to analysis of STM images. *J. Phys. Chem.*, 96:8993, 1992.

[51] H. Gutfreund and W. A. Little. Correlation effects of π electrons. I. screening. *Phys. Rev*, 183:68, 1969.

[52] C. Zhou, J. Kong, and H. Dai. Intrinsic electrical properties of individual single–walled carbon nanotubes with small band gaps. *Phys. Rev. Lett.*, 84:5604, 2000.

[53] M. Sagnes, B. Raquet, B. Lassagne, J. M. Broto, E. Flahaut, C. Laurent, T. Ondarçuhu, F. Carcenac, and C. Vieu. Probing the electronic properties of inividual carbon nanotube in 35 T pulsed magnetic field. *Chem. Phys. Lett.*, 372:733, 2003.

[54] T. Nussbaumer C. Schönenberger M. Krüger, M. R. Buitelaar and L. Forrò. Electrochemical carbon nanotube field–effect transistor. *Appl. Phys. Lett.*, 78:1291, 2001.

[55] A. Rakitin, C. Papadopoulos, and J. M. Xu. Carbon nanotube self–doping: Calculation of the hole carrier concentration. *Phys. Rev. B*, 67:033411, 2003.

[56] T. W. Tombler, C. Zhou, L. Alexseyev, J. Kong, H. Dai, L. Liu, C. S. Jayanthi, M. Tang, and S. Wu. Reversible electrochemical characteristics of carbon nanotubes under local-probe manipulation. *Nature*, 405:769, 2000.

[57] J.-P. Salvetat, J.-M. Bonard, N. H. Thomson, A. J. Kulik, L. Forró, W. Benoit, and L. Zuppiroli. Mechanical properties of carbon nanotubes. *Appl. Phys. A*, 69:255, 1999.

[58] E. D. Minot, Y. Yaish, V. Sazonova, J.-Y. Park, M. Brink, and P. L. McEuen. Tuning carbon nanotube band gaps with strain. *Phys. Rev. Lett*, 90:156401, 2003.

[59] L. Yang and J. Han. Electronic structure of deformed carbon nanotubes. *Phys. Rev. Lett.*, 85:154, 2000.

[60] R. Heyd, A. Charlier, and E. McRae. Uniaxial–stress effects on the electronic properties of carbon nanotubes. *Phys. Rev. B*, 55:6820, 1997.

[61] M. Buongiorno Nardelli and J. Bernholc. Mechanical deformations and coherent transport in carbon nanotubes. *Phys. Rev. B*, 60:R16338, 1999.

[62] A. Maiti, A. Svizhenko, and M. P. Anantram. Electronic transport through carbon nanotubes: Effects of structural deformation and tube chirality. *Phys. Rev. Lett.*, 88:126805, 2002.

[63] A. Rochefort, P. Avouris, F. Lesage, and D. R. Salahub. Electrical and mechanical properties of distorted carbon nanotubes. *Phys. Rev. B*, 60:13824, 1999.

[64] B. T. Kelly. *Physics of graphite*. Applied Science, 1981.

[65] A. Bachtold, C. Strunk, J.-P. Salvetat, J.-M. Bonard, L. Forró, T. Nussbaumer, and C. Schönenberger. Aharonov–Bohm oscillations in carbon nanotubes. *Nature*, 397:673, 1999.

[66] A. Fujiwara, K. Tomiyama, and H. Suematsu. Quantum interference of electrons in multiwall carbon nanotubes. *Phys. Rev. B*, 60:13492, 1999.

[67] J.-O. Lee, J.-R. Kim, J.-J. Kim, J. Kim, N. Kim, J. W. Park, and K.-H. Yoo. Observation of magnetic–field–modulated energy gap in carbon nanotubes. *Solid State Comm.*, 115:467, 2000.

[68] S. Zaric, G. N. Ostojic, J. Kono, J. Shaver, V. C. Moore, M. S. Strano, R. H. Hauge, R. E. Smalley, and X. Wei. Optical signatures of the Aharonov–Bohm phase in single-walled carbon nanotubes. *Science*, 304:1129, 2004.

[69] U. C. Coskun, T.-C. Wei, S. Vishveshwara, P. M. Goldbart, and A. Bezryadin. h/e magnetic flux modulation of the energy gap in nanotube quantum dots. *Science*, 304:1132, 2004.

[70] E. D. Minot, Y. Yaish, V. Sazonova, and P. L. McEuen. Measuring electron orbital magnetic moments in carbon nanotubes. *Nature*, 428:536, 2004.

[71] J. M. Luttinger. The effect of a magnetic field on electrons in a periodic potential. *Phys. Rev.*, 84:814, 1951.

[72] J. P. Lu. Novel magnetic properties of carbon nanotubes. *Phys. Rev. Lett.*, 74:1123, 1995.

[73] T. Giamarchi. *Quantum physics in one dimension*. Oxford University Press, 2004.

[74] B. S. Shastry and B. Sutherland. Twisted boundary conditions and effective mass in Heisenberg–Ising and Hubbard rings. *Phys. Rev. Lett.*, 65:243, 1990.

[75] I. Sadakata and E. Hanamura. Optical absorption in a half–filled narrow band. *J. Phys. Soc. Japan*, 34:882, 1973.

[76] H. Ajiki and T. Ando. Electronic states of carbon nanotubes. *J. Phys. Soc. Japan*, 62:1255, 1993.

[77] M. Szopa, M. Margańska, and E. Zipper. Persistent currents in carbon nanotubes. *Phys. Lett. A*, 299:593, 2002.

[78] M. Szopa, M. Margańska, E. Zipper, and M. Lisowski. Coherence of persistent currents in multiwall carbon nanotubes. *Phys. Rev. B*, 70:075406, 2004.

[79] K. Sasaki, S. Murakami, and R. Saito. Fractional flux periodicity in doped carbon nanotubes. *Phys. Rev. B*, 70:233406, 2004.

[80] M. F. Lin and D. S. Chuu. Persistent currents in toroidal carbon nanotubes. *Phys. Rev. B*, 57:6731, 1998.

[81] S. Latil, S. Roche, and A. Rubio. Persistent currents in carbon nanotubes based rings. *Phys. Rev. B*, 67:165420, 2003.

[82] H. R. Shea, R. Martel, and Ph. Avouris. Electrical transport in rings of single–wall nanotubes: One–dimensional localization. *Phys. Rev. Lett.*, 84:4441, 2000.

[83] B. L. Al'tshuler, A. G. Aronov, and B. Z. Spivak. The Aaronov–Bohm effect in disordered conductors. *JETP Lett.*, 33:94, 1981.

[84] A. I. Larkin and D. E. Khmelnitskii. Anderson localization and anomalous magnetoresistance at low temperatures. *Sov. Phys. Usb.*, 25:185, 1982.

[85] J. W. Negele and H. Orland. *Quantum many-particle systems*. Advanced book classics. Westview Press, 1998.

[86] Y. Imry. *Introduction to mesoscopic physics*. Oxford University Press, second edition, 2002.

[87] P. W. Anderson. Absence of diffusion in certain random lattices. *Phys. Rev.*, 109:1492, 1958.

[88] E. Abrahams, P. W. Anderson, D. C. Licciardello, and T. V. Ramakrishnan. Scaling theory of localization: Absence of quantum diffusion in two dimensions. *Phys. Rev. Lett.*, 42:673, 1979.

[89] G. Bouzerar and D. Poilblanc. Persistent currents in multichannel interacting systems. *Phys. Rev. B*, 52:10772, 1995.

[90] G. Bouzerar and D. Poilblanc. Persistent currents in interacting systems: Role of the spin. *J. Phys. I France*, 7:877, 1997.

[91] E. A. Jagla and C. A. Balseiro. Electron–electron correlations and the Aharonov–Bohm effect in mesoscopic rings. *Phys. Rev. Lett.*, 70:639, 1993.

[92] F. V. Kusmartsev, J. F. Weisz, R. Kishore, and M. Takahashi. Strong correlations versus U–center pairing and fractional Aharonov–Bohm effect. *Phys. Rev. B*, 49:16234, 1994.

[93] V. Ferrari and G. Chiappe. The fractional Aharonov–Bohm effect in mesoscopic rings. *J. Phys.: Condens. Matter*, 8:8683, 1996.

[94] P. Fazekas. *Lecture Notes on Electron Correlation and Magnetism*, volume 5 of *Series in Modern Condensed Matter Physics*. World Scientific, Singapore, 1999.

[95] B. Frischmuth, B. Ammon, and M. Troyer. Susceptibility and low–temperature thermodynamics of spin–$\frac{1}{2}$ Heisenberg ladders. *Phys. Rev. B*, 54:R3714, 1996.

[96] H. J. Schulz. Phase diagrams and correlation exponents for quantum spin chains of arbitrary spin quantum number. *Phys. Rev. B*, 34:6372, 1986.

[97] A. Auerbach. *Interacting electrons and quantum magnetism*. Springer, New York, 1997.

[98] M. Matsumoto, T. Sakai, M. Sato, H. Takayama, and S. Todo. Quantum phase transitions of spin chiral nanotubes. 2005. cond-mat/0506626.

[99] J.B. Fouet, P. Sindzingre, and C. Lhuillier. An investigation of the quantum J_1–J_2–J_3 model on the honeycomb lattice. *Euro. Phys. J. B*, 20:241, 2001.

[100] M. E. Peskin and D. V. Schroeder. *An introduction to quantum field theory.* Perseus Books, 1995.

[101] M. Troyer, H. Tsunetsugu, and D. Würtz. Thermodynamics and spin gap of the Heisenberg ladder calculated by the look–ahead Lanczos algorithm. *Phys. Rev. B*, 50:13515, 1994.

[102] J. D. Reger, J. A. Riera, and A. P. Young. Monte Carlo simulations of the spin-$\frac{1}{2}$ Heisenberg antiferromagnet in two dimensions. *J. Phys.: Condens. Matter*, 1:1855, 1989.

[103] S. Todo and K. Kato. Cluster algorithms for general-S quantum spin systems. *Phys. Rev. Lett.*, 87:047203, 2001.

[104] P. W. Anderson. The resonating valence bond state in La_2CuO_4 and superconductivity. *Science*, 235:1196, 1987.

[105] T. M. Rice. *Lectures on microscopic theories for high–T_c superconductors.* Troisième cycle de la physique en suisse romande, april 2004.

[106] P. W. Anderson. Resonating valence bonds: A new kind of insulator? *Materials Research Bulletin*, 8:153, 1973.

[107] P. W. Anderson P. Fazekas. Ground–state properties of anisotropic triangular antiferromagnet. *Philosophical Magazine*, 30:423, 1974.

[108] P. Coleman. New approach to the mixed-valence problem. *Phys. Rev. B*, 29:3035, 1984. The idea of slave bosons seems to go back to S.E. Barnes, J. Phys. F **6**, 1374 (1976).

[109] G. Kotliar and J. Liu. Superexchange mechanism and d–wave superconductivity. *Phys. Rev. B*, 38:5142, 1988.

[110] M. U. Ubbens and P. A. Lee. Superconductivity phase diagram in the gauge-field description of the t-J model. *Phys. Rev. B*, 49:6853, 1994.

[111] B. Sriram Shastry and Brijesh Kumar. $SrCu_2(BO_3)_2$: A unique Mott Hubbard insulator. *Prog. Theor. Phys. Suppl.*, 145:1, 2002.

[112] Brijesh Kumar and B. Sriram Shastry. Superconductivity in CoO_2 layers and the resonating valence bond mean–field theory of the triangular lattice t–J model. *Phys. Rev. B*, 68:104508, 2003.

[113] C. Gros. Physics of projected wavefunctions. *Annals of Phys.*, 189:53, 1989.

[114] E. Heeb. *A new variational method with application to strongly correlated electrons.* PhD thesis, ETH Zürich, 1994. http://e-collection.ethbib.ethz.ch/show?type=diss&nr=10765.

[115] J. M. Hammersley and D. C. Handscomb. *Monte Carlo Methods.* Methuen, London, 1964.

[116] C. Weber, A. Läuchli, F. Mila, and T. Giamarchi. Interplay of magnetism and superconductivity of strongly correlated electrons on the triangular lattice. 2005. in preparation.

[117] L. Capriotti, A. E. Trumper, and S. Sorella. Long–range Néel order in the triangular Heisenberg model. *Phys. Rev. Lett.*, 82:3899, 1999.

[118] C. Weber. unpublished.

[119] U. J. Wiese and H. P. Ying. A determination of the low–energy parameters of the 2–D Heisenberg–antiferromagnet. *Z. Phys. B*, 93:147, 1994.

[120] V. Bach, E. H. Lieb, and J. P. Solovey. Generalized Hartree–Fock theory and the Hubbard model. *J. Stat. Phys.*, 76:3, 1994.

[121] J. Sólyom. The fermi gas model of one–dimensional conductors. *Adv. in Phys.*, 28:201, 1979.

[122] A. L. Fetter and J. D. Walecka. *Quantum theory of many-particle systems*. McGraw–Hill, New York, 1971.

[123] L. D. Landau and I. M. Lifshitz. *Statistical physics*. Pergamon Press, Oxford, third edition, 1986.

[124] Yu. A. Bychkov, L. P. Gorkov, and I. E. Dzyaloshinskii. Possibility of superconductivity type phenomena in a 1-dimensional system. *Sov. Phys. JETP*, 23:489, 1966.

[125] C. Bourbonnais, B. Guay, and R. Wortis. Renormalization group technique for quasi–one–dimensional interacting fermion systems at finite temperature. In A.M. Tremblay, D. Sénéchal, A. Ruckenstein, and C. Bourbonnais, editors, *Theoretical methods for strongly correlated electrons*, 2003. cond-mat/0204163.

[126] A. Luther and V. J. Emery. Backward scattering in the one–dimensional electron gas. *Phys. Rev. Lett.*, 33:589, 1974.

[127] E. H. Rezayi, J. Sak, and J. Sólyom. Symmetry properties of one-dimensional fermi systems: Some nonperturbative results. *Phys. Rev. B*, 23:1342, 1981.

[128] I. E. Dzyaloshinskii and A. I. Larkin. Possible states of quasi–unidimensional systems. *Sov. Phys. JETP*, 34:422, 1972.

[129] D. Pines and P. Nozières. *Theory of quantum liquids*. Advanced book classics. Westview Press, 1999.

[130] W. Feller. *An introduction to probability theory and its applications*. John Wiley & Sons, New York, third (revised printing) edition, 1970.

[131] F. Alet, S. Wessel, and M. Troyer. Generalized directed loop method for quantum Monte Carlo simulations. *Phys. Rev. E*, 71:036706, 2005.

[132] S. Wessel. Introduction to quantum Monte Carlo. Talk at the First ALPS User Workshop (Lugano, sept. 2004). Slides are available at http://www.comp-phys.org/lugano04/.

[133] A. W. Sandvik and J. Kurkijärvi. Quantum Monte Carlo simulation method for spin systems. *Phys. Rev. B*, 43:5950, 1991.

[134] A. W. Sandvik. A generalization of Handscomb's quantum Monte Carlo scheme—application to the 1D Hubbard model. *J. Phys. A*, 25:3667, 1992.

[135] A. W. Sandvik. Stochastic series expansion method with operator-loop update. *Phys. Rev. B*, 59:R14157, 1999.

[136] O. F. Syljuåsen and W. Sandvik. Quantum Monte Carlo with directed loops. *Phys. Rev. E*, 66:046701, 2002.

[137] O. F. Syljuåsen. Directed loop updates for quantum lattice models. *Phys. Rev. E*, 67:046701, 2003.

[138] G. B. Dantzig. *Linear programming and extensions*. Princeton University Press, Princeton, 1998. reprint from 1963.

[139] A. Dorneich and M. Troyer. Accessing the dynamics of large many-particle systems using the stochastic series expansion. *Phys. Rev. E*, 64:66701, 2001.

Curriculum vitae

name:	Thomas Gloor
date of birth:	3rd of may 1975
citizenship:	Liechtenstein
marital status:	single

Education

1987–1995	Liechtensteinisches Gymnasium, Vaduz
10/1995–3/2000	studies in physics at EPFL
	exchange year at the University of Nottingham
	diploma thesis with T. M. Rice at ETH Zürich
10/2000–9/2001	D. Phil. student at Oxford University with A. Tsvelik
10/2001–10/2005	teaching assistant and graduate student
	at the University of Lausanne and EPFL with F. Mila

List of publications

L. Perfetti, T. A. Gloor, F. Mila, H. Berger, M. Grioni: "Unexpected periodicity in the quasi-two-dimensional Mott insulator 1T-TaS$_2$ revealed by angle-resolved photoemission." Phys. Rev B **71**, 153101 (2005).

T. A. Gloor, F. Mila: "Strain induced correlation gaps in carbon nanotubes" Eur. Phys. J. B **38**, 9 (2004).

T. A. Gloor, F. Mila: "Correlation gap in armchair carbon nanotubes" Europhys. Lett. **61**, 513 (2003).

T. A. Gloor, M. E. Zhitomirsky, T. M. Rice: " Multiexciton molecules in the hexaborides " Eur. Phys. J. B **21**, 491 (2001).